HULL/MOORING/RISER COUPLED MOTION SIMULATIONS

OF THRUSTER-ASSISTED MOORED PLATFORMS

A Dissertation

by

SANGSOO RYU

Submitted to the Office of Graduate Studies of
Texas A&M University
in partial fulfillment of the requirements for the degree of

DOCTOR OF PHILOSOPHY

December 2003

Major Subject: Ocean Engineering

HULL/MOORING/RISER COUPLED MOTION SIMULATIONS

OF THRUSTER-ASSISTED MOORED PLATFORMS

A Dissertation

by

SANGSOO RYU

Submitted to Texas A&M University
in partial fulfillment of the requirements
for the degree of

DOCTOR OF PHILOSOPHY

Approved as to style and content by:

Moo-Hyun Kim (Chair of Committee)	Hamn-Ching Chen (Member)
Julian H. Kang (Member)	Robert H. Stewart (Member)
Jun Zhang (Member)	Paul N. Roschke (Head of Department)

December 2003

Major Subject: Ocean Engineering

ABSTRACT

Hull/Mooring/Riser Coupled Motion Simulations

of Thruster-Assisted Moored Platforms. (December 2003)

Sangsoo Ryu, B.S.; M.S., Inha University

Chair of Advisory Committee: Dr. Moo-Hyun Kim

To reduce large motion responses of moored platforms in a harsh environment in deep waters, a thruster-assisted position mooring system can be applied. By applying the system, global dynamic responses can be improved in terms of the mooring line/riser top tensions, operational radii, and the top and bottom angle of the production risers. Kalman filtering as an optimum observer and estimator for stochastic disturbances is implemented in the developed control algorithm to filter out wave frequency responses. Investigation of the performance of thruster-assisted moored offshore platforms was conducted in terms of six-degree-of-freedom motions and mooring line/riser top tensions by means of a fully coupled hull/mooring/riser dynamic analysis program in the time domain and a spectral analysis.

The two cases, motion analyses of a platform with thrusters and without thrusters, are extensively compared. The numerical examples illustrate that for deepwater position-keeping of platforms a thruster-assisted moored platform can be an effective solution compared to a conventionally moored platform.

To my mother Ho-gil

and the memory of my father in heaven Seung-kyu Ryu

ACKNOWLEDGMENTS

I would like to express special thanks to my advisor Dr. M. H. Kim for his continuous encouragement and guidance during my research. From the beginning of my study at Texas A&M University, Dr. Kim has been the role model for both my academic life and daily life. His teaching, teaching philosophy, leadership, expertise, and personality deserve to be praised.

Special thanks are extended to Dr. Hamn-Ching Chen, Dr. Jun Zhang, Dr. Robert H. Stewart, and Dr. Julian H. Kang for their excellent service as my academic committee advisors.

I cannot help expressing my special thanks to Dr. Billy L. Edge, Dr. C. H. Kim, Dr. Richard Mercier, and Dr. Robert E. Randall for their excellent teaching and counseling, and to Dr. Jose M. Roesset, my TAMU Teaching Academy mentor, for sharing his invaluable academic experiences and advice regarding academic life.

I would also like to thank Rev. Scott Nelson, my best Aggie friend, for his friendship, mentorship, and proof-reading.

Lastly, I would like to express my appreciation to my parents, Ho-gil and Seung-kyu Ryu, to my wife Jihyun, and to my two lovely daughters, Hyunah and Grace, for their love and encouragement. In addition, I owe my American parents, Dotty and Ernie Prochaska, for their prayers and strong encouragement.

TABLE OF CONTENTS

CHAPTER Page

CHAPTER Page

LIST OF FIGURES

FIGURE Page

FIGURE Page

FIGURE Page

FIGURE Page

FIGURE Page

FIGURE Page

LIST OF TABLES

TABLE Page

CHAPTER I

INTRODUCTION

1.1. Background

As the current major oil and gas fields in the Gulf of Mexico (GoM) are being depleted, new potential fields in ultra-deep seas (i.e., greater than 2,000m water depth) are receiving more and more attention. As shown in Figs. 1.1 and 1.2., the challenging need to address ultra-deep sea system types is clearly recognized. Applicable deepwater system types consist of compliant towers (CTs), conventional tension leg platforms (TLPs), mini-TLPs, semi-FPSs (floating production systems), truss spars, classic spars, control buoys

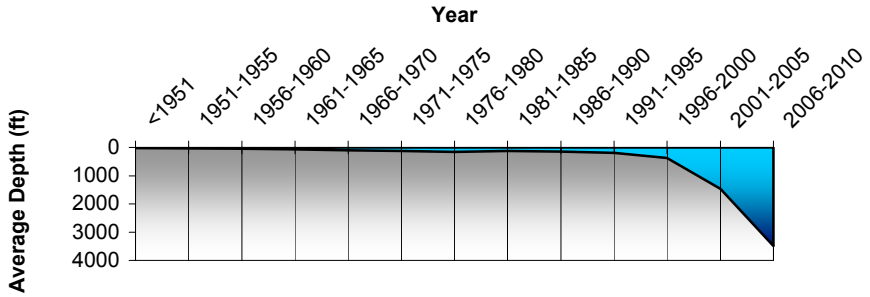

Fig. 1.1. GoM milestones in average water depth.

(From Infield Systems Ltd., Offshore Journal, January 2003)

This dissertation follows the style and format of *Journal of Ocean Engineering.*

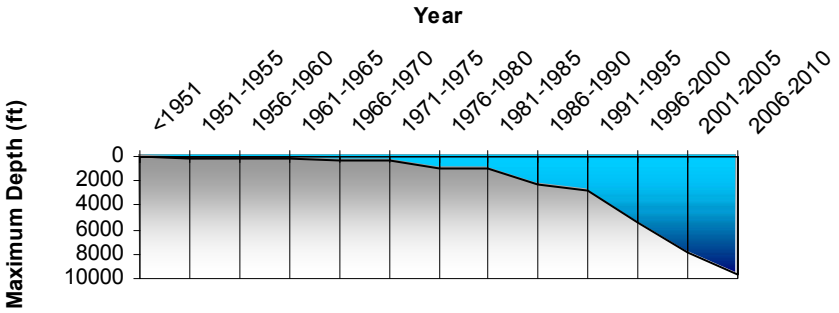

Fig. 1.2. GoM milestones in maximum water depth.

(From Infield Systems Ltd., Offshore Journal, January 2003)

(CBs), and floating production storage and offloading units (FPSOs) as shown in Fig. 1.3.

FPSOs are among the most promising offshore structures for ultra-deep seas because they have large storage capacity compared to others and thus address the lack of pipeline infrastructure. In addition, they can be used for testing and early production, and the disconnectable turret-riser systems allow FPSOs to sail away from the operational

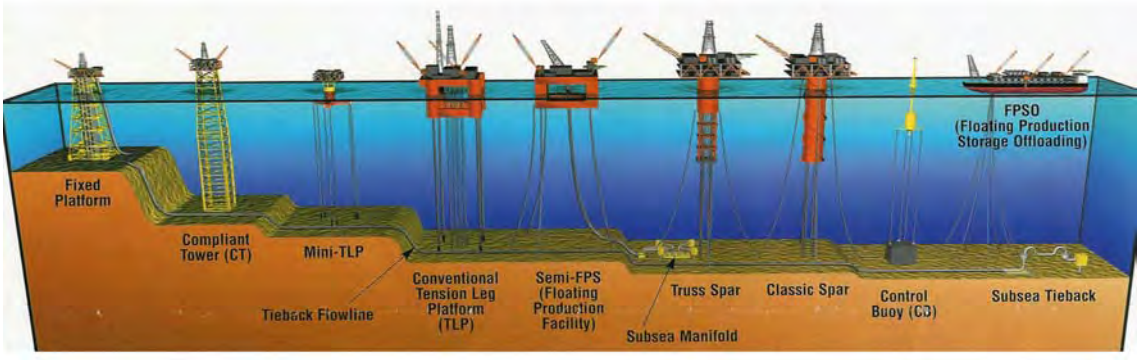

Fig. 1.3. Deepwater system types. (From 2002 Offshore Oil & Gas Industry Deepwater Solutions for Concept Selection, Mustang Engineering)

locations for safety purposes when FPSOs face harsh environmental conditions.

One example of how to seek a deep water solution is shown in Fig. 1.4.

Two types of positioning systems were suggested by Sorensen et al. (1999): dynamic positioning (DP) systems used for positioning of freely floating offshore structures and thruster-assisted position mooring (POSMOOR) systems used for moored structures.

Mooring line systems have been used to keep structures in position. For the station-keeping FPSOs, although conventional wire and chain moorings can be applied, the costs of moorings will increase significantly with water depth. On the other hand, a DP system or thruster-assisted POSMOOR performs well both in deep and shallow water, and the costs do not increase significantly as moorings (Barltrop, 1998). A comprehensive large-scale model test and numerical simulations were conducted (Cortijo et al., 2003), and the results emphasize that the full DP FPSO system is a feasible and cost-efficient solution for ultra-deep water oil/gas development. However, a thruster-assisted turret-moored FPSO may be a more popular solution in deep waters because the offshore platforms should

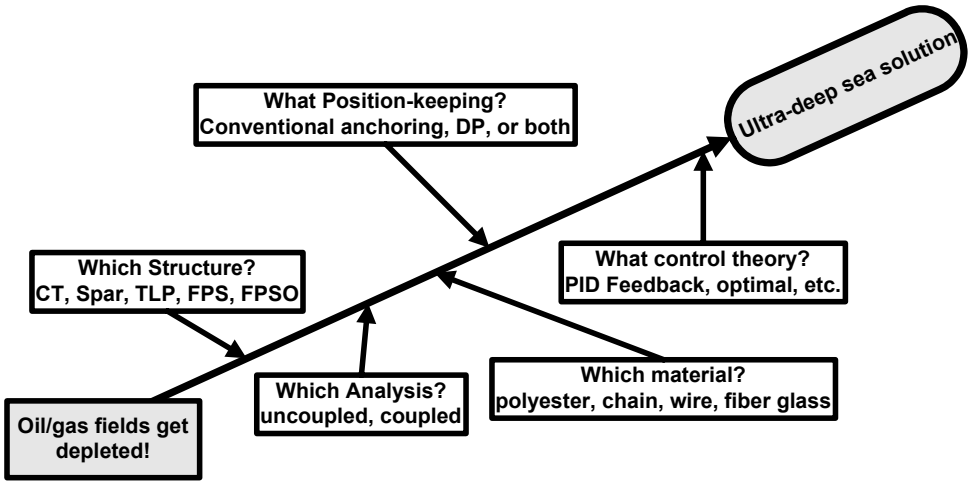

Fig. 1.4. Diagram that explains one example to seek a possible deepwater solution.

endure harsh environmental conditions and operate for relatively longer period of time as opposed to other full DP applications, such as pipelaying, drilling, diving support, submarine salvage, etc., used in relatively short term offshore operations. An exemplary DP concept is shown in Fig. 1.5 and Fig. 1.6.

Therefore, the thruster-assisted POSMOOR system is a reasonable solution, and it has already been used to maintain the position of turret-moored FPSOs in deep seas (Lee and Choi, 2000). For instance, this thruster-assisted POSMOOR system is applied to the Petrojarl, Norwegian shuttle tankers, BP's SWOPS (Single-Well Oil-Production System) vessel, Kerr McGee's Gryphon FPSO, the Texaco Captain FPSO, BP's Foinaven Phase I FPSO, and Statoil's Norne FPSO (Aalbers et al., 1995). Thruster-assisted turret-moored FPSOs are expected to be in use in the GoM in the near future as many of them are in operation in the North Sea and have been studied for the GoM (Cortijo et al., 2003, and Wichers and Dijk, 1999). Currently, a JIP has already demonstrated the feasibility of

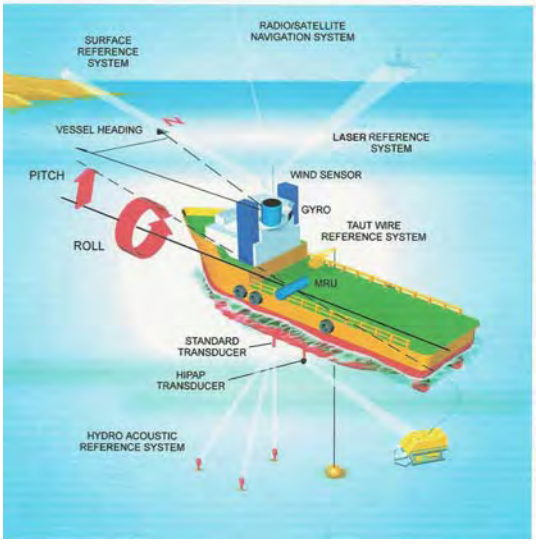

Fig. 1.5. Schematic diagram of a DP system. (Courtesy of KONGSBERG-SIMRAD)

maintaining a large FPSO on position in extreme conditions in the GoM using a DP thruster system (Cortijo et al., 2003).

Since no wave basin can correctly scale the entire ultra-deep water system, reliable numerical tools will play an important role for design and evaluation of the system. Another important issue concerning the global analysis of offshore structures in deep waters is what analysis gives the most reliable answers. A study has shown that uncoupled analysis might give inaccurate results especially for deep-water problems (Ma et al., 2000). In ultra-deep seas, the mass and length of mooring lines and risers become greater; thus, an accurate estimate of the damping and inertia effects of mooring lines and risers on the hull motions can only be achieved by fully coupled analysis programs.

However, a coupled motion analysis for a thruster-assisted offshore platform has not been studied. This research will focus on a new approach: a coupled dynamic analysis of a

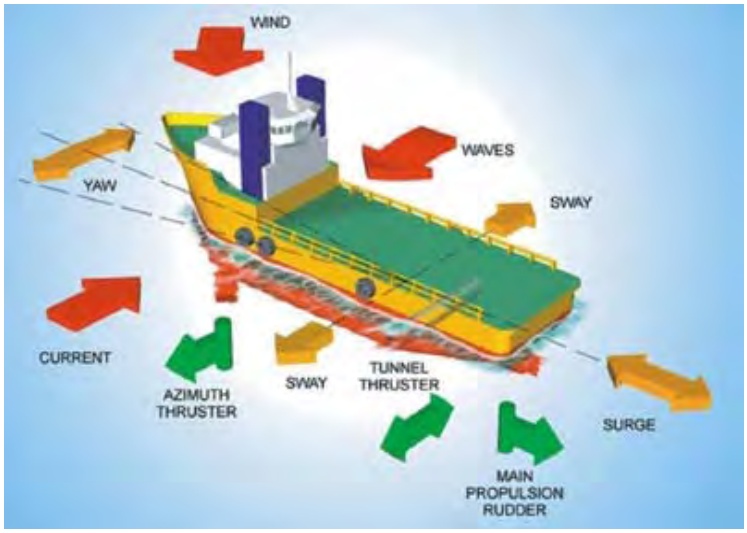

Fig. 1.6. Illustration of a DP system with typical environmental forces.

(Courtesy of KONGSBERG-SIMRAD)

thruster-assisted turret-moored FPSO and a thruster-assisted spar. It will also address a conceptual study through relevant numerical simulations of the platforms in hypothetically deep water on the basis of an assumption that a common thruster specification is not given.

1.2. Literature Review

For deepwater floating structures, vessel motions would be more influenced by moorings and risers. Therefore, as water depth increases, the uncoupled quasi-static analysis, which assumes that moorings/tendons and risers respond statically to the motion of the structure, may produce inaccurate results (Ma et al., 2000, and Arcandra, 2001). In this regard, the hull/mooring/riser coupled analysis of a tanker based turret-moored FPSO designed for 1,829m (6,000ft) water depth was carried out by using a coupled dynamic analysis tool called WINPOST-FPSO (Arcandra et al., 2001). On the other hand, Lee, Ha, and Kim (1999) considered the control performance of a turret-moored vessel assisted by a DP system by developing a nonlinear simulator and designing a robust two-degree of freedom controller. They conducted numerical simulations of the nonlinear responses of the FPSO for both the station-keeping mode and tracking mode and concluded that the control system worked satisfactorily. However, in the paper, restoring forces of mooring lines were estimated by the catenary equation and regarded as quasi-static.

To design full DP or thruster-assisted POSMOOR systems, a three-degree of freedom problem is generally adequate for the dynamic analysis (Fossen, 1994). However, Sorensen and Strand (1998) discussed coupling effects between the horizontal plane (surge, sway, and yaw) and the vertical plane (heave, roll, and pitch). They stressed that undesirable

large roll and pitch oscillations may be induced by the thruster actions for certain marine structures, such as semi-submersibles, since they have small water-plane area and low metacentric height, resulting in relatively low hydrostatic coupling phenomena between the vertical plane and the horizontal plane. It was also pointed out that the natural periods of roll and pitch motions, typically in the range of 35-65 seconds, are within the bandwidth of the positioning controller. They proposed a new multivariable control law to account for motion coupling between the two planes.

A nonlinear passivity-based state observer was developed for a thruster-assisted turret-moored FPSO, and the reduction of the number of tuning parameters was addressed (Sorensen et al., 1999). However, a quasi-static approach was used for a mooring system in this study.

1.3. Specific Aims and Scope

Reduction of large motion responses of offshore platforms in a harsh environment in deep waters is the most important consideration for the analysis and/or design of the platforms. DP systems can be applied to increase motion performance of the platforms, but thruster-assisted FPSOs are not fully understood in the sense of hull/mooring/riser coupled analysis. The goal of this study is to develop and recommend a system, based on coupled dynamic analysis, that will provide better motion response in a deep water environment.

By applying thrusters, total dynamic responses can be improved in terms of mooring line/riser top tensions and operation radii of platforms. Thrust must be added and adequately controlled in the following equation of motion in the horizontal plane (i.e. surge,

sway, and yaw).

$$m\ddot{\mathbf{X}} = \mathbf{F}_E + \mathbf{F}_M + \mathbf{F}_H + \mathbf{F}_T \tag{1.1}$$

where m represents platform's mass plus added mass, $\mathbf{X}$ displacement vector in x-, y-, z-directions, double dot 2nd time derivative, $\mathbf{F}_E$ environmental forces and moment, $\mathbf{F}_M$ mooring force, $\mathbf{F}_H$ hydrodynamic reaction forces and moment due to platform motions, and $\mathbf{F}_T$ thruster forces and moment acting on the platform. To minimize the error i.e. the difference between desired and measured location and heading angle of the platform, the thruster force $\mathbf{F}_T$ needs to be calculated, and a controller needs to be designed.

A coupled dynamic program, WINPOST-FPSO, has been developed, and it has been determined that the program is suitable for the analysis of FPSOs (Arcandra, 2001). For the next step, it is proposed that the following hypotheses should be tested:

1. Motion responses of thruster-assisted structures give smaller value of riser/mooring line stresses than those without a thruster.
2. The watch circle of a moored platform becomes smaller so that the structure has better global motion responses.

To test these two hypotheses, the following *Specific Aims* are proposed:

1. To develop and implement thrust control algorithm in the hull/mooring/riser time-domain coupled dynamic analysis program (WINPOST-FPSO) by tuning each gain of the P(I)D (Proportional-Integral-Derivative) controller.
2. To conduct case studies of hull/mooring/riser coupled motions of thruster-assisted moored platforms. The FPSO and the spar used for the DeepStar Project are adopted for this study.

3. To investigate the global motion response by means of spectral analysis and statistical analysis by comparing two cases: (1) A floating platform with a thruster-assisted system and 2) a floating platform without the system.
4. To determine how and why a thruster-assisted moored platform can (or cannot) be an effective solution in terms of mooring line stress reduction and improvement of the global motion response for deepwater system types.

In Chapter II the hydrodynamic loading, floating platform dynamics, and relevant numerical approaches for a solution of the derived mathematical formulation are reviewed. Chapters III and IV review position-keeping systems. Mooring line dynamics is addressed in Chapter III, and thruster-assisted position-keeping system is discussed in Chapter IV. Coupling between a hull and legs is briefly discussed in Chapter V. Lastly, Chapters VI and VII include two study cases: a thruster-assisted turret-moored FPSO and a thruster-assisted moored spar.

CHAPTER II

DYNAMICS OF A FLOATING STRUCTURE

2.1. Introduction

Onshore/offshore floating structures are destined to encounter waves, wind, and current. In this chapter, the wave loads and wave-induced motions of a floating structure are addressed. Both linear (1st order) and nonlinear (Stokes' 2nd order) wave theories and their corresponding potential forces acting on a floating structure are addressed. Formulation of motions of a floating platform and the relevant numerical approach for a solution of the derived mathematical equations follow Ran (2000).

2.2. Wave Theory Formulation and Solution

It is assumed that the fluid is irrotational and inviscid so that a velocity potential exists in the fluid domain. A pictorial illustration of a computational domain and coordinate system is shown in Fig. 2.1. A Cartesian coordinate system is employed such that the $z = 0$ line corresponds to the still water level, and z is positive upwards. The problem to solve is to determine the velocity potential that satisfies the Laplace equation:

$$\nabla^2 \Phi = 0 \qquad \text{in} \quad \Omega \tag{2.1}$$

where Ω denotes the fluid domain and $\Phi(x, y, z)$ the velocity potential function. Once the

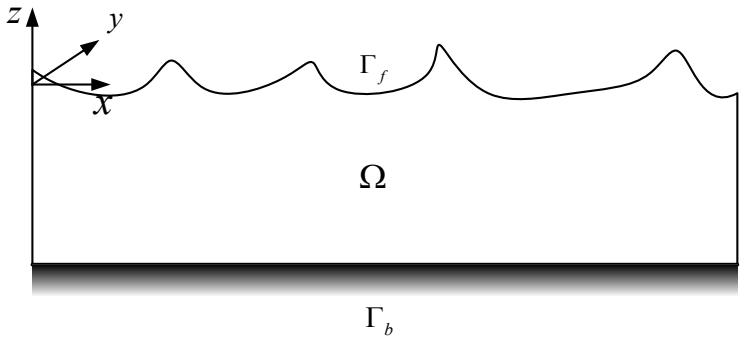

Fig. 2.1. Schematic diagram of domain and coordinate system.

potential function is obtained, the velocity and pressure field in the domain and on the boundaries can be calculated by the following equations:

$$\mathbf{v} = \nabla\Phi = \frac{\partial\Phi}{\partial x}\mathbf{i} + \frac{\partial\Phi}{\partial y}\mathbf{j} + \frac{\partial\Phi}{\partial z}\mathbf{k} \tag{2.2}$$

$$p = -\rho g z - \rho\frac{\partial\Phi}{\partial t} - \frac{1}{2}\rho\nabla^2\Phi \tag{2.3}$$

where $\mathbf{v} = u\mathbf{i} + v\mathbf{j} + w\mathbf{k}$ represents the particle velocity vector, ∇ gradient, p pressure, ρ fluid density, and g the gravitational acceleration. To solve the Laplace equation (2.1), the pertinent boundary conditions are to be defined.

For the bottom boundary condition, the condition of no flux through the bottom boundary Γ_b gives

$$\frac{\partial\Phi}{\partial n} = 0 \qquad \text{on} \quad \Gamma_b \tag{2.4}$$

where $\frac{\partial}{\partial n}$ denotes the normal derivative with respect to the bottom boundary so that it becomes $\frac{\partial}{\partial z}$ when a flat ocean bottom is considered. In addition, both the kinematic and dynamic free-surface boundary conditions (FSBCs) must be satisfied on the instantaneous free surface. The kinematic FSBC requires that the free-surface velocity should be equal to

the motion of free-surface particles,

$$\frac{D(z-\eta)}{Dt}=0 \qquad \text{on} \quad \Gamma_f \tag{2.5}$$

$$-\frac{\partial\eta}{\partial t}-u\frac{\partial\eta}{\partial x}-v\frac{\partial\eta}{\partial y}+w=0 \qquad \text{on} \quad \Gamma_f \tag{2.6}$$

where $z=\eta(x,y,t)$ is the free-surface elevation. In addition to the kinematic FSBC Eq. (2.6), the dynamic FSBC requires that the pressure on the free-surface must be uniform and equal to atmospheric pressure. The Bernoulli equation can be applied to describe this boundary condition,

$$\frac{\partial\Phi}{\partial t}+\frac{1}{2}\nabla^2\Phi+g\eta=-\frac{P_a}{\rho} \qquad \text{on} \quad \Gamma_f \tag{2.7}$$

where the atmospheric pressure P_a can be set to zero and

$$\nabla^2\Phi=\left(\frac{\partial\Phi}{\partial x}\right)^2+\left(\frac{\partial\Phi}{\partial y}\right)^2+\left(\frac{\partial\Phi}{\partial z}\right)^2. \tag{2.8}$$

Substituting Eq. (2.8) into Eq. (2.7) yields the dynamic FSBC,

$$\frac{\partial\Phi}{\partial t}+\frac{1}{2}\left\{\left(\frac{\partial\Phi}{\partial x}\right)^2+\left(\frac{\partial\Phi}{\partial y}\right)^2+\left(\frac{\partial\Phi}{\partial z}\right)^2\right\}+g\eta=0 \qquad \text{on} \quad \Gamma_f. \tag{2.9}$$

These are two ways to solve this boundary value problem (BVP) in the time domain: the analytical approach and the numerical approach. Because of the nonlinear terms in two FSBCs, i.e., Eqs. (2.6) and (2.9), the perturbation method as an analytical approach is commonly used under the assumption that the surface wave amplitude is small compared to the wave length and water depth. In this perturbation method, the potential solutions are approximate solutions which satisfy the FSBCs within the range of certain accuracy depending on the order of the perturbation parameter. The solution for Φ and the wave elevation can be expressed as follows with the form of a power series of a non-dimensional

perturbation parameter ε

$$\Phi = \sum_{n=1}^{\infty} \varepsilon^n \Phi^{(n)} \qquad \text{and} \qquad \eta = \sum_{n=1}^{\infty} \varepsilon^n \eta^{(n)} \tag{2.10}$$

where $\Phi^{(n)}$ is the n th order solution of Φ, and the ε is defined as

$$\varepsilon = \frac{2A}{L} = \frac{kA}{\pi} \tag{2.11}$$

where A is wave amplitude, L wave length, and k wave number. The linear and 2nd-order solutions are summarized in Table 2.1.

Table 2.1. Summary of Linear and 2nd-Order Solutions

Order	Velocity Potential (Φ) and Wave Elevation (η)
Linear	$\Phi^{(1)} = \mathrm{Re}\left[-\frac{igA}{\omega} \frac{\cosh k(z+d)}{\cosh kd} e^{i(\mathbf{k}\bullet\mathbf{x}-\omega t+\varphi)} \right]$
	$\eta^{(1)} = A\cos(\mathbf{k}\bullet\mathbf{x} - \omega t + \varphi)$
2nd order	$\Phi^{(2)} = \mathrm{Re}\left[\frac{3}{8}\omega A^2 \frac{\cosh 2k(z+d)}{\sinh^4 kd} e^{i(2\mathbf{k}\bullet\mathbf{x}-2\omega t+\varphi)} \right]$
	$\eta^{(2)} = A^2 k \frac{\cosh kd}{\sinh^3 kd}(2+\cosh 2kd)\cos(2\mathbf{k}\bullet\mathbf{x} - 2\omega t + \varphi)$

In Table 2.1 $\mathbf{k}$ and $\mathbf{x}$ are the wave number vector and position vector, respectively. And they are expressed as

$$\mathbf{k} = k\cos\theta\mathbf{i} + k\sin\theta\mathbf{j}$$

$$\mathbf{x} = x\mathbf{i} + y\mathbf{j},$$

and i denotes the imaginary symbol in complex numbers, A wave amplitude, ω wave frequency, φ arbitrary phase, θ incident wave angle with respect to the positive x-axis, k magnitude of the wave number, and d water depth.

Even though nonlinear higher-order solutions of surface waves give more accurate estimates for real seas, the linear theory is used to simulate irregular waves and to obtain statistical estimates based on computational efforts and difficulty in modeling of breaking waves (Faltinsen, 1990). The mathematical expression of the unidirectional waves, commonly called long-crested irregular seas, can be written as

$$\eta(\mathbf{x},t) = \mathrm{Re}\left[\sum_{j=1}^{N} A_j e^{i(\mathbf{k}_j \bullet \mathbf{x} - \omega_j t + \varphi_j)}\right] \tag{2.12}$$

where N and φ_j mean the number of wave components and random phase angle of wave component number j, respectively. The following relation can be used to obtain the wave amplitude A_j:

$$\frac{1}{2} A_j^2 = S(\omega_j)\Delta\omega \tag{2.13}$$

where $S(\omega_j)$ and $\Delta\omega$ represent a wave spectrum and a constant interval between successive angular frequencies, respectively.

In addition, it is also necessary to formulate wave particle velocities and accelerations in order to calculate hydrodynamic forces on a slender body facing waves using Morison's formula. Those velocities and accelerations in x-, y-, and z-directions can be expressed by the superposition based on the result of the linear regular waves given in Table 2.1. For instance, the horizontal particle velocity and acceleration is expressed as:

$$u(\mathbf{x},t) = \mathrm{Re}\left[\sum_{j=1}^{N} \frac{g k_j A}{\omega_j} \frac{\cosh k_j(z+d)}{\cosh k_j d} e^{i(\mathbf{k}_j \bullet \mathbf{x} - \omega_j t + \varphi_j)} \cos\theta\right] \tag{2.14}$$

$$\dot{u}(\mathbf{x},t) = \mathrm{Re}\left[\sum_{j=1}^{N} -i g k_j A \frac{\cosh k_j(z+d)}{\cosh k_j d} e^{i(\mathbf{k}_j \bullet \mathbf{x} - \omega_j t + \varphi_j)} \cos\theta\right] \tag{2.15}$$

A multi-directional sea (also called short-crested sea) can be expressed by employing the directional wave spectrum $S(\omega_j, \beta_k)$ as follows

$$\eta(\mathbf{x},t) = \mathrm{Re}\left[\sum_{j=1}^{N}\sum_{k=1}^{M}\left\{2S(\omega_j,\beta_k)\Delta\omega_j\Delta\beta_k\right\}^{1/2} e^{i(\mathbf{k}_{jk}\cdot\mathbf{x}-\omega_j t+\varphi_{jk})}\right] \tag{2.16}$$

where the directional wave spectrum $S(\omega_j, \beta_k)$ is a function of both wave frequency and direction and is expressed as follows

$$S(\omega,\beta) = S(\omega)G(\beta) \tag{2.17}$$

where $G(\beta)$ is called the directional spreading function, and β is measured counterclockwise from the wave direction with the most wave energy. The spreading function should satisfy the following condition

$$\int_{\beta=-\pi}^{\beta=\pi} G(\beta)d\beta = 1. \tag{2.18}$$

The cos-squared function and the cos-power function are the two commonly used directional spreading functions (Kamphuis, 2000).

2.3. Floating Structure Response in Regular Waves

To investigate motion responses of a floating structure, it is necessary to understand wave forces on the structure. Depending on the relative size of the structure compared to the ocean waves, diffraction theory and/or Morison's formula can be applied. In this section, these two fundamental concepts are discussed. Mathematical description of the responses of a floating structure follows the discussion.

2.3.1. Diffraction and Radiation Theory

To understand how the fluid field changes and how much wave forces act on a floating structure, a BVP needs to be established. First of all, the total velocity potential Φ must satisfy the Laplace equation, bottom boundary condition, and two FSBCs described in section 2.2. Based on the linearization, the total velocity potential can be expressed as the sum of three different potentials: incident wave potential Φ_I, diffraction potential Φ_D, and radiation potential Φ_R. As shown in Fig. 2.2, the diffraction potential Φ_D represents the disturbed fluid field of the incident wave by the body fixed at its undisturbed position. When a floating structure is placed in the fluid, two more additional conditions should be satisfied. These two conditions are:

$$\frac{\partial \Phi}{\partial n} = V_n \quad \text{on body surface} \tag{2.19}$$

where V_n is the normal velocity of the body at its surface.

$$\lim_{r\to\infty} \sqrt{r}\left(\frac{\partial \Phi_{D,R}}{\partial r} \pm ik\Phi_{D,R}\right) = 0 \tag{2.20}$$

where r is the radial distance from the center of the structure. Equation (2.20) is called the Sommerfeld radiation condition at far field, which describes the decay and vanish of the

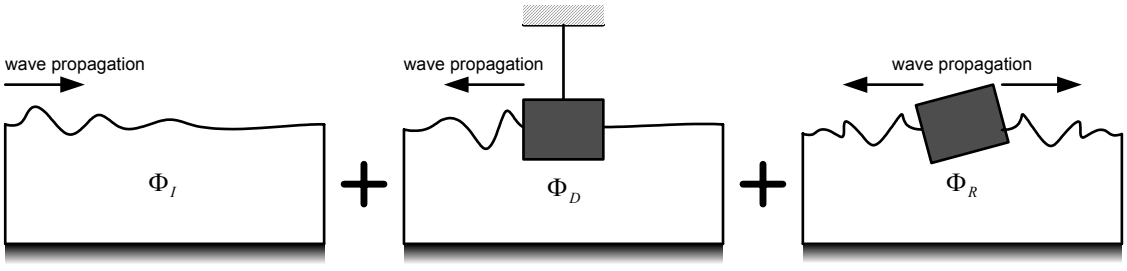

Fig. 2.2. Decomposition of three different potentials.

diffraction and radiation potentials as the distance from the structure becomes larger. If we consider mathematically weakly nonlinear waves, the total velocity potential can be expressed as a power series based on the perturbation method.

$$\Phi(\mathbf{x},t)=\sum_{n=1}^{\infty}\varepsilon^{n}\Phi^{(n)}(\mathbf{x},t)=\sum_{n=1}^{\infty}\varepsilon^{n}\left(\Phi_{I}^{(n)}+\Phi_{D}^{(n)}+\Phi_{R}^{(n)}\right) \tag{2.21}$$

where $\Phi^{(n)}$ is the n^{th}-order solution of velocity potential Φ. In this section, only up to the 2nd-order solutions will be discussed.

2.3.2. First-Order Boundary Value Problem

When $n=1$ in Eq. (2.21) (i.e., the 1st-order problem) and a regular wave case are considered, the total 1st-order velocity potential can be expressed as follows

$$\begin{aligned}\Phi^{(1)}(\mathbf{x},\mathrm{t})&=\varepsilon\left(\Phi_{\mathrm{I}}^{(1)}+\Phi_{\mathrm{D}}^{(1)}+\Phi_{\mathrm{R}}^{(1)}\right)\\&=\mathrm{Re}\left\{\left[\phi_{\mathrm{I}}^{(1)}(\mathrm{x},\mathrm{y},\mathrm{z})+\phi_{\mathrm{D}}^{(1)}(\mathrm{x},\mathrm{y},\mathrm{z})+\phi_{\mathrm{R}}^{(1)}(\mathrm{x},\mathrm{y},\mathrm{z})\right]\mathrm{e}^{-\mathrm{i}\omega\mathrm{t}}\right\}.\end{aligned} \tag{2.22}$$

The 1st-order incident wave potential $\phi_I^{(1)}$ may be regarded as known and was already mentioned in the previous section and written here again,

$$\phi_I^{(1)}=\mathrm{Re}\left[-\frac{igA}{\omega}\frac{\cosh k(z+d)}{\cosh kd}e^{i(\mathbf{k}\bullet\mathbf{x}-\omega t+\varphi)}\right]. \tag{2.23}$$

To solve the 1st-order BVP, the entire set of boundary conditions can be summarized as:

$$\nabla^{2}\phi_{\mathrm{D,R}}^{(1)}=0 \qquad \text{in } \Omega \ (z<0) \tag{2.24}$$

$$\left(-\omega^{2}+\mathrm{g}\frac{\partial}{\partial \mathrm{z}}\right)\phi_{\mathrm{D,R}}^{(1)}=0 \qquad \text{on } \Gamma_f \ (z=0) \tag{2.25}$$

$$\frac{\partial\phi_{\mathrm{D,R}}^{(1)}}{\partial \mathrm{z}}=0 \qquad \text{on } \Gamma_b \ (z=-d) \tag{2.26}$$

$$\frac{\partial\phi_{\mathrm{D}}^{(1)}}{\partial \mathrm{n}}=-\frac{\partial\phi_{\mathrm{I}}^{(1)}}{\partial \mathrm{n}} \qquad \text{on } \Gamma_{body} \tag{2.27}$$

$$\frac{\partial \phi_R^{(1)}}{\partial n} = -i\omega \mathbf{n} \cdot \left(\boldsymbol{\xi}^{(1)} + \boldsymbol{\alpha}^{(1)} \times \mathbf{r} \right) \qquad \text{on } \Gamma_{body} \tag{2.28}$$

$$\lim_{r \to \infty} \frac{1}{\sqrt{r}} \left(\frac{\partial}{\partial r} \pm ik \right) \phi_{D,R}^{(1)} = 0 \qquad \text{at far field} \tag{2.29}$$

where **r** represents the position vector of an arbitrary point of the body surface, *r* the radial distance from the origin, and $\mathbf{n} = (n_x, n_y, n_z)$ the unit normal vector pointing out of the fluid domain. The translational $\boldsymbol{\Xi}$ and rotational (Θ) 1st-order motions of the floating body have the following forms:

$$\boldsymbol{\Xi}^{(1)}(t) = \mathrm{Re}\left[\boldsymbol{\xi}^{(1)} e^{-i\omega t} \right], \qquad \boldsymbol{\xi}^{(1)} = \left(\xi_1^{(1)}, \xi_2^{(1)}, \xi_3^{(1)} \right) \tag{2.30}$$

$$\boldsymbol{\Theta}^{(1)} = \mathrm{Re}\left[\boldsymbol{\alpha}^{(1)} e^{-i\omega t} \right], \qquad \boldsymbol{\alpha}^{(1)} = \left(\alpha_1^{(1)}, \alpha_2^{(1)}, \alpha_3^{(1)} \right) \tag{2.31}$$

where the subscripts 1, 2, and 3 in Eq. (2.30) denote translational motions, i.e., surge, sway, and heave, respectively, and in Eq. (2.31) rotational motions, i.e., roll, pitch, and yaw, respectively. To establish a variable of six degrees of freedom, the following definition can be used:

$$\varsigma_j = \xi_j^{(1)} \qquad \text{for } j = 1, 2, 3 \tag{2.32}$$

$$\varsigma_j = \alpha_{j-3}^{(1)} \qquad \text{for } j = 4, 5, 6. \tag{2.33}$$

Now, the simplified radiation potential can be written as:

$$\phi_R^{(1)} = i\omega \sum_{j=1}^{6} \varsigma_j \phi_j^{(1)} \tag{2.34}$$

where $\phi_j^{(1)}$ represents the velocity potential of the rigid body motion with unit amplitude in the j^{th} mode in the absence of the incident waves. The body boundary condition Eq. (2.28) becomes

$$\frac{\partial \phi_j^{(1)}}{\partial n} = \mathbf{n}_j \qquad j = 1, 2, 3 \tag{2.35}$$

$$\frac{\partial \phi_j^{(1)}}{\partial n} = \left(\mathbf{r} \times \mathbf{n}\right)_{j-3} \qquad j = 4, 5, 6. \tag{2.36}$$

The 1st-order hydrodynamic pressure $P^{(1)}(t)$ and free surface elevation $\eta^{(1)}(t)$ can be given as follows

$$P^{(1)} = -\rho \frac{\partial \Phi^{(1)}}{\partial t} \tag{2.37}$$

$$\eta^{(1)} = -\frac{1}{g} \frac{\partial \Phi^{(1)}}{\partial t} \qquad \text{at } z = 0. \tag{2.38}$$

By the direct integration over the wetted surface $S(t)$ of the body, the total forces and moments on the body can be calculated as

$$\mathbf{F}(t)_j = \begin{cases} \iint_{S_B} P n_j \, dS & j = 1, 2, 3 \\ \iint_{S_B} P(\mathbf{r} \times \mathbf{n})_j \, dS & j = 4, 5, 6 \end{cases} \tag{2.39}$$

where, for the 1st-order problem, the wetted body surface S_B means the wetted body surface when the body stays still in calm water because of the condition of the 1st-order BVP. The 1st-order hydrodynamic force can be expressed as a sum of three physically different terms:

$$\mathbf{F}^{(1)} = \mathbf{F}_{HS}^{(1)} + \mathbf{F}_{R}^{(1)} + \mathbf{F}_{EX}^{(1)} \tag{2.40}$$

where $\mathbf{F}_{HS}^{(1)}$ represents hydrostatic restoring force/moment, $\mathbf{F}_{R}^{(1)}$ force/moment occurred by the radiation potential, and $\mathbf{F}_{EX}^{(1)}$ wave exciting force/moment caused by both incident and diffraction potentials and the interaction between the two.

First, the hydrostatic restoring force $\mathbf{F}_{HS}^{(1)}$ is interpreted as the force caused by the hydrostatic pressure change due to the body motions, and it can be written as

$$\mathbf{F}_{HS}^{(1)} = -\mathbf{K}\boldsymbol{\zeta}^{(1)} \tag{2.41}$$

where $\zeta^{(1)}$ denotes the 1st-order displacement column vector, and $\mathbf{K}_{6\times6}$ the hydrostatic restoring stiffness matrix, whose components are defined as follows:

$$K_{33} = \rho g A_w \tag{2.42}$$

$$K_{34} = K_{43} = \rho g A_w y_f \tag{2.43}$$

$$K_{35} = K_{53} = -\rho g A_w x_f \tag{2.44}$$

$$K_{44} = \rho g \left(S_{22} + \forall z_b\right) - mgz_g \tag{2.45}$$

$$K_{45} = K_{54} = -\rho g S_{12} \tag{2.46}$$

$$K_{46} = -\rho g \forall x_b + mgx_g \tag{2.47}$$

$$K_{55} = \rho g \left(S_{11} + \forall z_b\right) - mgz_g \tag{2.48}$$

$$K_{56} = -\rho g \forall y_b + mgy_g \tag{2.49}$$

$$\text{Otherwise } K_{ij} = 0 \tag{2.50}$$

where A_w represents water plane area, x_f and y_f the coordinates of the center of the floating structure in the horizontal plane, $\forall$ the volume of the displaced water, (x_g, y_g, z_g) the coordinates of the center of gravity, (x_b, y_b, z_b) the coordinates of the center of buoyancy, and

$$S_{11} = \iint_{S_B} x^2 dS \tag{2.51}$$

$$S_{22} = \iint_{S_B} y^2 dS \tag{2.52}$$

$$S_{12} = \iint_{S_B} xy dS . \tag{2.53}$$

Secondly, the radiation force $\mathbf{F}_R^{(1)}$ is related to the added mass and damping load. This force is created by the generated outgoing waves caused by the forced motion of the

body. The hydrodynamic added mass and damping loads due to the 1st-order harmonic motion $\boldsymbol{\zeta}^{(1)}$ can be expressed as

$$\mathbf{F}_{R}^{(1)} = \mathrm{Re}\left[\mathbf{f}\boldsymbol{\zeta}^{(1)}\right] \tag{2.54}$$

where

$$\mathbf{f} = f_{ij} = -\rho\iint_{S_B} \frac{\partial \phi_i}{\partial n}\phi_j dS \qquad i,\ j = 1,2,\cdots,6. \tag{2.55}$$

The matrix $\mathbf{f}_{6\times 6}$ is a function of the exciting frequency ω. It can be expressed in terms of the added mass and damping coefficients as follows:

$$f_{ij} = -\omega^2 M_{ij}^{a} - i\omega C_{ij} \tag{2.56}$$

$$\mathbf{F}_{R}^{(1)} = \mathrm{Re}\left(\mathbf{M}^{a}\ddot{\boldsymbol{\zeta}}^{(1)} + \mathbf{C}\dot{\boldsymbol{\zeta}}^{(1)}\right) \tag{2.57}$$

where $\mathbf{M}_{6\times 6}^{a}$ represents the added mass and $\mathbf{C}_{6\times 6}$ the damping coefficient.

Lastly, the wave exciting force $\mathbf{F}_{EX}^{(1)}$ in Eq. (2.40) can be expressed by

$$\mathbf{F}_{EX}^{(1)} = \mathrm{Re}\left\{-\rho A e^{-i\omega t}\iint_{S_B}\left(\phi_I + \phi_D\right)\frac{\partial \phi_j}{\partial n}dS\right\}. \tag{2.58}$$

A linear transfer function (LTF) can be defined as the *exciting force*-to-*incident wave amplitude* ratio (i.e., $\mathbf{F}_{EX}^{(1)} / A$), which accounts for the 1st-order diffraction force on the body.

2.3.3. Second-Order Boundary Value Problem

When n=2 in Eq. (2.21) (i.e., the 2nd-order perturbation problem) and bi-chromatic incident wave case (ω_j and ω_k) are considered, the 2nd-order velocity potential can be

expressed as follows:

$$\begin{aligned}\Phi^{(2)}(\mathbf{x},t) &= \varepsilon^2\left(\Phi_I^{(2)}+\Phi_D^{(2)}+\Phi_R^{(2)}\right)\\ &= \mathrm{Re}\left\{\left[\phi_I^- + \phi_D^- + \phi_R^-\right]e^{-i\omega^- t} + \left[\phi_I^+ + \phi_D^+ + \phi_R^+\right]e^{-i\omega^+ t}\right\},\end{aligned} \tag{2.59}$$

where superscripts (+) and (–) represent the sum- and difference-frequency terms, i.e., $\omega^+ = \omega_j + \omega_k$ and $\omega^- = \omega_j - \omega_k$. The 2nd-order incident wave potential was already mentioned in Table 2.1. For bi-chromatic waves, the sum- and difference-frequency 2nd-order incident wave potentials can be written as

$$\phi_I^+ = \frac{1}{2}\left(\gamma_{jk}^+ + \gamma_{kj}^+\right)\frac{\cosh k^+(z+d)}{\cosh k^+ h}e^{i\mathbf{k}^+\cdot\mathbf{x}} \tag{2.60}$$

$$\phi_I^- = \frac{1}{2}\left(\gamma_{jk}^- + \gamma_{kj}^{-*}\right)\frac{\cosh k^-(z+d)}{\cosh k^- d}e^{i\mathbf{k}^-\cdot\mathbf{x}} \tag{2.61}$$

$$\gamma_{jk}^+ = -\frac{igA_jA_k}{2\omega_j}\frac{k_j^2\left(1-\tanh^2 k_j d\right)+2k_jk_k\left(1-\tanh k_j d\tanh k_k d\right)}{\nu^+ - k^+\tanh k^+ d} \tag{2.62}$$

$$\gamma_{jk}^- = -\frac{igA_jA_k^*}{2\omega_j}\frac{k_j^2\left(1-\tanh^2 k_j d\right)+2k_jk_k\left(1+\tanh k_j d\tanh k_k d\right)}{\nu^- - k^-\tanh k^- d}, \tag{2.63}$$

where the asterisk mark (*) represents a complex conjugate, $\nu^\pm = \dfrac{\left(\omega^\pm\right)^2}{g}$, $\mathbf{k}^\pm = \mathbf{k}_j \pm \mathbf{k}_k$, and $k^\pm = \left|\mathbf{k}^\pm\right|$.

To obtain the 2nd-order diffraction potential $\phi_D^\pm$, the following BVP can be established,

$$\nabla^2\phi_D^\pm = 0 \qquad \text{in } \Omega \text{ with calm free surface} \tag{2.64}$$

$$\left(-\omega^{\pm 2} + g\frac{\partial}{\partial z}\right)\phi_D^\pm = Q^\pm \qquad \text{on } \Gamma_f \ (z=0) \tag{2.65}$$

$$\frac{\partial\phi_D^\pm}{\partial z} = 0 \qquad \text{on } \Gamma_b \ (z=-d) \tag{2.66}$$

$$\frac{\partial \phi_D^{(1)}}{\partial n} = \frac{\partial \phi_I^{(1)}}{\partial n} + B^{\pm} \qquad \text{on} \quad \Gamma_{body} \tag{2.67}$$

Radiation boundary condition at the far field (2.68)

The sum- and difference-frequency free-surface forcing terms $Q^{\pm}$ can be expressed as:

$$Q^{+} = \frac{1}{2}\left(q_{jk}^{+} + q_{kj}^{+}\right), \quad Q^{-} = \frac{1}{2}\left(q_{jk}^{-} + q_{kj}^{-*}\right), \tag{2.69}$$

where

$$q_{jk}^{+} = -\frac{i\omega_j}{2g}\phi_k^{(1)}\left(-\omega_j^2\frac{\partial \phi_j^{(1)}}{\partial z} + g\frac{\partial^2 \phi_j^{(1)}}{\partial z^2}\right) + i\omega_k \nabla\phi_j^{(1)} \cdot \nabla\phi_k^{(1)} - q_{IIjk}^{+} \tag{2.70}$$

$$q_{jk}^{-} = -\frac{i\omega_j}{2g}\phi_k^{(1)*}\left(-\omega_j^2\frac{\partial \phi_j^{(1)}}{\partial z} + g\frac{\partial^2 \phi_j^{(1)}}{\partial z^2}\right) + i\omega_k \nabla\phi_j^{(1)} \cdot \nabla\phi_k^{(1)*} - q_{IIjk}^{-}. \tag{2.71}$$

The sum- and difference-frequency body-surface forcing terms $B^{\pm}$ can be written as:

$$B^{+} = \frac{1}{2}\left(b_{jk}^{+} + b_{kj}^{+}\right), \quad B^{-} = \frac{1}{2}\left(b_{jk}^{-} + b_{kj}^{-*}\right), \tag{2.72}$$

where

$$b_{jk}^{+} = -\frac{1}{2}\mathbf{n}\cdot\left(\zeta_k^{(1)} \cdot \nabla\right)\nabla\phi_j^{(1)}, \quad b_{jk}^{-} = \frac{1}{2}\mathbf{n}\cdot\left(\zeta_k^{(1)*} \cdot \nabla\right)\nabla\phi_j^{(1)}. \tag{2.73}$$

To get the radiation boundary condition Eq. (2.68), the separation of a homogeneous solution and a particular solution is considered for the 2nd-order diffraction potential $\phi_D^{\pm}$. The detailed formulation and explanation of this radiation boundary condition can be found in Kim and Yue (1990).

The BVP for the 2nd-order radiation, the following boundary condition must be satisfied,

$$\frac{\partial \phi_R^{\pm}}{\partial n} = -\omega^{\pm}\mathbf{n}\cdot\left(\boldsymbol{\xi}^{\pm} + \boldsymbol{\alpha}^{\pm} \times \mathbf{r}\right) \qquad \text{on} \quad \Gamma_{body}, \tag{2.74}$$

where $\xi^{\pm}$ and $\boldsymbol{\alpha}^{\pm}$ represent the 2nd-order translational and rotational motions of a body, respectively, at the sum and difference frequencies. Therefore, the solutions for the $\phi_R^{\pm}$ for the 2nd-order hydrodynamic coefficients are identical to those of the 1st-order radiation problem at the sum and difference frequencies.

2.3.4. Second-Order Potential Forces

To calculate the 2nd-order forces and moments, the 2nd-order pressure in the fluid domain must be known. The pressure can be expressed on the basis of the solutions of the sum- and difference-frequency 2nd-order potentials mentioned in the previous section. Hence, the 2nd-order pressure can be expressed by:

$$P^{(2)} = -\rho\frac{\partial\Phi^{(2)}}{\partial t} - \frac{1}{2}\rho\left(\nabla\Phi^{(1)}\right)^2. \tag{2.75}$$

In a bi-chromatic wave case, the above equation can also be expressed as:

$$P^{(2)} = \mathrm{Re}\left[A_j A_k p_{jk}^{+} e^{-i\omega^{+}t} + A_j A_k^{*} p_{jk}^{-} e^{-i\omega^{-}t}\right], \tag{2.76}$$

where $p_{jk}^{\pm}$ is defined as the sum- and difference-frequency quadratic transfer functions (QTFs) for the pressure. In general, the complete 2nd-order pressure can be distinguished by two separate terms:

$$p_{jk}^{\pm} = p_{qjk}^{\pm} + p_{pjk}^{\pm}, \tag{2.77}$$

where the $p_q^{\pm}$ and $p_p^{\pm}$ represent the two distinguishable contributions from the quadratic products of the 1st-order potentials and the 2nd-order potentials themselves, respectively. These two components can be expressed as

$$p_{qjk}^{+} = \left[-\frac{1}{4}\rho_0 \nabla\phi_j^{(1)} \cdot \nabla\phi_k^{(1)} \right] \Big/ A_j A_k \tag{2.78}$$

$$p_{qjk}^{-} = \left[-\frac{1}{4}\rho_0 \nabla\phi_j^{(1)} \cdot \nabla\phi_k^{(1)*} \right] \Big/ A_j A_k^* \tag{2.79}$$

$$p_{pjk}^{\pm} = \frac{1}{2}\rho_0 i\omega^{\pm}\phi^{\pm} \Big/ \left(A_j A_k, A_j A_k^* \right). \tag{2.80}$$

In a similar way, used for the expression of the linear 1st-order forces, the 2nd-order hydrodynamic forces can be expressed as a sum of different components as follows:

$$\mathbf{F}^{(2)} = \mathbf{F}_p^{(2)} + \mathbf{F}_q^{(2)} + \mathbf{F}_R^{(2)} + \mathbf{F}_{HS}^{(2)}, \tag{2.81}$$

where vectors $\mathbf{F}_p^{(2)}$, $\mathbf{F}_q^{(2)}$, $\mathbf{F}_R^{(2)}$ and $\mathbf{F}_{HS}^{(2)}$ represent the forces originated from the 2nd-order potentials, the quadratic products of 1st-order quantities, the 2nd-order radiation potentials, and the 2nd-order hydrostatic coefficients, respectively. The 2nd-order force and moment can be written as:

$$\mathbf{F}_p^{(2)} = -\rho \iint_{S_B} \frac{\partial \Phi^{(2)}}{\partial t} \mathbf{n} dS \tag{2.82}$$

$$\begin{aligned} \mathbf{F}_q^{(2)} = & -\rho \iint_{S_B} \left[\frac{1}{2}\left(\nabla\Phi^{(1)} \right)^2 + \left(\boldsymbol{\Xi}^{(1)} + \boldsymbol{\alpha}^{(1)} \times \mathbf{r} \right) \frac{\partial}{\partial t}\left(\nabla\Phi^{(1)} \right) \right] \mathbf{n} dS \\ & + \frac{1}{2}\rho g \int_{WL} \left[\eta_r^{(1)} - \left(\xi_3^{(1)} + y\alpha_1^{(1)} - x\alpha_2^{(1)} \right) \right] \mathbf{N} dl + \boldsymbol{\alpha}_1^{(1)} \times \mathbf{F}^{(1)} \\ & - \rho g A_w \left[\alpha_2^{(1)} \left(x_f \alpha_1^{(1)} + y_f \alpha_2^{(1)} \right) \right] \mathbf{k}, \end{aligned} \tag{2.83}$$

where $\eta_r^{(1)}$ denotes the 1st-order relative wave height, $\mathbf{N} = \mathbf{n} \Big/ \sqrt{(1 - n_3^2)}$, and $\mathbf{k}$ the unit vector in the z-direction. The first two terms in the right-hand side of Eq. (2.81) can be called the 2nd-order wave exciting forces, and re-written as follows:

$$\mathbf{F}_{EX}^{(2)} = \mathbf{F}_p^{(2)} + \mathbf{F}_q^{(2)}. \tag{2.84}$$

In the presence of bi-chromatic waves, the 2nd-order wave exciting forces have the

following form,

$$\mathbf{F}_{EX}^{(2)} = \mathrm{Re}\sum_{j=1}^{2}\sum_{k=1}^{2}\left[A_j A_k f_{jk}^{+} e^{-i\omega^{+}t} + A_j A_k^{*} f_{jk}^{-} e^{-i\omega^{-}t} \right] \tag{2.85}$$

$$f_{jk}^{\pm} = f_{pjk}^{\pm} + f_{qjk}^{\pm} \tag{2.86}$$

where $f_{jk}^{\pm}$ is defined as the complete sum- and difference-frequency exciting force QTFs.

The wave damping and added mass at the sum and difference frequency can be obtained from the 1st-order solutions, while the 2nd-order radiation and hydrostatic forces, $\mathbf{F}_{R}^{(2)}$ and $\mathbf{F}_{HS}^{(2)}$, are similar to those of the 1st-order problem.

2.3.5. WAMIT: A BEM-Based Hydrodynamic Analysis Program

In general, since it is impossible to get the analytic solutions of various practical problems, several hydrodynamic analysis programs, such as WINTCOL, higher-order BEM-based program HOBEM and WAMIT, have been developed. In this study, WAMIT is used to obtain the linear and the 2nd-order wave exciting forces on floating structures.

WAMIT is a hydrodynamic diffraction/radiation analysis program developed by MIT. Detailed mathematical background, usage of the program, and calculation examples can be found in *WAMIT User Manual*. An example of mesh generation for the input of WAMIT is shown in Fig. 2.3. The results of the diffraction/radiation analysis in WAMIT include added mass and damping coefficients, LTFs, and QTFs. These results, then, are fed to the program called WINPOST which is a mooring/riser analysis program developed by Texas A&M University.

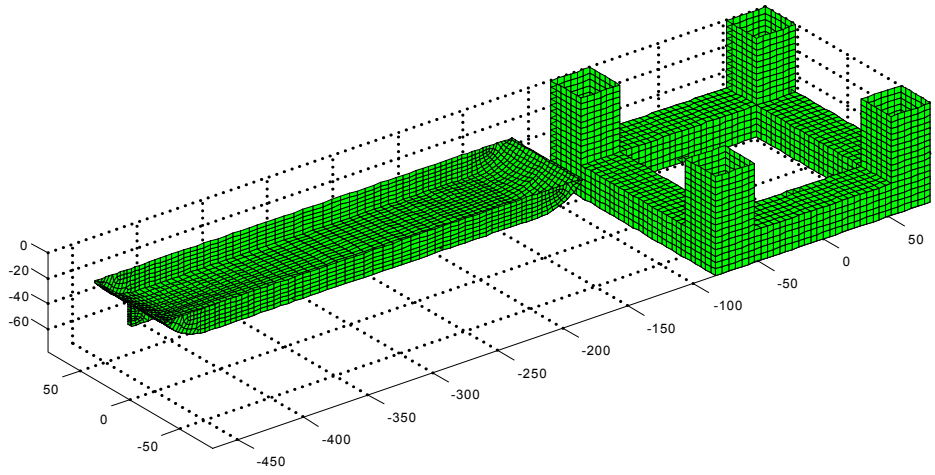

Fig. 2.3. An example of mesh generation for hydrodynamic calculations.

2.3.6. Wave Exciting Loads in Time Domain

In general, the linear and 2nd-order hydrodynamic forces on a body due to stationary Gaussian random seas can be expressed as a two-term Volterra series in time domain as follows:

$$F^{(1)}(t)+F^{(2)}(t)=\int_{-\infty}^{\infty} h_1(\tau)\eta(t-\tau)d\tau+\int_{-\infty}^{\infty}\int_{-\infty}^{\infty} h_2(\tau_1,\tau_2)\eta(t-\tau_1)\eta(t-\tau_2)d\tau_1 d\tau_2 , \quad (2.87)$$

where $\eta(t)$ is the wave elevation at the reference point, and $h_1(\tau)$ and $h_2(\tau_1,\tau_2)$ are the linear and quadratic impulse response functions, respectively. In the case of unidirectional waves with N wave components, the wave exciting forces from incident wave potential and diffraction potential can be expressed as

$$\mathbf{F}_I^{(1)}(t)=\mathrm{Re}\left[\sum_{j=1}^{N} A_j \mathbf{L}(\omega_j)e^{i\omega_j t}\right] \quad (2.88)$$

$$\mathbf{F}_I^{(2)}(t)=\mathrm{Re}\left[\sum_{j=1}^{N}\sum_{k=1}^{N} A_j A_k^{*}\mathbf{D}(\omega_j,-\omega_k)e^{i(\omega_j-\omega_k)t}+\sum_{j=1}^{N}\sum_{k=1}^{N} A_j A_k S(\omega_j,\omega_k)e^{i(\omega_j+\omega_k)t}\right], \quad (2.89)$$

where $\mathbf{L}(\omega_j)$ represents LTF, and $\mathbf{D}(\omega_j,-\omega_k)$ and $\mathbf{S}(\omega_j,+\omega_k)$ difference- and sum-frequency QTFs, respectively. As time marches on, the waves generated by the motion of a body propagate outward from the body. These traveling waves continuously affect the fluid pressure field, and the affected pressure field changes the forces acting on the body. With this reasoning, the concept of *memory effects* is introduced. The pressure forces acting on the body from radiation potential can be expressed as

$$\mathbf{F}_R(t) = -\mathbf{m}(\infty)\ddot{\boldsymbol{\zeta}}(t) - \int_{-\infty}^{t} \mathbf{R}(t-\tau)\dot{\boldsymbol{\zeta}}(\tau)d\tau \tag{2.90}$$

The above equation is a convolution integral over the past time history of the fluid field. The kernel $\mathbf{R}(t)$, called *retardation function*, is related to the frequency domain solution of the radiation problem and can be written as

$$\mathbf{R}(t) = \frac{2}{\pi}\int_0^{\infty} \mathbf{C}(\omega)\frac{\sin\omega t}{\omega}d\omega \tag{2.91}$$

where $\mathbf{C}(\omega)$ is wave damping coefficients at frequency ω. The added mass coefficients at infinite frequency can be written as

$$\mathbf{m}(\infty) = \mathbf{m}^a(\omega) - \int_0^{\infty} \mathbf{R}(t)\cos\omega t dt, \tag{2.92}$$

where $\mathbf{m}^a(\omega)$ is the added mass at frequency ω.

2.3.7. Morison's Equation for Slender Elements

When slender elements, for instance the trusses of a truss spar and risers of a platform, are considered, the diffraction force may not be dominant compared to the viscous force.

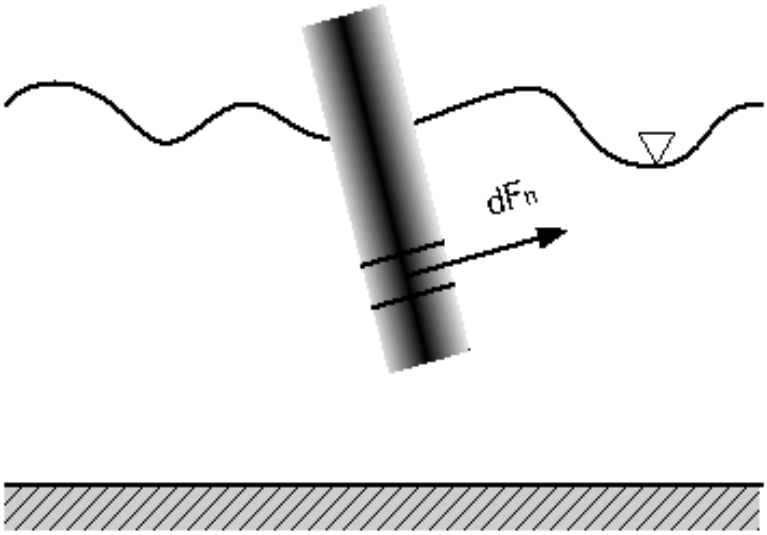

Fig. 2.4. Schematic diagram of force calculation by modified Morison's equation.

Here, the slenderness of an element is related to the ratio D/L (diameter-to-wave length). To obtain the horizontal force per unit length on a strip of the floating cylindrical body with the diameter of D shown in Fig. 2.4, a modified Morison's equation can be used

$$dF_n = C_M \rho \frac{\pi D^2}{4} \dot{u}_n - C_a \rho \frac{\pi D^2}{4} \ddot{x}_n + C_D \frac{1}{2} \rho (u_n - \dot{x}_n)\left|u_n - \dot{x}_n\right|, \tag{2.93}$$

where dF_n represents the force per unit length normal to the body surface, C_M inertia coefficient, ρ mass density of the water, C_a added mass coefficient, C_D drag coefficient, $\dot{u}_n$ and u_n fluid acceleration and velocity normal to the body, and $\ddot{x}_n$ and $\dot{x}_n$ normal acceleration and velocity of the structure.

In practical cases, Morison's equation may be used for the calculation of the wave/current forces acting on the truss of a truss spar, while the diffraction theory is used to calculate the wave/current forces on hulls of FPSOs or spars, and columns and pontoons of TLPs.

2.4. Motions of a Floating Body

To predict the motions of a floating body, every external force should be known first. In the case of a freely floating body, the hydrodynamic force described in the previous sections including wave and current forces, along with the gravitational force are the external forces that need to be considered. According to Newton's 2nd law, once the entire external force, as a vector sum, acting on a body is known, the motion of the body can be predicted. Therefore, the following two equations of momentum conservation are the governing equations for predicting the motions of a floating body,

$$\frac{d(m\dot{\mathbf{x}}_c)}{dt} = \mathbf{f} \tag{2.94}$$

$$\mathbf{I}\frac{d\boldsymbol{\omega}}{dt} + \boldsymbol{\omega}\times(\mathbf{I}\boldsymbol{\omega}) = \mathbf{m}, \tag{2.95}$$

where m represents the constant mass of the floating body, $\dot{\mathbf{x}}_c$ the velocity at the center of gravity of the body, $\mathbf{f}$ entire external force, $\mathbf{I}$ moment of inertia, $\boldsymbol{\omega}$ angular velocity, and $\mathbf{m}$ external moment. If a problem with small rotational motions is considered, the nonlinear term $\boldsymbol{\omega}\times(\mathbf{I}\boldsymbol{\omega})$ can be negligible, and the above two equations can be combined into one equation as follows

$$\mathbf{M}\ddot{\boldsymbol{\xi}} = \mathbf{F}, \tag{2.96}$$

where $\mathbf{M}$ represents the body mass matrix that is expressed as

$$\mathbf{M} = \begin{bmatrix} m & 0 & 0 & 0 & mz_G & -my_G \\ & m & 0 & -mz_G & 0 & mx_G \\ & & m & my_G & -mx_G & 0 \\ & & & I_{11} & I_{12} & I_{13} \\ & sym & & & I_{22} & I_{23} \\ & & & & & I_{33} \end{bmatrix}. \tag{2.97}$$

In addition, $\ddot{\boldsymbol{\zeta}}$ represents the body acceleration, $\mathbf{F}$ the external force/moment vector, m the body mass, (x_G, y_G, z_G) the coordinate of the center of gravity, and the moment of inertia is defined by

$$I_{ij=}\iiint_{V_B} \rho_B[\mathbf{x}\cdot\mathbf{x}\delta_{ij} - x_i x_j]dV\,, \tag{2.98}$$

where V_B denotes the body volume, ρ_B the body-mass density, and δ_{ij} the Kronecker delta function. When nonlinear effects become an important consideration or a detail design of a platform is sought, a time-domain dynamic analysis is favored, and the equation of motion in time domain can be expressed as follows:

$$\left[\mathbf{M} + \mathbf{M}^{\mathbf{a}}(\infty)\right]\ddot{\boldsymbol{\zeta}} + \mathbf{K}\boldsymbol{\zeta} = \mathbf{F}_{\mathrm{I}}(\mathrm{t}) + \mathbf{F}_{\mathrm{c}}(\mathrm{t},\dot{\boldsymbol{\zeta}}) + \mathbf{F}_{\mathrm{n}}(\mathrm{t},\dot{\boldsymbol{\zeta}})\,, \tag{2.99}$$

where $\mathbf{M}^{\mathbf{a}}(\infty)$ denotes added mass, $\mathbf{F}_{\mathrm{I}}(\mathrm{t})$ is wave exciting force, $\mathbf{F}_{\mathrm{n}}(\mathrm{t},\dot{\boldsymbol{\zeta}})$ nonlinear drag force from Morison's equation, and $\mathbf{F}_{\mathrm{c}}(\mathrm{t},\dot{\boldsymbol{\zeta}})$ radiation force as follows:

$$\mathbf{F}_{\mathrm{c}}(\mathrm{t},\dot{\boldsymbol{\zeta}}) = -\int_{-\infty}^{\mathrm{t}} \mathbf{R}(\mathrm{t}-\tau)\dot{\boldsymbol{\zeta}}\mathrm{d}\tau\,. \tag{2.100}$$

2.5. Numerical Implementation of the Equation of Motion

Runge-Kutta methods have been the standard methods for the numerical solution of ordinary differential equations (ODEs). However, when considering a large number of function evaluations per step, coupled with significant improvement in computer technology, multi-step methods are now preferred because the large function evaluations may be removed. The most general k-step method is

$$\sum_{m=0}^{k} \alpha_m y_{n+1-m} + \sum_{m=0}^{k} \beta_m f(x_{n+1-m}, y_{n+1-m}) = 0 \tag{2.101}$$

and is defined by the number of steps k and the parameters α_m and β_m (Ferziger, 1981). If $\beta_0 = 0$, the method is explicit; otherwise it is implicit. It is called Adams method when $\alpha_0 = 1$ and $\alpha_1 = -1$. The implicit methods are called Adams-Moulton methods, and the explicit ones are called Adams-Bashforth methods. The 1st-order Adams-Bashforth method is the Euler method, and the 1st- and the 2nd-order Adams-Moulton methods are the backward Euler and the trapezoidal rule, respectively. In this study, both the 2nd-order Adams-Moulton method and the 2nd-order Adams-Bashforth method are used.

To numerically solve Eq. (2.99), the following set of two 1st-order ODEs needs to be considered:

$$\overline{\mathbf{M}}\dot{\boldsymbol{\xi}} = \mathbf{F}_{\mathrm{I}}(\mathrm{t}) + \mathbf{F}_{\mathrm{c}}(\mathrm{t}, \dot{\boldsymbol{\zeta}}) + \mathbf{F}_{\mathrm{n}}(\mathrm{t}, \dot{\boldsymbol{\zeta}}) - \mathbf{K}\boldsymbol{\zeta} \tag{2.102}$$

$$\dot{\boldsymbol{\zeta}} = \boldsymbol{\xi}, \tag{2.103}$$

where $\overline{\mathbf{M}} = \mathbf{M} + \mathbf{M}^{\infty}(\infty)$. Applying the 2nd-order Adams-Moulton method (i.e., a trapezoidal rule), the following two equations are obtained

$$\begin{aligned} \overline{\mathbf{M}}\boldsymbol{\xi}^{(\mathrm{n+1})} = \overline{\mathbf{M}}\boldsymbol{\xi}^{(\mathrm{n})} &+ \frac{\Delta \mathrm{t}}{2}\left(\mathbf{F}_{\mathrm{I}}^{(\mathrm{n+1})} + \mathbf{F}_{\mathrm{I}}^{(\mathrm{n})} + \mathbf{F}_{\mathrm{c}}^{(\mathrm{n+1})} + \mathbf{F}_{\mathrm{c}}^{(\mathrm{n})} + \mathbf{F}_{\mathrm{n}}^{(\mathrm{n+1})} + \mathbf{F}_{\mathrm{n}}^{(\mathrm{n})}\right) \\ &- \frac{\Delta \mathrm{t}}{2}\mathbf{K}\left(\boldsymbol{\zeta}^{(\mathrm{n+1})} + \boldsymbol{\zeta}^{(\mathrm{n})}\right) \end{aligned} \tag{2.104}$$

$$\boldsymbol{\xi}^{(\mathrm{n+1})} = \frac{2}{\Delta \mathrm{t}}\left(\boldsymbol{\zeta}^{(\mathrm{n+1})} - \boldsymbol{\zeta}^{(\mathrm{n})}\right) - \boldsymbol{\xi}^{(\mathrm{n})}. \tag{2.105}$$

To calculate $\boldsymbol{\xi}$ and $\boldsymbol{\zeta}$ at step (n+1), iterative computation is required because of the two terms $\mathbf{F}_{\mathrm{c}}^{(\mathrm{n+1})}$ and $\mathbf{F}_{\mathrm{n}}^{(\mathrm{n+1})}$ in Eq. (2.104). This iterative computation can be removed by applying the 2nd-order Adams-Bashforth method to the two terms described in the following Eqs. (2.106) and (2.107):

$$\int_{t^{(n)}}^{t^{(n+1)}} \mathbf{F}_c dt = \frac{\Delta t}{2}\left(3\mathbf{F}_c^{(n)} - \mathbf{F}_c^{(n-1)}\right) \quad \text{for} \quad n \neq 0, \qquad \int_{t^{(0)}}^{t^{(1)}} \mathbf{F}_c dt = \Delta t \mathbf{F}_c^{(0)} \quad \text{for} \quad n = 0, \tag{2.106}$$

$$\int_{t^{(n)}}^{t^{(n+1)}} \mathbf{F}_n dt = \frac{\Delta t}{2}\left(3\mathbf{F}_n^{(n)} - \mathbf{F}_n^{(n-1)}\right) \quad \text{for} \quad n \neq 0, \qquad \int_{t^{(0)}}^{t^{(1)}} \mathbf{F}_n dt = \Delta t \mathbf{F}_n^{(0)} \quad \text{for} \quad n = 0. \tag{2.107}$$

Eqs. (2.104) through (2.107) can be re-arranged to obtain the following final equation:

$$\begin{aligned}\left[\frac{4}{\Delta t^2}\overline{\mathbf{M}} + \mathbf{K}\right]\Delta\boldsymbol{\zeta} = \frac{4}{\Delta t^2}\overline{\mathbf{M}}\boldsymbol{\xi}^{(n)} + \left(\mathbf{F}_I^{(n+1)} + \mathbf{F}_I^{(n)}\right) + \left(3\mathbf{F}_c^{(n)} - \mathbf{F}_c^{(n-1)}\right) \\ + \left(3\mathbf{F}_n^{(n)} - \mathbf{F}_n^{(n-1)}\right) - 2\mathbf{K}\boldsymbol{\zeta}^{(n)} + 2\mathbf{F}_0\end{aligned} \tag{2.108}$$

where $\Delta\boldsymbol{\zeta} = \boldsymbol{\zeta}^{(n+1)} - \boldsymbol{\zeta}^{(n)}$, and $\mathbf{F}_0$ represents a constant force, for instance, the net buoyancy force on a floating platform to account for the mooring forces.

In this approach, the stability of the numerical methods used for the solution of the ODEs would be important. According to stability analysis, the 2nd-order Adams-Bashforth is conditionally stable, while the 2nd-order Adams-Moulton method is always stable. Therefore, the time interval (Δt) for the time domain dynamic analyses of a platform must be controlled to keep numerical simulations within stability limits. However, since a platform/mooring coupled system and a more rigorous, in general, stability condition in the mooring line analysis are considered, the time interval required for the mooring line analysis may not cause any numerical instability problems in the computational routine for the analysis of the platform (Ran, 2000).

CHAPTER III

POSITION KEEPING SYSTEM I: MOORING LINE DYNAMICS

3.1. Introduction

In the previous chapter, the external loads caused primarily by water and the corresponding responses of a floating body were discussed. Position keeping is one of the major concerns in design criteria of an offshore floating structure since the platform may drift away from a target location without the help of a position-keeping device. Two position-keeping methods, i.e., mooring alone and thruster-assisted position-keeping, will be discussed in Chapters III and IV, successively.

In this chapter, mooring line/riser dynamics and its numerical implementation for mooring line/riser analysis are addressed. The risers are considered as the same type of structure as mooring lines from the structural point of view. However, even though those risers are originally targeted for production, drilling, oil/gas export, etc., they may be able to significantly affect the dynamic responses of a floating platform due to the increase of drag force and inertia in deep waters.

For the analysis of both the mooring line and riser, the slender rod theory is commonly used. The elastic rod theory derived by Nordgen (1974) and Garret (1982) was applied, and the derivation/formulation follows Ran (2000). The finite element method is used to numerically solve the equations of the motion of a rod. For formulation of dynamic

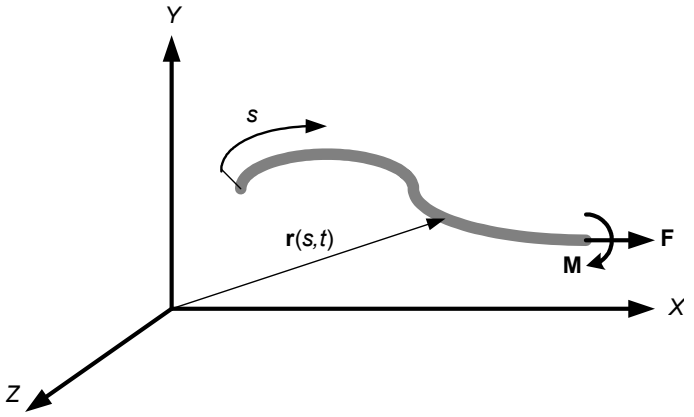

Fig. 3.1. Notation and coordinate of rod.

problems, only time-domain formulation is mentioned, and all of the case studies deal with time-domain analysis. Finally, the vertical elastic spring model is addressed for the consideration of the interaction between the seabed and the mooring line.

3.2. Equations of Motion of a Rod

As shown in Fig. 3.1, for the expression of the shape and state of a rod in a 3-D Cartesian coordinate system, we can define the position vector $\mathbf{r}(s,t)$, where s is the arc-length along the rod, and t is time. By simply applying Newton's 2nd law, the following two equations of motion can be written,

$$\mathbf{F}' + \mathbf{q} = \rho\ddot{\mathbf{r}}(s,t) \tag{3.1}$$

$$\mathbf{M}' + \mathbf{r}' \times \mathbf{F} + \mathbf{m} = \mathbf{0}, \tag{3.2}$$

where the prime and dot denote the differentiation with respect to arc-length (s) and time (t), respectively, $\mathbf{F}$ resultant force, $\mathbf{M}$ resultant moment, $\mathbf{q}$ applied force per unit length, ρ rod mass per unit length, and $\mathbf{m}$ applied moment per unit length. The resultant moment $\mathbf{M}$ can be expressed as

$$\mathbf{M} = \mathbf{r}' \times \mathrm{EI}\mathbf{r}'' + \mathrm{H}\mathbf{r}', \tag{3.3}$$

where EI is the bending stiffness, and H is the torque. Substituting Eq. (3.3) into Eq. (3.2) yields

$$\mathbf{r}' \times \left[\left(\mathrm{EI}\mathbf{r}'' \right)' + \mathbf{F} \right] + \mathrm{H}'\mathbf{r}' + \mathrm{H}\mathbf{r}'' + \mathbf{m} = \mathbf{0}, \tag{3.4}$$

and the scalar product of the above equation with $\mathbf{r}'$ yields

$$\mathrm{H}' + \mathbf{m} \cdot \mathbf{r}' = \mathbf{0}. \tag{3.5}$$

By assuming that both H and $\mathbf{m}$ are negligible, Eq. (3.4) can be rewritten as

$$\mathbf{r}' \times \left[\left(\mathrm{EI}\mathbf{r}'' \right)' + \mathbf{F} \right] = \mathbf{0}. \tag{3.6}$$

Introducing a scalar function $\lambda(\mathrm{s,t})$, the resultant force in Eq. (3.6) can be rewritten as

$$\mathbf{F} = -\left(\mathrm{EI}\mathbf{r}'' \right)' + \lambda \mathbf{r}'. \tag{3.7}$$

The scalar product of Eq. (3.7) with $\mathbf{r}'$ results in

$$\lambda(\mathrm{s,t}) = \mathbf{F} \cdot \mathbf{r}' + \left(\mathrm{EI}\mathbf{r}'' \right)' \cdot \mathbf{r}' = \mathrm{T}(\mathrm{s,t}) - \mathrm{EI}\kappa^2, \tag{3.8}$$

where $T(s,t) = \mathbf{F} \cdot \mathbf{r}'$ is the local tension, and the κ ($\kappa^2 = -\mathbf{r}' \cdot \mathbf{r}'''$) is the local curvature of the rod. Substituting Eq. (3.7) to Eq. (3.1) yields

$$-\left(\mathrm{EI}\mathbf{r}'' \right)'' + \left(\lambda \mathbf{r}' \right)' + \mathbf{q} = \rho \ddot{\mathbf{r}}. \tag{3.9}$$

When the inextensibility condition of a rod is assumed, the following equation must be satisfied:

$$\mathbf{r}' \cdot \mathbf{r}' = 1. \tag{3.10}$$

If a linear and small extensible rod is considered, the above condition can be expanded as

$$\frac{1}{2}\left(\mathbf{r}' \cdot \mathbf{r}' - 1 \right) = \frac{\tilde{\mathrm{T}}}{\mathrm{AE}} \approx \frac{\lambda + \mathrm{P}_{\mathrm{res}}}{\mathrm{AE}}, \tag{3.11}$$

where $\tilde{T}(= T + P_{res})$ is *effective tension,* AE axial stiffness, T actual tension, and P_{res} the force caused by hydrostatic pressure expressed by

$$P_{res} = A_o p_o - A_i p_i, \tag{3.12}$$

where $A_o p_o$ denotes the force expressed by the multiplication of the external cross sectional area A_o and external pressure p_o, and $A_i p_i$ comes from the internal pressure.

The scalar function called Lagrange multiplier $\lambda(s,t)$ and the position vector $\mathbf{r}(s,t)$ can be obtained by solving Eqs. (3.9) through (3.12) with appropriate initial conditions, boundary conditions, and applied force $\mathbf{q}$, which can be expressed by the sum of three different kinds of forces,

$$\mathbf{q} = \mathbf{w} + \mathbf{F}^s + \mathbf{F}^d, \tag{3.13}$$

where $\mathbf{w}$ represents the weight of a rod, $\mathbf{F}^s$ the hydrostatic force, and $\mathbf{F}^d$ the hydrodynamic force, and all of these forces are dimensionally forces per unit length.

First, the hydrostatic force can be written as follows:

$$\mathbf{F}^s = \mathbf{B} - \left(P\,\mathbf{r}'\right)', \tag{3.14}$$

where $\mathbf{B}$ is the buoyant force of the rod per unit length and P the hydrostatic pressure at the point $\mathbf{r}$ on the rod.

Secondly, to calculate the hydrodynamic force $\mathbf{F}^d$, following Morison's equation is used:

$$\begin{aligned} \mathbf{F}^d &= -C_a \ddot{\mathbf{r}}^n + C_m \dot{\mathbf{V}}^n + C_d \left|\mathbf{V}^n - \dot{\mathbf{r}}^n\right|\left(\mathbf{V}^n - \dot{\mathbf{r}}^n\right) \\ &= -C_a \ddot{\mathbf{r}}^n + \overline{\mathbf{F}}^d, \end{aligned} \tag{3.15}$$

where C_a, C_m, and C_d denote the added mass coefficient per unit length, the inertia force coefficient per unit length per unit normal acceleration, and the drag force coefficient per unit length per unit normal velocity, respectively. $\dot{\mathbf{V}}^n$ and $\mathbf{V}^n$ are fluid acceleration

and velocity normal to the rod centerline, which are to be obtained from

$$\dot{\mathbf{V}}^{\mathrm{n}} = \dot{\mathbf{V}} - \left(\dot{\mathbf{V}} \cdot \dot{\mathbf{r}}\right)\mathbf{r}' \tag{3.16}$$

$$\mathbf{V}^{\mathrm{n}} = \left(\mathbf{V} - \dot{\mathbf{r}}\right) - \left[\left(\mathbf{V} - \dot{\mathbf{r}}\right) \cdot \mathbf{r}'\right]\mathbf{r}', \tag{3.17}$$

where $\dot{\mathbf{V}}$ and $\mathbf{V}$ are the total water particle acceleration and velocity, respectively, at the center line of the rod by assuming that the fluid field is undisturbed by the rod. In Eq. (3.15), $\ddot{\mathbf{r}}^{\mathrm{n}}$ and $\dot{\mathbf{r}}^{\mathrm{n}}$ are the components of the rod acceleration and velocity normal to its centerline and can be obtained from the following equations:

$$\dot{\mathbf{r}}^{\mathrm{n}} = \dot{\mathbf{r}} - \left(\dot{\mathbf{r}} \cdot \mathbf{r}'\right)\mathbf{r}' \tag{3.18}$$

$$\ddot{\mathbf{r}}^{\mathrm{n}} = \ddot{\mathbf{r}} - \left(\ddot{\mathbf{r}} \cdot \mathbf{r}'\right)\mathbf{r}' . \tag{3.19}$$

Combining Eqs. (3.13), (3.14) and (3.15) with (3.10), the equation of the rod with its weight, hydrostatic, and hydrodynamic forces in water becomes

$$\rho\ddot{\mathbf{r}} + \mathrm{C_a}\rho_{\mathrm{w}}\ddot{\mathbf{r}}^{\mathrm{n}} + \left(\mathrm{EI}\mathbf{r}''\right)'' - \left(\tilde{\lambda}\mathbf{r}'\right)' = \tilde{\mathbf{w}} + \overline{\mathbf{F}}^{\mathrm{d}}, \tag{3.20}$$

where $\tilde{\lambda} = \tilde{\mathrm{T}} - \mathrm{EI}\kappa^2$ and $\tilde{\mathbf{w}} = \mathbf{w} + \mathbf{B}$. $\tilde{\mathbf{w}}$ is called *effective weight*. Eq. (3.20) is the equation of motion of a rod in fluid.

3.3. Finite Element Formulation

To numerically solve Eqs. (3.11) and (3.20), a finite element method can be employed. As the first step in the procedure of the use of finite element methods, the *weak form* of Eq. (3.20) can be written as

$$\int_0^L \left[A_l(\rho \ddot{r}_i + C_a \ddot{r}_i^n) + EIA_i'' r_i'' + \tilde{\lambda} A_i' r_i' - A_i(\tilde{w}_i + \bar{F}_i^d) \right] ds = EIr_i'' A_l' \Big|_0^L + \left[\tilde{\lambda} r_i' - (Br_i'')' \right] A_l \Big|_0^L , \tag{3.21}$$

where A_l is called *interpolation function*, and $U_{il}(t)$ is the coefficient that needs to be solved. Also, they are defined as

$$r_i(s,t) = A_l(s) U_{il}(t) \tag{3.22}$$

and

$$\delta r_i(s,t) = A_l(s) \delta U_{il}(t) . \tag{3.23}$$

The condition of extensibility, i.e., Eq. (3.11), can also be written as

$$\int_0^L P_m \left[\frac{1}{2}(r_r' r_r' - 1) - \frac{\lambda}{AE} \right] ds = 0 , \tag{3.24}$$

where P_m is an interpolation function, and is defined as

$$\lambda(s,t) = P_m(s) \lambda_m(t) . \tag{3.25}$$

The cubic shape functions for $A_l(s)$ and quadratic shape functions for $P_m(s)$ are selected, and they are defined as

$$\begin{aligned} A_1 &= 1 - 3\xi^2 + 2\xi^3 \\ A_2 &= L\left(\xi - 2\xi^2 + \xi^3\right) \\ A_3 &= 3\xi^2 - 2\xi^3 \\ A_4 &= L\left(-\xi^2 + \xi^3\right) \end{aligned} \tag{3.26}$$

$$\begin{aligned} P_1 &= 1 - 3\xi^2 + 2\xi^3 \\ P_2 &= 4\xi(1 - \xi) \\ P_3 &= \xi(2\xi - 1), \end{aligned} \tag{3.27}$$

where $\xi = \frac{s}{L}$. In addition, the parameters U_{il} and λ_m are defined as follows:

$$U_{i1} = r_i(0,t), \quad U_{i2} = r_i'(0,t)$$
$$U_{i3} = r_i(L,t), \quad U_{i4} = r_i'(L,t) \tag{3.28}$$

$$\lambda_1 = \lambda(0,t), \quad \lambda_2 = \lambda(\frac{L}{2},t), \quad \lambda_3 = \lambda(L,t), \tag{3.29}$$

where λ represents the line tension at the end node and the midpoint. Substituting Eqs. (3.19), (3.22) and (3.25) into Eq. (3.21) yields

$$\left(M_{ijlk} + M^a_{ijlk}\right)\ddot{U}_{jk} + \left(K^1_{ijlk} + \lambda_n K^2_{nijlk}\right)U_{jk} - F_{il} = 0, \tag{3.30}$$

where

$$M_{ijlk} = \int_0^L \rho A_l A_k \delta_{ij} ds \tag{3.31}$$

$$M^a_{ijlk} = C_a\left[\int_0^L A_l A_k \delta_{ij} ds - \int_0^L \left(A_l A_k A_s' A_t' ds\right) U_{it} U_{js}\right] \tag{3.32}$$

$$K^1_{ijlk} = \int_0^L EIA_l'' A_k'' \delta_{ij} ds \tag{3.33}$$

$$K^2_{nijlk} = \int_0^L P_n A_l' A_k' \delta_{ij} ds \tag{3.34}$$

$$F_{il} = \int_0^L \left(\tilde{w}_i + \overline{F}_i^d\right) A_l ds \tag{3.35}$$

and δ_{ij} represents the Kronecker Delta function, M_{ijlk} mass, M^a_{ijlk} added mass, K^1_{ijlk} material stiffness coming from the bending stiffness, and K^2_{nijlk} stiffness from the tension and the curvature of a rod. Eq. (3.24) can be written as

$$G_m = A_{mil} U_{kl} U_{ki} - B_m - C_{mt}\lambda_t = 0, \tag{3.36}$$

where

$$A_{mil} = \frac{1}{2}\int_0^L P_m A_i A_l ds$$

$$B_m = \frac{1}{2}\int_0^L P_m ds$$

$$C_{mt} = \frac{1}{AE}\int_0^L P_m P_t ds\,.$$

Following sections will deal with how to solve Eqs. (3.30) through (3.36) numerically.

3.4. Formulation for Static Problem

Since the word "static" means time-independency, the time-dependent term $\left(M_{ijlk} + M^a_{ijlk}\right)\ddot{U}_{jk}$ in Eq. (3.30) is removed for static problems.

Letting

$$R_{il} = \left(K^1_{ijlk} + \lambda_n K^2_{nijlk}\right)U_{jk} - F_{il}\,, \tag{3.37}$$

we can rewrite Eqs. (3.30) and (3.36) as

$$R_{il} = 0 \tag{3.38}$$

$$G_m = 0\,, \tag{3.39}$$

where F_{il} is a static forcing term from the gravity force, drag force from the steady current and other applied static forces on the rod. The Newton-Raphson iterative method is used to solve the above nonlinear equations. By means of Taylor series expansion, Eqs. (3.38) and (3.39) can be expressed as follows:

$$R^{(n+1)}_{il} = R^{(n)}_{il} + \frac{\partial R_{il}}{\partial U_{jk}}\left(\Delta U_{jk}\right) + \frac{\partial R_{il}}{\partial \lambda_n}\left(\Delta\lambda_n\right) \tag{3.40}$$

$$G^{(n+1)}_{m} = G^{(n)}_{m} + \frac{\partial G_{m}}{\partial U_{jk}}\left(\Delta U_{jk}\right) + \frac{\partial G_{m}}{\partial \lambda_n}\left(\Delta\lambda_n\right). \tag{3.41}$$

Re-arranging each term of the above two equations, we can write the following equation in a matrix form

$$\begin{bmatrix} K^{t0(n)}_{ijlk} & K^{t1(n)}_{iln} \\ D^{t0(n)}_{mjk} & D^{t1(n)}_{mn} \end{bmatrix}\begin{Bmatrix} \Delta U_{jk} \\ \Delta\lambda_n \end{Bmatrix} = \begin{Bmatrix} -R^{(n)}_{il} \\ -G^{(n)}_{m} \end{Bmatrix}, \tag{3.42}$$

where

$$K_{ijlk}^{t0(n)} = K_{ijlk}^{1} + \lambda_n^{(n)} K_{nijlk}^{2}$$

$$K_{iln}^{t1(n)} = K_{nijlk}^{2} U_{jk}^{(n)} = \left(\int_0^L P_n A_l' A_k' ds \right) U_{jk}^{(n)}$$

$$D_{mjk}^{t0(n)} = \left(\int_0^L P_m A_k' A_p' ds \right) U_{jp}^{(n)}$$

$$D_{mn}^{t1(n)} = \int_0^L \left(-\frac{1}{AE} P_m P_n \right) ds$$

$$R_{il}^{(n)} = \left(K_{ijlk}^{1} + \lambda_n K_{nijlk}^{2} \right) U_{jK}^{(n)} - F_{il}$$

$$G_m^{(n)} = \int_0^L P_m \left[\frac{1}{2} \left\{ (A_p' U_{rp}^{(n)})(A_q' U_{rq}^{(n)}) - 1 \right\} - \frac{1}{AE} P_t \lambda_t^{(n)} \right] ds .$$

Eq. (3.42) can be written in the following compact form based on the systematic renumbering suggested by Ran (2000)

$$\mathbf{K}^{(n)} \Delta \mathbf{y} = \mathbf{F}^{(n)}, \tag{3.43}$$

where the column vector **y** consists of U_{ij} and λ_m, and is expressed as

$$\mathbf{y} = \left[U_{11} \; U_{12} \; U_{21} \; U_{22} \; U_{31} \; U_{32} \; \lambda_1 \; \lambda_2 \; U_{13} \; U_{14} \; U_{23} \; U_{24} \; U_{33} \; U_{34} \; \lambda_3 \right]^T . \tag{3.44}$$

In Eq. (3.43), $\mathbf{K}$ is stiffness matrix, and the force vector $\mathbf{F}$ is expressed as

$$\mathbf{F} = -\left[R_{11} \; R_{12} \; R_{21} \; R_{22} \; R_{31} \; R_{32} \; G_1 \; G_2 \; R_{13} \; R_{14} \; R_{23} \; R_{24} \; R_{33} \; R_{34} - G_3 \right]^T \tag{3.45}$$

and

$$\Delta \mathbf{y} = \mathbf{y}^{(n+1)} - \mathbf{y}^{(n)} . \tag{3.46}$$

The superscript (T) in Eqs. (3.44) and (3.45) denotes transpose of a vector. Gauss elimination method is applied to solve Eq. (3.43). Although the resultant forces at the node ends of an element are removed in the element formulation due to cancellation, usually the internal forces are required to analyze the corresponding stresses of the mooring lines for a

structural design. Based on Eq. (3.21), the resultant force vector can be written as

$$\mathbf{F}^{r}=\begin{bmatrix} -\lambda r_1'+\left(Br_1''\right)'|_{s=0} \\ -EIr_1''|_{s=0} \\ -\lambda r_2'+\left(Br_2''\right)'|_{s=0} \\ -EIr_2''|_{s=0} \\ -\lambda r_3'+\left(Br_3''\right)'|_{s=0} \\ -EIr_3''|_{s=0} \\ 0 \\ 0 \\ \lambda r_1'-\left(Br_1''\right)'|_{s=L} \\ EIr_1''|_{s=L} \\ \lambda r_2'-\left(Br_2''\right)'|_{s=L} \\ EIr_2''|_{s=L} \\ \lambda r_3'-\left(Br_3''\right)'|_{s=L} \\ EIr_3''|_{s=L} \\ 0 \end{bmatrix}=\begin{bmatrix} -N_1^{[1]} \\ -L_1^{[1]} \\ -N_2^{[1]} \\ -L_2^{[1]} \\ -N_3^{[1]} \\ -L_3^{[1]} \\ 0 \\ 0 \\ N_1^{[2]} \\ L_1^{[2]} \\ N_2^{[2]} \\ L_2^{[2]} \\ N_3^{[2]} \\ L_3^{[2]} \\ 0 \end{bmatrix}, \tag{3.47}$$

where superscripts [1] and [2] denote the first end ($s=0$) and the second end ($s=L$) of an element, respectively, and $\mathbf{N}=\left\{N_1,N_2,N_3\right\}^{T}$ the nodal resultant force. In addition, $\mathbf{L}=\left\{L_1,L_2,L_3\right\}^{T}$ is related to the nodal resultant moment $\mathbf{M}$ $(=\mathbf{L}\times\mathbf{r}')$. By solving for the nodal variables U and λ, the resultant force can be obtained as follows:

$$\mathbf{F}^{r}=-\mathbf{F}^{(n+1)}. \tag{3.48}$$

3.5. Time-Domain Formulation for Dynamic Problem

To formulate a finite element method for dynamic problems, the time-dependent term $\left(M_{ijlk}+M_{ijlk}^{a}\right)\ddot{U}_{jk}$ in Eq. (3.30) that was removed for static problems needs to be included, and the whole Eq. (3.30) and the stretch condition Eq. (3.36) have to be reconstructed.

First, by letting

$$\hat{M}_{ijlk} = M_{ijlk} + M^{a}_{ijlk}$$

$$F^{1}_{il} = K^{1}_{ijlk} U_{jk}$$

$$F^{2}_{il} = \lambda_n K^{2}_{nijlk} U_{jk}$$

$$\hat{F}_{il} = -F^{1}_{il} - F^{2}_{il} + F_{il},$$

the equation of motion, Eq. (3.30), becomes

$$\hat{M}_{ijlk} \ddot{U}_{jk} = \hat{F}_{il}. \tag{3.49}$$

To numerically solve the above 2nd-order ODE, we can construct two 1st-order ODEs as follows:

$$\hat{M}_{ijlk} \dot{V}_{jk} = \hat{F}_{il} \tag{3.50}$$

$$\dot{U}_{jk} = V_{jk}. \tag{3.51}$$

Since $\hat{M}_{ijlk}$ is a function of time, the term $\hat{M}^{(n+\frac{1}{2})}_{ijlk}$, which is the mass at $t = t^{(n)} + \Delta t/2$, can be assumed as constant in time interval $\Delta t\ (= t^{(n+1)} - t^{(n)})$ to be a constant for simplified integration of Eq. (3.50). For one step time integration, the above two first-order ODEs can be integrated from $t = t^{(n)}$ to $t = t^{(n+1)}$, and they are written as follows:

$$\hat{M}^{(n+\frac{1}{2})}_{ijlk} \dot{V}^{(n+1)}_{jk} - \hat{M}^{(n+\frac{1}{2})}_{ijlk} \dot{V}^{(n)}_{jk} = \int_{t(n)}^{t(n+1)} \hat{F}_{il} dt \tag{3.52}$$

$$U^{(n+1)}_{jk} = U^{(n)}_{jk} + \frac{\Delta t}{2}\left(V^{(n+1)}_{jk} + V^{(n)}_{jk}\right), \tag{3.53}$$

where the 1st-order Adams-Moulton (or a trapezoidal method) was employed to obtain Eq. (3.53). By applying the trapezoidal method to the term of RHS in Eq. (3.52) and re-

arranging, the following final form of the equation of motion can be obtained

$$\left[\frac{4}{(\Delta t)^2}\hat{M}_{ijlk}^{(n+\frac{1}{2})}+K_{ijlk}^{1}+\lambda_n^{(n-\frac{1}{2})}K_{nijlk}^{2}\right]\Delta U_{jk}+2K_{nijlk}^{2}U_{jk}^{(n)}\Delta\lambda_n$$
$$=\frac{4}{\Delta t}\hat{M}_{ijlk}^{(n+\frac{1}{2})}V_{jk}^{(n)}+\left(3F_{il}^{(n)}-F_{il}^{(n-1)}\right)-2\left(K_{ijlk}^{1}+\lambda_n^{(n-\frac{1}{2})}K_{nijlk}^{2}\right)U_{jk}^{(n)}, \tag{3.54}$$

where $\Delta\lambda_n=\lambda_n^{(n+\frac{1}{2})}-\lambda_n^{(n-\frac{1}{2})}$. For the approximate mass term $\hat{M}_{ijlk}^{(n+\frac{1}{2})}$, the following Adams-Bashforth method is employed:

$$\hat{M}_{ijlk}^{(n+\frac{1}{2})}=\frac{1}{2}\left(3\hat{M}_{ijlk}^{(n)}-\hat{M}_{ijlk}^{(n-1)}\right). \tag{3.55}$$

Secondly, by applying Taylor series expansion, the stretch condition, Eq. (3.36), can be obtained as follows

$$0=2G_m^{(n+1)}\approx 2G_m^{(n)}+2\frac{\partial G_m^{(n)}}{\partial U_{jk}}\Delta U_{jk}+2\frac{\partial G_m^{(n)}}{\partial\lambda_n}\Delta\lambda_n$$
$$=2G_m^{(n)}+2K_{mijlk}^{2}U_{il}\Delta U_{jk}+D_{mn}^{t1(n)}\Delta\lambda_n. \tag{3.56}$$

In the same way, applied to a static problem, Eqs. (3.54) and (3.56) can be re-arranged in a matrix form as follows:

$$\begin{bmatrix}\hat{K}_{ijlk}^{t0(n)} & \hat{K}_{iln}^{t1(n)}\\ \hat{D}_{mjk}^{t0(n)} & \hat{D}_{mn}^{t1(n)}\end{bmatrix}\begin{Bmatrix}\Delta U_{jk}\\ \Delta\lambda_n\end{Bmatrix}=\begin{Bmatrix}-\hat{R}_{il}^{(n)}\\ -\hat{G}_m^{(n)}\end{Bmatrix}, \tag{3.57}$$

where

$$\hat{K}_{ijlk}^{t0(n)}=\frac{2}{\Delta t}\left(3\hat{M}_{ijlk}^{(n)}-\hat{M}_{ijlk}^{(n-1)}\right)+K_{ijlk}^{1}+\lambda_n^{(n-1)}K_{nijlk}^{2}$$

$$\hat{K}_{iln}^{t1(n)}=2K_{nijlk}^{2}U_{jk}^{(n)}$$

$$\hat{D}_{mjk}^{t0(n)}=2K_{nijlk}^{2}U_{il}^{(n)}$$

$$\hat{D}_{mn}^{t1(n)}=2D_{mn}^{t1(n)}$$

$$\hat{R}_{il} = \frac{2}{\Delta t}\left(3\hat{M}_{ijlk}^{(n)} - \hat{M}_{ijlk}^{(n-1)}\right)V_{jk}^{(n)} + \left(3F_{il}^{(n)} - F_{il}^{(n-1)}\right) - 2K_{ijlk}^{1}U_{jk}^{(n)} - 2\lambda_{n}^{\left(n-\frac{1}{2}\right)}K_{nijlk}^{2}U_{jk}^{(n)}$$

$$\hat{G}_{m}^{(n)} = 2G_{m}^{(n)}.$$

The superscripts in parentheses mean the time step. Ultimately, Eq. (3.57) can be re-written as

$$\hat{\mathbf{K}}^{(n)}\Delta\mathbf{y} = \hat{\mathbf{F}}^{(n)} \qquad \text{at each time step n,} \tag{3.58}$$

where the matrix $\hat{\mathbf{K}}$ and the two vectors $\mathbf{y}$ and $\hat{\mathbf{F}}$ have the same structures mentioned in Eqs. (3.44) and (3.45). Also, the nodal resultant force can be calculated based on the following equation:

$$\mathbf{F}^{r} = -\hat{\mathbf{F}}^{(n+1)}. \tag{3.59}$$

As Ran (2000) pointed out, a time-domain analysis is preferred for the problems in which the nonlinear effect is one of the main concerns since the analysis directly solves the nonlinear terms without any linearization procedure or assumption. However, the time-domain analysis may require such serious computational effort as large computation time. On the other hand, a frequency-domain analysis can be competitive in that matter, even though it may not be able to appropriately capture the nonlinear effects better than the time-domain analysis.

3.6. Modeling of Seabed

When a mooring line or a riser has a catenary shape, the interaction between a leg and seabed requires a proper modeling of the physical characteristics of the touching part. In

the numerical modeling, the seabed is modeled as a quadratic elastic spring in vertical direction based on numerical factors, and the horizontal friction between the line and the seabed is ignored. By letting the mean water surface as the x-y plane, the interaction force $\mathbf{f} \quad (= f_x\mathbf{i} + f_y\mathbf{j} + f_z\mathbf{k})$ between the leg and the seabed can be expressed as

$$f_x = 0, \qquad f_y = 0, \qquad f_z = \begin{cases} c(r_z - D)^2 & \text{for } (r_z - D) < 0 \\ 0 & \text{for } (r_z - D) \geq 0, \end{cases} \tag{3.60}$$

where D denotes water depth or vertical distance between the seabed and the origin of the coordinate, and r_z the z-component of the line position vector $\mathbf{r}$. Now, the equation of motion of a rod, i.e., Eq. (3.30), needs to be modified by adding F^{seabed} and becomes

$$\left(M_{ijlk} + M^a_{ijlk}\right)\ddot{U}_{jk} + \left(K^1_{ijlk} + \lambda_n K^2_{nijlk}\right)U_{jk} = F_{il} + F^{seabed}_{il}, \tag{3.61}$$

where

$$\begin{aligned} F^{seabed}_{il} &= \int_0^L A_l f_i ds \\ &= \begin{cases} \int_0^L A_l \delta_{i3} c(\delta_{i3} A_k U_{jk} - D)^2 ds & \text{for } (r_z - D) < 0 \\ 0 & \text{for } (r_z - D) \geq 0 \end{cases} \end{aligned} \tag{3.62}$$

and

$$\delta_{i3} = \begin{cases} 1 & \text{for i=3} \\ 0 & \text{otherwise.} \end{cases}$$

For static problems, the stiffness matrix of the seabed is constructed by applying Newton's method, and it is written as follows:

$$\begin{aligned} K^3_{ijlk} &= \frac{\partial F^{seabed}_{il}}{\partial U_{jk}} \\ &= \begin{cases} \int_0^L 2A_l \delta_{i3} c \delta_{j3} A_k (\delta_{m3} A_n U^{(n)}_{mn} - D) ds & \text{for } (r_z - D) < 0 \\ 0 & \text{for } (r_z - D) \geq 0. \end{cases} \end{aligned} \tag{3.63}$$

The newly defined stiffness, K^{3}_{ijlk}, originating from the consideration of the effect of the seabed, is added to K^{t0}_{ijlk} which is defined in Eq. (3.42). The other three terms in Eq. (3.42), K^{t1}_{iln}, D^{t0}_{mjk} and D^{t1}_{mn}, are not affected by the seabed.

For a time domain analysis, F^{seabed}_{il} in Eq. (3.62) needs to be integrated over the time interval $\Delta t\ (= t^{(n+1)} - t^{(n)})$ as follows,

$$\begin{aligned}\int_{t(n)}^{t(n+1)} F^{seabed}_{il}\,dt &\approx \frac{\Delta t}{2}\left(F^{seabed(n+1)}_{il} + F^{seabed(n)}_{il}\right)\\ &\approx \frac{\Delta t}{2}\left[K^{3}_{ijlk}\Delta U_{jk} + 2F^{seabed(n)}_{il}\right],\end{aligned} \tag{3.64}$$

where the trapezoidal rule is applied for numerical integration. Finally, by modifying Eq. (3.54), the equation of motion of a rod, taking into consideration of the seabed, becomes

$$\begin{aligned}&\left[\frac{4}{\Delta t^{2}}\hat{M}^{(n+\frac{1}{2})}_{ijlk} + K^{1}_{ijlk} + \lambda_{n}^{(n-\frac{1}{2})}K^{2}_{nijlk} - K^{3}_{ijlk}\right]\Delta U_{jk} + 2K^{2}_{nijlk}U^{(n)}_{jk}\Delta\lambda_{n}\\ &= \frac{4}{\Delta t}\hat{M}^{(n+\frac{1}{2})}_{ijlk}V^{(n)}_{jk} + \left(3F^{(n)}_{il} - F^{(n-1)}_{il} + 2F^{seabed(n)}_{il}\right) - 2\left(K^{1}_{ijlk} + \lambda_{n}^{(n-\frac{1}{2})}K^{2}_{nijlk}\right)U^{(n)}_{jk}.\end{aligned} \tag{3.65}$$

CHAPTER IV

POSITION KEEPING SYSTEM II: THRUSTER-ASSISTED POSITION MOORING

4.1. Introduction

Two position-keeping systems with thrusters are: dynamic positioning (DP) systems used for positioning freely floating offshore structures and thruster-assisted position mooring (POSMOOR) systems used for anchored floating structures.

As illustrated in Fig. 4.1, a DP system performs well both in deep and shallow water and the costs do not increase significantly as moorings. In this chapter, the general ideas are discussed by emphasizing key elements in a positioning system, which include wave filtering, controller design, and thrust allocation.

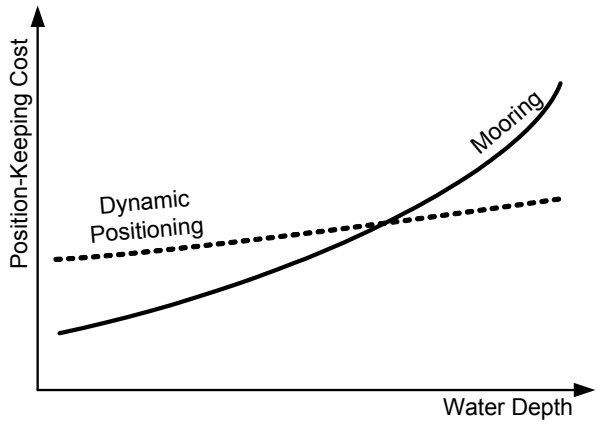

Fig. 4.1. Cost curves of position-keeping.

4.2. Reference Frames

Two different reference frames are used: an earth-fixed frame (X, Y, Z) and a body-fixed frame (x, y, z). As shown in Fig. 4.2, the turret center is set as the origin of the body-fixed frame, and ψ denotes the yaw angle of a platform with respect to the earth-fixed frame.

4.3. Continuous-Time Kalman Filter for Wave Filtering

The computation of optimal estimates of the states should be a key part of the design processes of an offshore floating structure control system. A Kalman filter is most commonly used for vessel positioning, tracking, detection, etc. In such complicated stochastic problems as measurement and noise reduction in offshore engineering in real-time application, its filtering algorithm and functionality are adequate to filter out wave

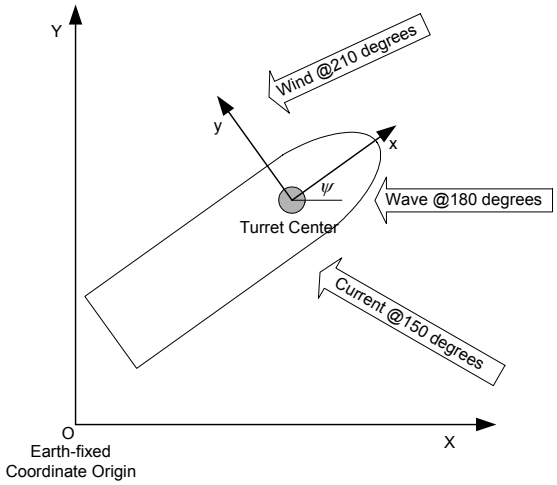

Fig. 4.2. Schematic diagram of coordinate convention and example of environmental forces.

frequency (WF) signal. Digital filters can also be used, but they may have a time shift problem depending on resolution, filter order, and cutoff frequency, when a real-time application is needed (Lee et al., 1999).

In this study a Kalman filter is used for optimal estimation of FPSO and spar responses and for the removal of the external forces which include both the leg (i.e., mooring line or riser) forces and the WF components of the environmental forces. A detailed study on a DP system based on Kalman filtering and optimal control was conducted and can be found in Balchen et al. (1980). The advantage of a self-tuning Kalman filter over extended Kalman filtering DP systems is also addressed in Fung and Grimble (1983).

For thruster-assisted moored platforms, zero vessel-velocity is assumed. To design an observer (state estimator), consider the low frequency (LF) ship model which is a linear, time-invariant system of the form (Lee et al., 1999 and Fossen, 1994),

$$\dot{\mathbf{x}} = \mathbf{A}\mathbf{x} + \mathbf{B}\mathbf{u} + \mathbf{E}\mathbf{w} \tag{4.1}$$

$$\mathbf{y} = \mathbf{C}\mathbf{x} + \mathbf{v}\,, \tag{4.2}$$

where dot (·) denotes time derivative, and each vector written in lower case can be described by the following set of definitions:

State $\mathbf{x} = [u, x, v, y, \omega, \psi]^T$

Control Input $\mathbf{u} = [\tau_x, \tau_y, \tau_\psi]^T$

Plant Noise $\mathbf{w} = [w_x, w_y, w_\psi]^T$

Measurement $\mathbf{y} = [x, y, \psi]^T$

Measurement Noise $\mathbf{v} = [v_x, v_y, v_\psi]^T$.

Each matrix written in upper case in Eqs. (4.1) and (4.2) can also be expressed as follows:

$$\mathbf{A} = \mathbf{M}^{-1}\begin{bmatrix} 0 & 0 & 0 & 0 & 0 & 0 \\ 1 & 0 & 0 & 0 & 0 & 0 \\ 0 & 0 & 0 & 0 & 0 & 0 \\ 0 & 0 & 1 & 0 & 0 & 0 \\ 0 & 0 & 0 & 0 & 0 & 0 \\ 0 & 0 & 0 & 0 & 1 & 0 \end{bmatrix}, \quad \mathbf{B} = \mathbf{E} = \mathbf{M}^{-1}\begin{bmatrix} 1 & 0 & 0 \\ 0 & 0 & 0 \\ 0 & 1 & 0 \\ 0 & 0 & 0 \\ 0 & 0 & 1 \\ 0 & 0 & 0 \end{bmatrix}$$

$$\mathbf{C} = \begin{bmatrix} 0 & 1 & 0 & 0 & 0 & 0 \\ 0 & 0 & 0 & 1 & 0 & 0 \\ 0 & 0 & 0 & 0 & 0 & 1 \end{bmatrix}$$

$$\mathbf{M} = \begin{bmatrix} M_{11} & 0 & 0 & 0 & 0 & 0 \\ 0 & 1 & 0 & 0 & 0 & 0 \\ 0 & 0 & M_{22} & 0 & M_{26} & 0 \\ 0 & 0 & 0 & 1 & 0 & 0 \\ 0 & 0 & M_{62} & 0 & M_{66} & 0 \\ 0 & 0 & 0 & 0 & 0 & 1 \end{bmatrix},$$

where $M_{11} = m + a_{11}(0)$

$$M_{22} = m + a_{22}(0)$$

$$M_{26} = m + a_{26}(0)$$

$$M_{62} = m + a_{62}(0)$$

$$M_{66} = I + a_{66}(0)$$

and m the mass of the floating structure, I the inertia moment in z-direction, and $a_{ij}(0)$ added masses in LF. Now, the LF estimated state vector $\hat{\mathbf{x}}$ can be written as

$$\hat{\mathbf{x}} = [\hat{u}, \hat{x}, \hat{v}, \hat{y}, \hat{\omega}, \hat{\psi}]^T . \tag{4.3}$$

In Eqs. (4.1) and (4.2), two noise vectors, $\mathbf{w}$ and $\mathbf{v}$, are assumed as vectors of mutually uncorrelated zero-mean Gaussian white noise signals describing the WF external disturbance forces, including the 1st-order wave exciting force, and WF responses,

respectively. Their covariance matrices are:

$$\mathbf{Q} = E\left[\mathbf{w}\cdot\mathbf{w}^T\right], \qquad \mathbf{R} = E\left[\mathbf{v}\cdot\mathbf{v}^T\right], \tag{4.4}$$

where E represents the time average. Finally, the estimator is therefore proposed in the structure

$$\dot{\hat{\mathbf{x}}}(t) = \mathbf{A}\hat{\mathbf{x}}(t) + \mathbf{B}\mathbf{u}(t) + \mathbf{L}(t)\left[\mathbf{y}(t) - \mathbf{C}\hat{\mathbf{x}}(t)\right], \tag{4.5}$$

where $\mathbf{L}(t)$ is the continuous-time Kalman gain, and it is given by

$$\mathbf{L}(t) = \mathbf{P}\mathbf{C}^T\mathbf{R}^{-1}, \tag{4.6}$$

where $\mathbf{P}$ is the solution of the following differential matrix *Riccati equation*, independent of the gain $\mathbf{L}$:

$$\mathbf{0} = \dot{\mathbf{P}} = \mathbf{A}\mathbf{P} + \mathbf{P}\mathbf{A}^T - \mathbf{P}\mathbf{C}^T\mathbf{R}^{-1}\mathbf{C}\mathbf{P} + \mathbf{G}\mathbf{Q}\mathbf{G}^T. \tag{4.7}$$

4.4. PID Control and LQR

Considering excessive thruster modulation gives us the common fact that it is not desirable to counteract the WF motion caused by 1st-order wave exciting forces. Only slowly varying signals which originate mainly from the 2nd-order mean and slowly varying environmental forces need to be obtained through a filter; those filtered signals are used for a control algorithm. In this study, a PID (Proportional-Integral-Derivative) controller is adopted, and the integral gains I_x, I_y, and I_ψ are set to zero by assuming that the error integral is not significant. However, in general, steady-state errors due to wind, current, and wave drift can all be compensated for by adding integral action to the control law.

The required control input vector $\mathbf{u}$ (thruster force) is calculated based on the

following P(I)D control theory,

$$\mathbf{u} = -\mathbf{K}\mathbf{e}\,, \tag{4.8}$$

where the PD gain matrix $\mathbf{K}$ is

$$\mathbf{K} = \begin{bmatrix} D_x & P_x & 0 & 0 & 0 & 0 \\ 0 & 0 & D_y & P_y & 0 & 0 \\ 0 & 0 & 0 & 0 & D_\psi & P_\psi \end{bmatrix} \tag{4.9}$$

and the deviation vector $\mathbf{e}$ of the floating structure from its target location is

$$\mathbf{e} = \hat{\mathbf{x}} - \mathbf{x}_{set}\,. \tag{4.10}$$

In Eq. (4.9), D and P denote derivative and proportional gains, respectively. The main objective is to make the deviation vector $\mathbf{e}$ zero in Eq. (4.8). There could be many methods to convert the deviation to the required thrust $\mathbf{u}$. In this research, Linear Quadratic Regulator (LQR) methodology is used to specify the gain matrix $\mathbf{K}$.

Cost may be a function of the input $\mathbf{u}$, the time, and the state vector. The goal of an optimal controller is, therefore, to determine the input $\mathbf{u}$. Let the cost function as

$$J = \int_0^\infty \left\{ \mathbf{e}(t)^T \mathbf{Q}_o \mathbf{e}(t) + \mathbf{u}(t)^T \mathbf{R}_o \mathbf{u}(t) \right\} dt\,, \tag{4.11}$$

and through minimization of the *cost function* J (or performance function) the gain $\mathbf{K}$ needs to be sought. In other words, minimization of J means trying to make the deviation $\mathbf{e}$ zero with as little control input $\mathbf{u}$ (thruster force) and state deviation $\mathbf{e}$ (position error) as possible with the balancing thruster energy and deviations by changing the $\mathbf{Q}_o$ (state cost) and $\mathbf{R}_o$ (input cost), which are weighting factor matrices.

In the process of optimally designing the thruster control system, the tuning or balancing of two weighting factors is critical, and this requires a designer to decide which factor to emphasize: station-keeping accuracy or costs for thruster energy. Thus, the values

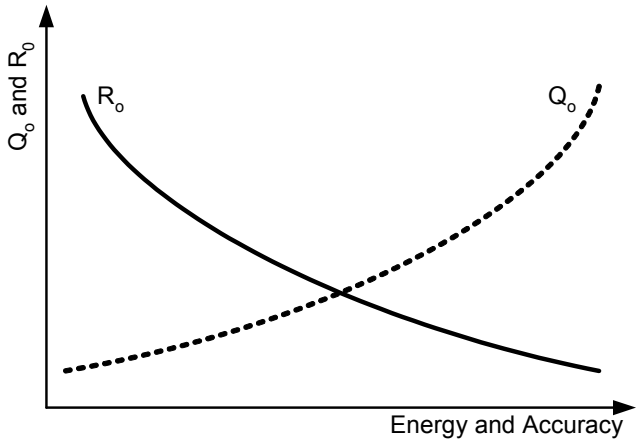

Fig. 4.3. Relationship between energy/accuracy and weighting factors $\mathbf{Q}_o$ and $\mathbf{R}_o$.

for $\mathbf{Q}_o$ and $\mathbf{R}_o$ are considered as design parameters. Following are three cases that enable one to better understand how the two values work in the tuning procedure:

(1) When $Q_{ij} = 0$, station-keeping error is not concerned at all

(2) Relatively high values of Q_{ij} compared to R_{ij} mean that a large amount of control energy is required to achieve a small watch-circle of a floating structure

(3) When $R_{ij} = 0$, infinite control energy (impractical case) is allowed to achieve the station-keeping error to be zero.

Better accuracy may require more energy. Therefore, the accuracy limitation is bounded by the given control energy limitation. The concept of tuning $\mathbf{Q}_o$ and $\mathbf{R}_o$ is illustrated in Fig. 4.3. Finding the state-feedback gain matrix $\mathbf{K}$ to minimize the cost function J results in solving the following *Ricatti equation* for $\mathbf{P}$:

$$\mathbf{A}^T\mathbf{P} + \mathbf{P}\mathbf{A} - \mathbf{P}\mathbf{B}\mathbf{R}_o^{-1}\mathbf{B}^T\mathbf{P} + \mathbf{Q}_o = 0, \tag{4.12}$$

where the state matrix $\mathbf{A}$ and the input matrix $\mathbf{B}$ are the same matrices mentioned in Eq.

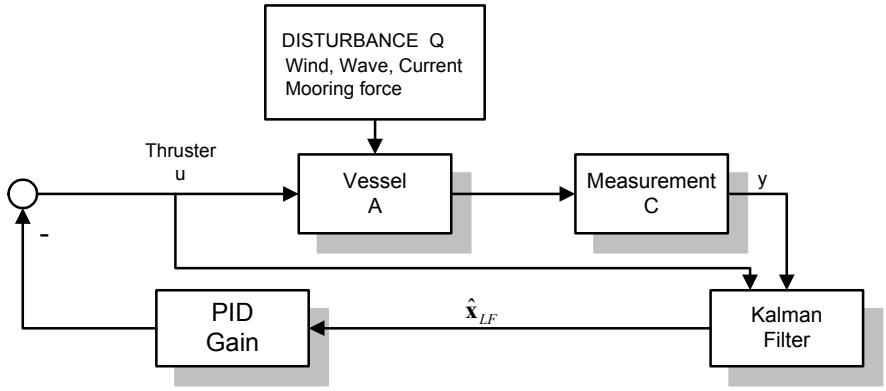

Fig. 4.4. Block diagram of control strategy of floating structure.

(4.1). Finally, the optimal $\mathbf{K}$ is derived from $\mathbf{P}$ by

$$\mathbf{K} = \mathbf{R}_o^{-1}\mathbf{B}^T\mathbf{P} . \tag{4.13}$$

An overall concept of this floating structure control system can be summarized in Fig. 4.4 (Aalbers et al., 1995).

4.5. Thrust Allocation Algorithm

A thrust allocation algorithm, which is basically distribution of the thrust to each installed thruster depending on the type (i.e., azimuth, channel, fixed, etc.), power limit, thruster characteristics, and the locations of the thrusters, is followed by the calculation of the required thrust $\mathbf{u}$ in Eq. (4.8). In practical applications, fuel consumption, wear and tear of the thrusters, the saturation of the rpm/pitch inputs, forbidden directional sectors, and power limitation of the thrusters need to be considered (Sorensen, 2003).

As shown in Fig. 4.5, three-thruster configuration was selected for study case I: a

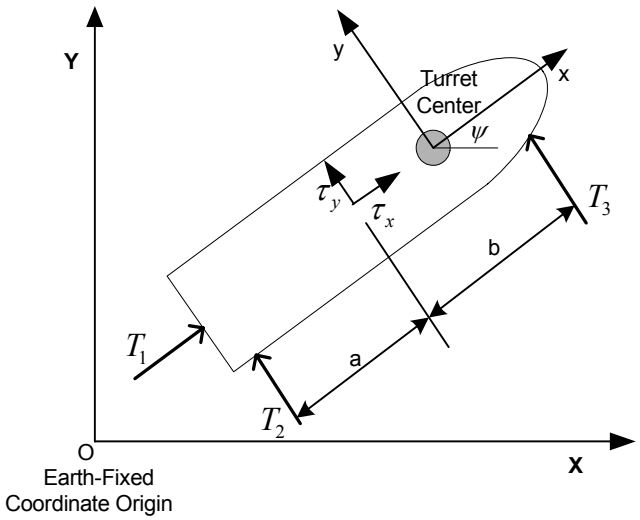

Fig. 4.5. An example of thrust allocation.

main propeller and two side thrusters at bow and stern, respectively. To calculate each thruster force, the following equation is constructed:

$$\mathbf{T} = \begin{bmatrix} 1 & 0 & 0 \\ 0 & 1 & 1 \\ 0 & -a & b \end{bmatrix}^{-1} \mathbf{u}_o , \tag{4.14}$$

where thruster force $\mathbf{T} = [T_1, T_2, T_3]^T$, and the control input vector $\mathbf{u}_o = [\tau_x, \tau_y, \tau_\psi]^T$ with respect to the body-fixed frame (x, y, z) is given by the following formula:

$$\mathbf{u}_o = \begin{bmatrix} \cos\psi & \sin\psi & 0 \\ -\sin\psi & \cos\psi & 0 \\ 0 & 0 & 1 \end{bmatrix} \mathbf{u} . \tag{4.15}$$

CHAPTER V

COUPLED DYNAMIC ANALYSIS OF THRUSTER-ASSISTED MOORED STRUCTURES

5.1. Introduction

In previous Chapters II through IV, floating structure dynamics, mooring line dynamics, and thruster-assisted system were discussed. To address the coupled dynamic analysis of thrust-assisted moored floating platforms, those described ideas are to be linked together. However, *quasi-static* analyses have been used for floating platform design since the water depth was not significantly deep. As mentioned in Chapter I, motions of floating structures would be more influenced by moorings and risers in deep waters.

In this chapter, the difference between coupled and uncoupled analyses is reviewed. One of the objectives of this research is to suggest a new approach: a coupled dynamic analysis of thruster-assisted moored offshore platforms. In the next two chapters, two study cases are investigated in order to test two established hypotheses mentioned previously through relevant numerical simulations of floating platforms in hypothetically deep water on the basis of an assumption that a common thruster specification is not given.

5.2. Coupled Analysis

Traditionally, a *quasi-static* approach is used for the prediction of the motions of

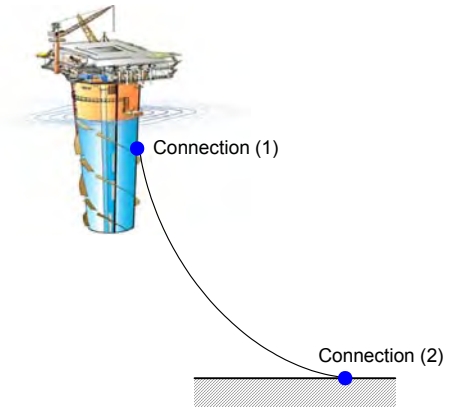

Fig. 5.1. Illustration of two important connections for coupling analysis.

floating structures. An uncoupled analysis consists of two steps. First, motion response of a platform is calculated by uncoupling it from the mooring and riser systems. Secondly, the calculated floating structure motions are then fed as prescribed boundary conditions for the mooring line/riser analysis.

As water depth increases, the mass of the mooring lines and risers, called "legs," becomes larger, and the effect of the dynamic interaction between the floating structure and the legs should be considered for a better analysis (Kim and Kim, 2002). Also, the quasi-static approach can not capture the interaction between the structure and the legs (mooring lines and risers). Luo and Baudic (2003) addressed that the time domain coupled analysis is the most adequate for the hull-leg interaction because mooring lines and risers can significantly influence hull responses.

As shown in Fig. 5.1, the hull-leg coupling essentially requires two appropriate connections: (1) connection of the hull and the leg, and (2) connection of the seabed and the leg. Then, the interactions between the hull and the leg are properly considered based on the hydrodynamic modeling of each object. The modeling of the coupling between

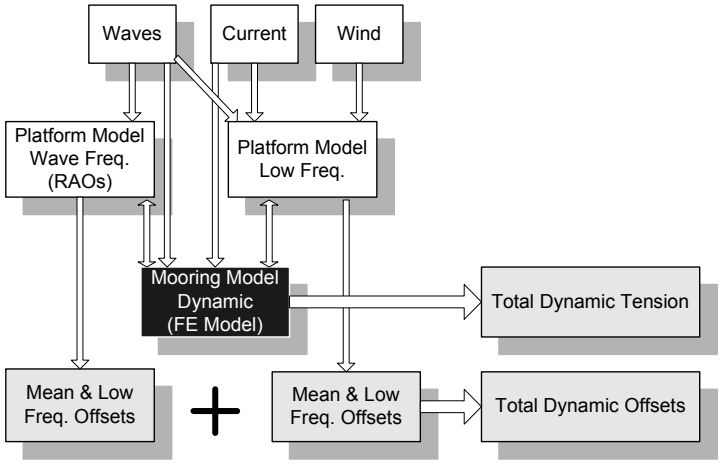

Fig. 5.2. Coupled analysis flowchart. Gray – output data; white – input data; black – mooring model (Luo and Baudic, 2003).

mooring lines and a platform, the numerical method to integrate the motion equations of line and the platform in static, time-domain, and frequency-domain analyses, the modeling of the line-seabed connection, the assembled algebraic equations of a coupled system are described in Ran (2000) in detail. Flowcharts of a coupled analysis and an uncoupled analysis are shown in Figs. 5.2 and 5.3 (Luo and Baudic, 2003).

5.3. Inclusion of Thruster Force

Reduction of the global motion responses of offshore platforms in harsh environment in deep water is one of the most important concerns for the analysis and/or design of the platforms. By applying a DP or thruster-assist system, total dynamic responses and motion performance of the platforms can be improved in terms of mooring line stresses and the operation radius of a platform. The assistance of thrusters is only complementary to the

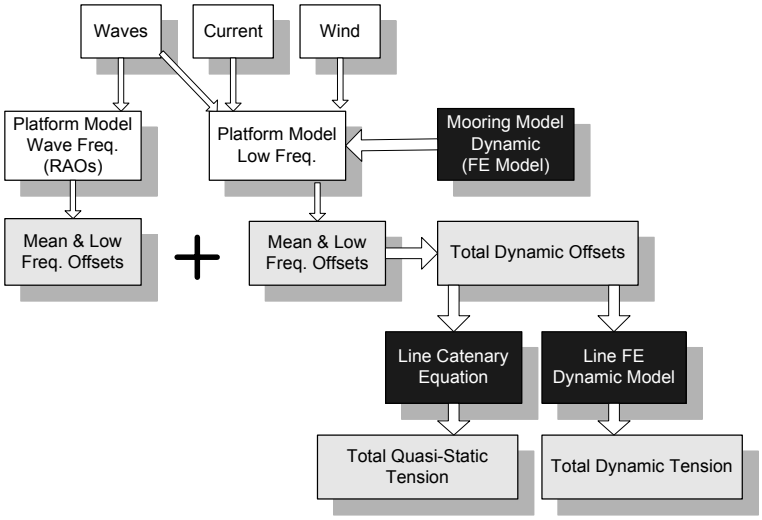

Fig. 5.3. Uncoupled analysis flowchart. Gray – output data; white – input data; black – mooring model (Luo and Baudic, 2003).

mooring system (Strand et al., 1998) since the mooring force, in general, is much larger than the thruster force.

To analyze a thruster-assisted POSMOOR system, the appropriate thruster force needs to be calculated by the methodology mentioned in Chapter IV, and it is added to the total external force term in the Newton's 2nd law, which is the following equation of motion in the horizontal plane (i.e. surge, sway, and yaw),

$$m\ddot{\mathbf{X}} = \mathbf{F}_E + \mathbf{F}_H + \mathbf{F}_M + \mathbf{F}_T \tag{5.1}$$

where m represents platform mass plus the added mass, $\mathbf{X}$ displacement vector in X-, Y-, Z-directions, double dot 2nd time derivative, $\mathbf{F}_E$ environmental force and moment, $\mathbf{F}_H$ hydrodynamic reaction force, $\mathbf{F}_M$ mooring force, and $\mathbf{F}_T$ thruster force and moment acting on the platform. The proper method to calculate each force is discussed in Chapters II through IV.

Not to have thruster wear and tear, it is not desirable to counteract the WF motion. Only slowly varying motions are filtered for the platform control. For this purpose, a Kalman filter was addressed in Chapter IV.

It is intuitively correct that the time domain coupled analysis is physically reasonable for numerical simulations of thruster-assisted moored platforms since the required thrust should be calculated in every time step based on total external forces. Thus, theoretically, an uncoupled analysis with two-step procedure cannot correctly implement the time-varying thruster force $\mathbf{F}_T$ that needs to be obtained from the relationship between the platform excursion and the instant total external force.

As shown in Fig. 5.3, in quasi-static analysis $\mathbf{F}_T$ is calculated and applied to the first step that is for the platform response only. Then, as the second step a mooring line analysis program uses the results of the body motions. Therefore, the interaction between the thruster force and mooring lines cannot be taken into account.

CHAPTER VI

CASE STUDY I: THRUSTER-ASSISTED TURRET-MOORED FPSO

6.1. Introduction

As shown in Fig. 6.1, an FPSO is the most dominant offshore floating structure in terms of the total number of installed or sanctioned platforms. In this chapter, a turret-moored FPSO is selected to investigate and/or to analyze how much a thruster-assisted POSMOOR system affects the responses of an FPSO compared to a conventionally turret-moored FPSO, and what advantage may be achieved in the mooring/riser top tension by means of spectral and statistical analyses. The tanker-based FPSO moored by 12 chain-polyester-chain taut mooring lines with 13 steel catenary risers designed for 1,829m (=6,000ft) water depth is numerically simulated to investigate the characteristics of

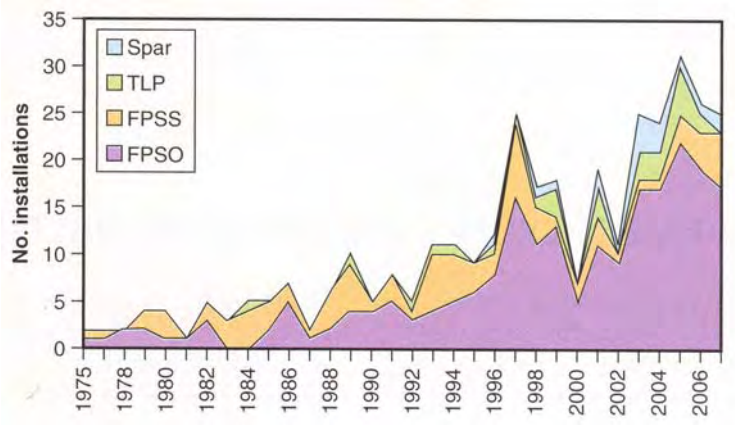

Fig. 6.1. Trend of different types of offshore platforms. (Source: *The World Floating Production Report 2003-2007*, Douglas-Westwood & Infield Systems)

nonlinear behaviors and hull/mooring/riser dynamic coupling (Kim and Kim, 2002), and the same FPSO is employed for this case study. This FPSO has also been used for the DeepStar Project, which is a joint industry technology development project focused on advancing the technologies in water depths to 10,000ft. DeepStar Project seeks cost-effective, low risk methods in deep water development.

The 1st-order wave-frequency and 2nd-order difference-frequency wave loads, fluid added mass, and radiation damping for the hull are calculated in the frequency domain from the 2nd-order diffraction/radiation program WAMIT. The wave-current induced forces on slender members are calculated from the Morison's equation.

The 100-yr hurricane with non-parallel wind, wave, and current is used as the environmental condition. The wind and current forces were calculated from the empirical data provided by OCIMF (Oil Company International Marine Forum, 1994). In this case study, the environmental condition is a design condition for the GoM not an operational condition, which is milder than the design condition.

6.2. Description of Thruster-Assisted Turret-Moored FPSO

6.2.1. FPSO Particulars

The prototype FPSO used in this study is a 200,000 DWT tanker moored in 1,829m water depth. The internal turret is located 63.55m away from the forward perpendicular, and its diameter is 15.8m. The particulars of the FPSO are given in Table 6.1.

Table 6.1

Turret-Moored FPSO Particulars

Designation	Symbol	Unit	Quantity
Production level		bpd	120000
Storage		bbls	1440000
Vessel size		kDWT	200
Length b/w perpendiculars	Lpp	*m*	310
Breadth	B	*m*	47.2
Depth	H	*m*	28.0
Draft	T	*m*	18.9
Length to beam ratio	L/B		6.57
Beam to draft ratio	B/T		2.5
Displacement	∆	ton	240869
Block coefficient	Cb		0.85
Center of buoyancy forward section 10	FB	*m*	6.6
Water plane area	A	m^2	13400
Water plane coefficient	Cw		0.9164
Center of water plane area forward section 10	FA	*m*	1.0
Center of gravity above base	KG	*m*	13.3
Metercentric height transverse	MGt	*m*	5.8
Metercentric height longitudinal	MGl	*m*	403.8
Trans. radius of gyration in air	Kxx	*m*	14.8
Long. radius of gyration in air	Kyy	*m*	77.5
Yaw radius of gyration	Kzz	*m*	79.3
Wind area front	Af	m^2	1012
Wind area side	Ab	m^2	3772
Turret in centerline behind Fpp (20.5% Lpp)		*m*	63.5
Turret elev. below tanker base		*m*	1.5
Turret diameter		*m*	15.8

6.2.2. Mooring Line and Riser Particulars

The particulars of the mooring lines and risers are given in Tables 6.2 and 6.3. The FPSO has 12 chain-polyester-chain mooring lines and 13 steel catenary risers. Polyester mooring lines, in this study, are assumed to be elastic in this study with a representative Young's modulus. As shown in Fig. 6.2, the 12 mooring lines are arranged in four groups, and each line is numbered. Each group is 90 degrees apart and consists of three legs 5 degrees apart. The seabed is modeled as an elastic bed with a quadratic spring as mentioned in chapter 3.

The particulars of the hull, mooring lines, and risers are almost identical to those of the standard model set up by DeepStar Offshore Industry Consortium (Wichers and Devlin, 2001) except for two cases. The first one is the angle of mooring lines at the fairlead; here 43 degrees were used instead of 48.8 degrees. The second difference is the angle of top riser connection; 77 degrees were used here instead of 80.9 degrees (Kim and Kim, 2002). The general arrangement and numbering of the FPSO risers is shown in Fig. 6.3.

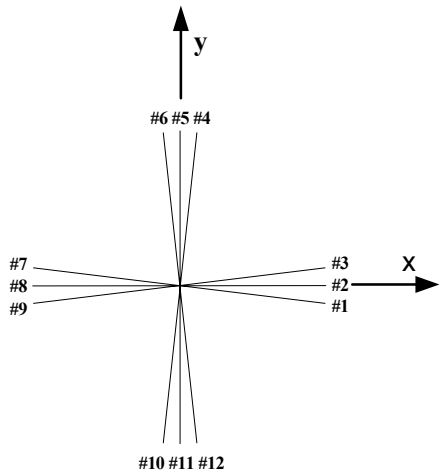

Fig. 6.2. Arrangement and numbering of the FPSO mooring lines.

Table 6.2

Mooring Line Particulars

Designation	Unit	Quantity
Water depth	*m*	1829
Pre-tension	*kN*	1424
Number of lines		4×3
Degree between the 3 lines	*deg.*	5
Length of mooring line	*m*	2652
Radius of location of chain stoppers on turn table	*m*	7.0
Segment 1: Chain		
Length at anchor point	*m*	121.9
Diameter	*cm*	9.52
Dry weight	*N/m*	1856
Weight in water	*N/m*	1615
Stiffness AE	*kN*	912120
Mean breaking load (MBL)	*kN*	7553
Segment 2: Polyester		
Length	*m*	2438
Diameter	*cm*	16.0
Dry weight	*N/m*	168.7
Weight in water	*N/m*	44.1
Stiffness AE	*kN*	186800
Mean breaking load (MBL)	*kN*	7429
Segment 3: Chain		
Length at anchor point	*m*	91.4
Diameter	*cm*	9.53
Dry weight	*N/m*	1856
Weight in water	*N/m*	1615
Stiffness AE	*kN*	912120
Mean breaking load (MBL)	*kN*	7553

Table 6.3

Riser Particulars

Riser Type	Top Tension	OD	AE	EI	Weight Dry/Wet	Cdn
	kN	*cm*	*kN*	*kNm²*	*N/m*	
Liquid Production (LP)	2224	44.5	1.83×107	276	1927 1036	1
Gas Production (GP)	1223	38.6	1.08×107	113	1708 525	1
Water Injection (WI)	4048	53.1	1.86×107	224	2802 1897	1.414
Gas Injection (GI)	2714	28.7	3.14×106	64	1810 1168	1.414
Gas Export (GE)	912	34.3	8.63×106	71	1357 423	1
Total Length of Risers		3657.4 m				

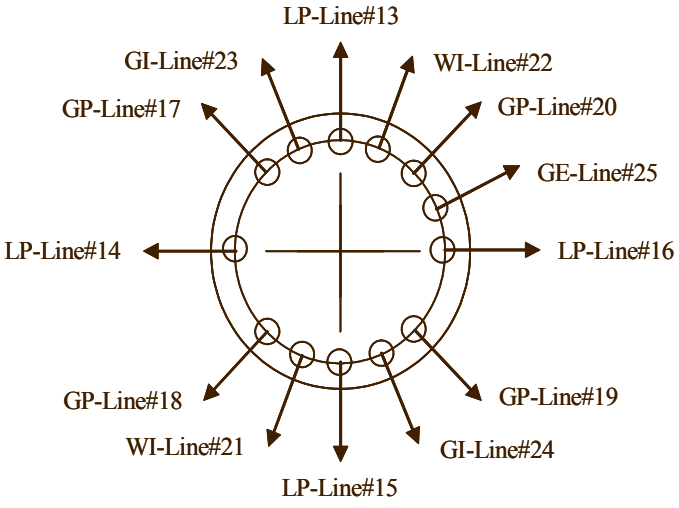

Fig. 6.3. Arrangement and numbering of the FPSO risers.

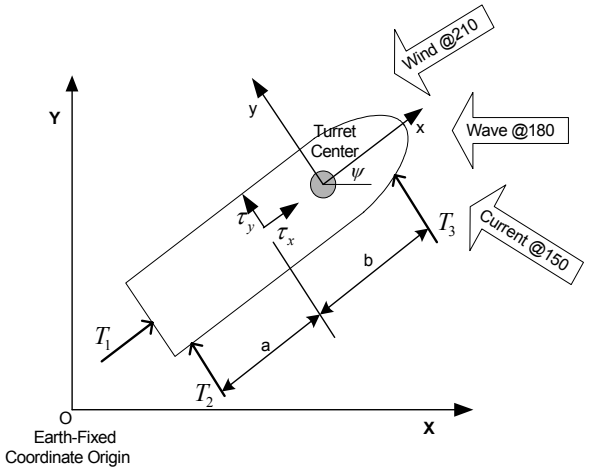

Fig. 6.4. Coordinate convention and direction of environmental forces.

6.2.3. Thruster Implementation

In this case study, two thruster depths are considered: (1) the still water level and (2) 16*m* below the still water level. Even though case (1) is not practical, the comparison between the two cases may be helpful to understand the effect of the thruster depth and what relevant motions occur when the thruster depth varies. Especially, the roll and pitch motions are supposed to be affected by the thruster depth. The maximum thrust limit in both x- and y-directions is predefined as 8×10^6 N. The arrangement of three thrusters is shown in Fig. 6.4.

6.3. Design Environmental Condition

The directions of three different environmental forces are shown in Fig. 6.4. The OCIMF data were used for the wind and current force coefficients, and a cylindrical bow

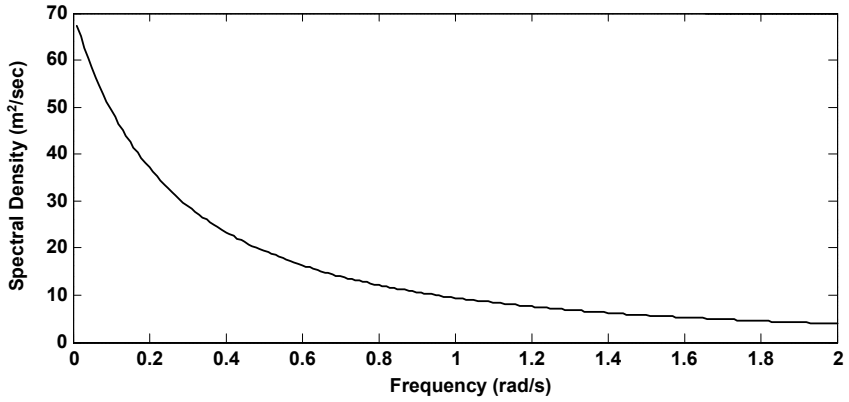

Fig. 6.5. API wind speed spectrum for 100-yr GoM hurricane condition.

with full loading condition was selected. The storm induced current flows from 30 degrees right of wave direction and is assumed to be steady. The current velocity is assumed to be 1.07m/s between 0–61m and reduced to 9.1cm/s at 91–910m. The drag coefficients for wave forces are 1.0 for mooring lines and 1.0 or 1.414 for risers.

The API (America Petroleum Institute) wind spectrum was used to prepare the dynamic wind forces. The wind speed at 10m above the still water level and the wind direction are required to get those wind forces. The applied wind speed is 148km/h at 10m, and its direction is 30 degrees left of waves. The corresponding wind spectrum is shown in Fig. 6.5.

Mathematical description of the API wind spectrum is given in Eqs. (6.1) through (6.3) (API RP-2A WSD, 1994).

$$S(\omega) = \frac{\sigma^2(z)}{2\pi f_p \left[1 + \frac{1.5}{2\pi f_p}\right]^{\frac{5}{3}}} \tag{6.1}$$

where the average factor f_p derived from measured spectra and the standard deviation of

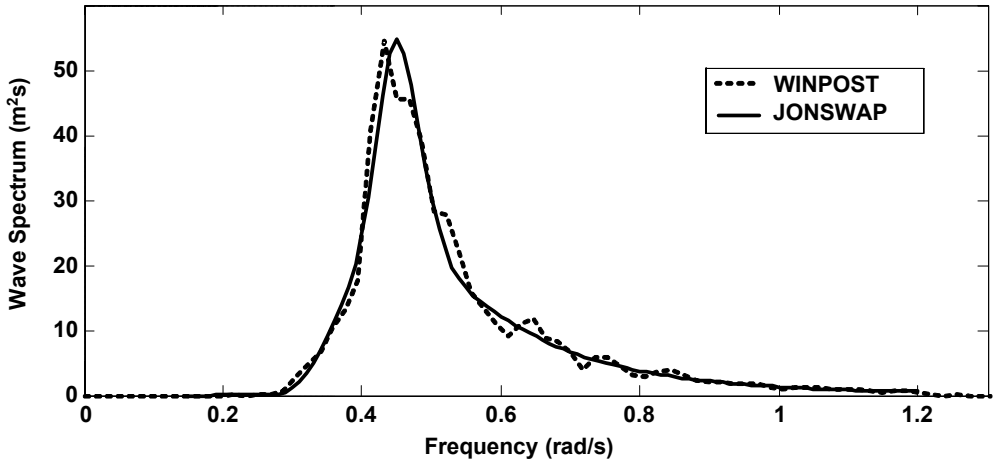

Fig. 6.6. Wave spectra from WINPOST simulation (dotted line) and JONSWAP (solid line) for 100-yr GoM hurricane condition.

wind speed $\sigma(z)$ at 10m above the mean water level are respectively expressed as

$$f_p = \frac{0.025 V_w(z)}{z}, \tag{6.2}$$

$$\sigma(z) = 0.15\left(\frac{z}{20}\right)^{-0.125} V_w(z) \tag{6.3}$$

where $V_w(z)$ is the one hour mean wind speed (m/s) at z m above the mean water level.

Unidirectional wave condition is applied. A JONSWAP (Joint North Sea Wave Project) spectrum with significant wave height H_s=12.19m, peak period T_p=14s, and overshoot parameter γ=2.5 was selected to represent a typical 100-yr hurricane in the GoM (Fig. 6.6). While a 10-yr storm condition is suggested for a full DP system, the 100-yr hurricane condition is applied in this study. As Aalbers et al. (1995) mentioned, the design sea conditions for a thruster-assisted POSMOOR system can be stronger than those considered for a full DP system.

6.4. Preparation of Hydrodynamic Coefficients and Wave Forces

The 2nd-order diffraction/radiation program called WAMIT is used for the calculations of the added mass and radiation damping, the 1st-order wave-frequency forces, and 2nd-order mean and difference-frequency forces (Korsmeyer et al., 1988 and Lee et al., 1991). Fig. 6.7 shows the panel distributions on the body surface. Only half hull was discretized for saving numerical calculation time based on the symmetrical hull shape of the FPSO. There are total 1,684 panels for hull, and 480 panels for the free surface. The wave exciting forces obtained in frequency domain were converted to the ones in time domain by applying two-term Volterra series expansion (Ran et al., 1995). The radiation damping was included while the wave drift damping was not considered.

The analysis methodology employed in this study is similar to those of Ran and Kim (1997) and Kim et al. (1999). It is assumed that the mooring lines are hinged at both the turret and anchor position. The near-vertical risers are also hinged at the turret. The calculated FPSO mass at 18.9m draft condition is 2.3686×10^8 kg. The viscous

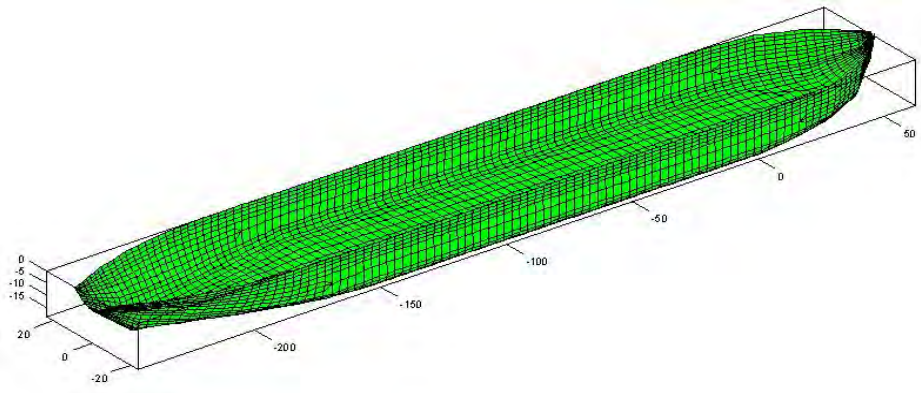

Fig. 6.7. Mesh generation of the turret-moored FPSO. The body-fixed frame is located at the turret center on the mean water level.

damping coefficients of the same FPSO in normal direction were adopted from the model test results (Wichers and Ji, 2000).

The wave force QTFs are computed for 9 wave frequencies, ranging from 0.24 to 1.8 rad/sec, and the intermediate wave forces for other frequencies are calculated by an interpolation method. For various yaw angles with 5-degree interval, the hydrodynamic coefficients and wave forces were prepared for the WINPOST input.

6.5. Time-Domain Simulation

The four-step interpretation used for a coupled dynamic analysis of this case study follows this rationale: When (1) *environmental forces originated by waves, current, and wind* act on a floating platform, (2) *thrusters* are supposed to counteract those environmental forces. Then, due to the time-varying unbalance of the entire external forces including the mooring/riser reaction forces (3) *floating structure motions* occur. Ultimately, the interactions of the environmental forces, the thruster forces, and the motions of the platform create such structural behavior as (4) *tension changes in the mooring lines and risers*. In this section, those four aspects are systematically discussed according to priority.

6.5.1. Review of Environmental Forces

First, the time traces of the four decomposed environmental forces in X- and Y-directions are shown in Figs. 6.8 and 6.9. Their power spectra are shown in Figs. 6.10 and 6.11. The wave exciting and radiation damping forces are oscillatory forces with higher

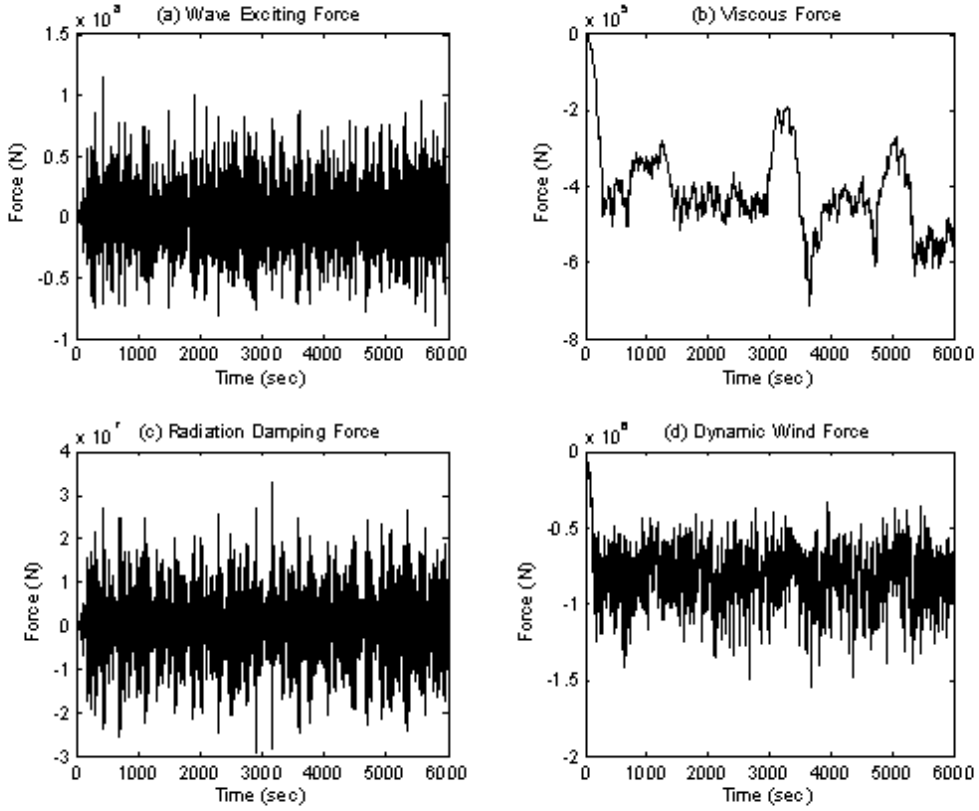

Fig. 6.8. Decomposed external forces in X-direction for 100-yr hurricane case: (a) wave exciting, (b) viscous, (c) radiation damping, and (d) wind forces.

order of peak force compared to other two forces. According to the spectra shown in Figs. 6.10 and 6.11 and the statistical results summarized in Table 6.4, slowly-varying forces, i.e. viscous and wind forces, have similar order of force in terms of mean value.

On the other hand, as clearly shown in Figs. 6.8 and 6.9, the wave exciting and radiation forces have larger dynamic forces compared to those slowly-varying forces, and their spectrum components are bounded in WF region, which needs to be ignored in DP or thruster-assisted moored platforms.

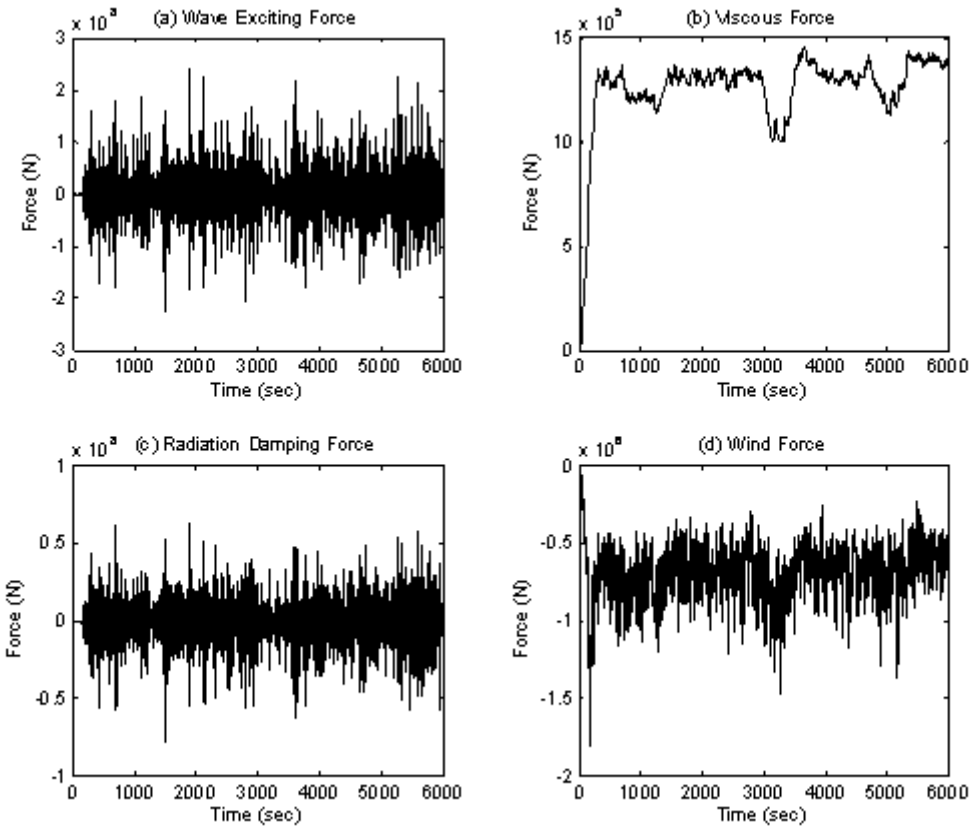

Fig. 6.9. Decomposed external forces in Y-direction for 100-yr hurricane case: (a) wave exciting, (b) viscous, (c) radiation damping, and (d) wind forces.

The statistics of these environmental forces are the most important design factors in company with static offset curves. For instance, it is useful to compare the quantities of each force summarized in Table 6.4. For example, the sum of the mean values in X-direction is -2,805 kN, and the sum of the mean values in Y-direction has +1,852 kN. As counteract forces, the mooring line restoring force and the thrust are supposed to react against those environmental forces.

Based on the mean values of the environmental forces, ultimately, the mean location

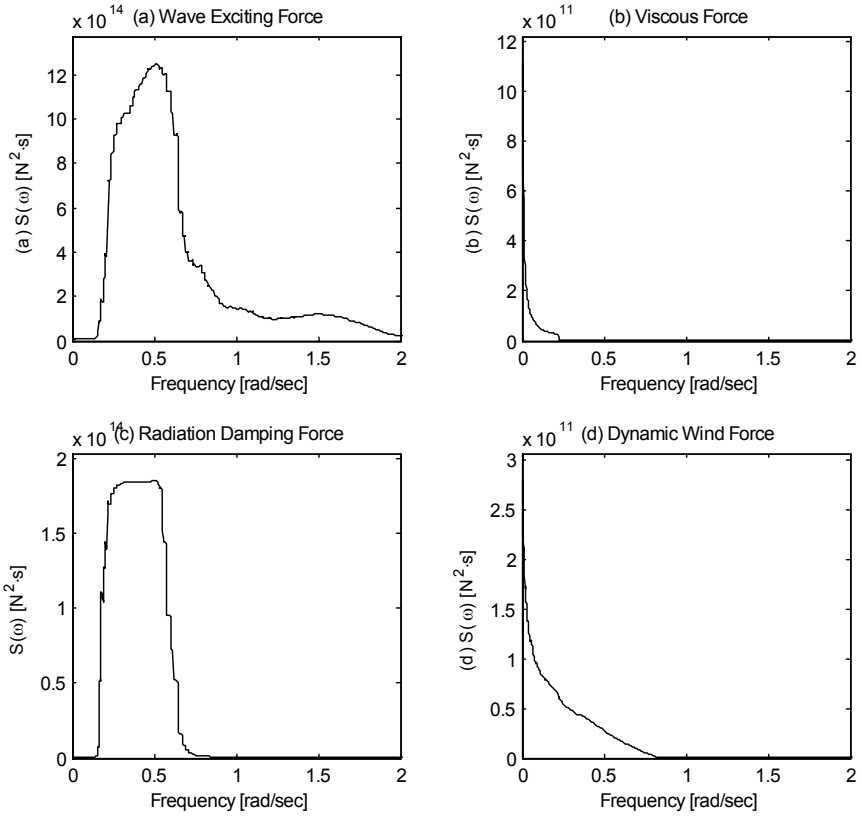

Fig. 6.10. Power spectra of the decomposed external forces in X-direction: (a) wave exciting, (b) viscous, (c) radiation damping, and (d) wind forces.

of the FPSO will move to a certain point in the 2nd quadrant. In addition, the order of mean forces gives us an idea about how much thrust must be created to react on the environmental forces.

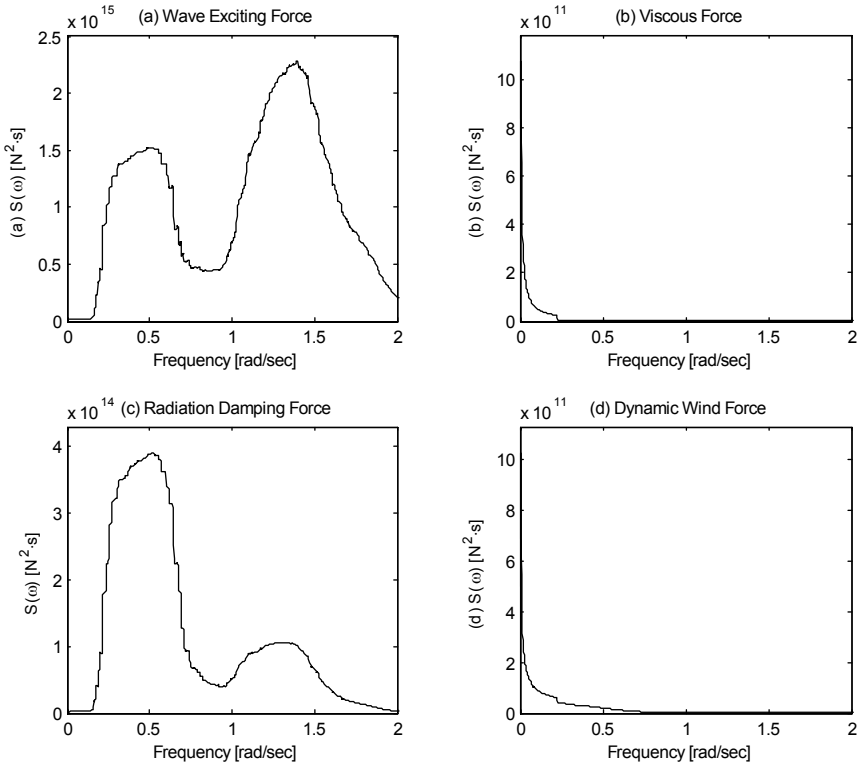

Fig. 6.11. Power spectra of the decomposed external forces in Y-direction: (a) wave exciting, (b) viscous, (c) radiation damping, and (d) wind forces.

Table 6.4

Statistical Results of External Forces Acting on Thruster-Assisted FPSO in 100-Yr GoM Hurricane (unit: kN)

	X			**Y**		
Force	Mean	*STD*	Extreme	Mean	*STD*	Extreme
Wave Exciting	-1552	26310	95290	1241	46580	225100
Viscous	-439	108	-712	1298	105	1463
Radiation Damping	8	9023	33400	9	15430	-63010
Dynamic Wind	-822	186	-1547	-687	174	-1475

6.5.2. Evaluation of Commanded Thrust

As the slowly-varying active opposing forces against the environmental forces, the thruster forces in X- and Y-directions are calculated based on the designed control algorithm which includes a Kalman filter, LQR, and PID controller. Based on tuning, the covariance matrices $\mathbf{Q}$ and $\mathbf{R}$ in Eq. (4.4) and the weighting factor matrices $\mathbf{Q}_o$ and $\mathbf{R}_o$ in LQR Eq. (4.11) are given by

$$\mathbf{Q} = \begin{bmatrix} (2.9\times10^{6})^2 & 0 & 0 \\ 0 & (5\times10^{5})^2 & 0 \\ 0 & 0 & (3\times10^{7})^2 \end{bmatrix} \tag{6.4}$$

$$\mathbf{R} = \begin{bmatrix} (5.3\times10^{-1})^2 & 0 & 0 \\ 0 & (4.3\times10^{-1})^2 & 0 \\ 0 & 0 & (4.6\times10^{-3})^2 \end{bmatrix} \tag{6.5}$$

$$\mathbf{Q}_o = \begin{bmatrix} (10^{5})^2 & 0 & 0 \\ 0 & (10^{5})^2 & 0 \\ 0 & 0 & 1^2 \end{bmatrix} \tag{6.6}$$

$$\mathbf{R}_o = \begin{bmatrix} 1^2 & 0 & 0 \\ 0 & 1^2 & 0 \\ 0 & 0 & 1^2 \end{bmatrix}. \tag{6.7}$$

Based on the above values, the PD gains in Eq. (4.9) are given in Table 6.5.

Table 6.5

PID Gains Used for Thruster-Assisted Turret-Moored FPSO

P_x [kN/m]	D_x [kNs/m]	P_y [kN/m]	D_y [kNs/m]	P_ψ [kN/rad]	D_ψ [kNs/rad]
100	7090	100	6450	0	0

For the arrangement of the thrusters, and as an example of thrust allocation, it is assumed that the bow and stern side tunnel thrusters are located at 120m from the FPSO center of gravity (See Fig. 6.4.). It is also assumed that all the thruster forces act on the mean water level for this case. The maximum thrust limit in x- and y-directions is predefined as 4.5×10^{6} N.

The PD control, cost function optimization in LQR, and Kalman filtering described in Chapter IV were applied to this case study, and the required thrust in surge and sway directions were calculated and plotted in Figs. 6.12 and 6.13. Time traces of the commanded thruster forces in surge and sway directions and their power spectra are also shown. Most of the commanded power is concentrated in LW range, both in surge and sway directions. The statistical results of the thrusts are summarized in Table 6.6. The thruster system is designed to counter the mean and LF motions caused by wave, wind, and current drift forces. The motions in the WF region are essentially cyclic, so the structure would have repetitive motions following closed loops.

If a thruster system is designed to counter this cyclic behavior, thrusters would have strong tear and wear with unwanted fuel consumption. Therefore, thruster power spectra can be used to verify whether the required thrusters have WF components or not.

It is also valuable to compare Tables 6.4 and 6.6 to examine how much the thruster system would contribute to the position-keeping operation of the spar. For instance, the amount of the thruster force in surge is 30% of the total sum of the mean environmental force in surge; the thruster force in sway is 30% of the total sum of the mean environmental force in sway. In addition, the wave exciting and radiation forces have large *STD* values compared to the viscous and wind forces. On the other hand, the thruster

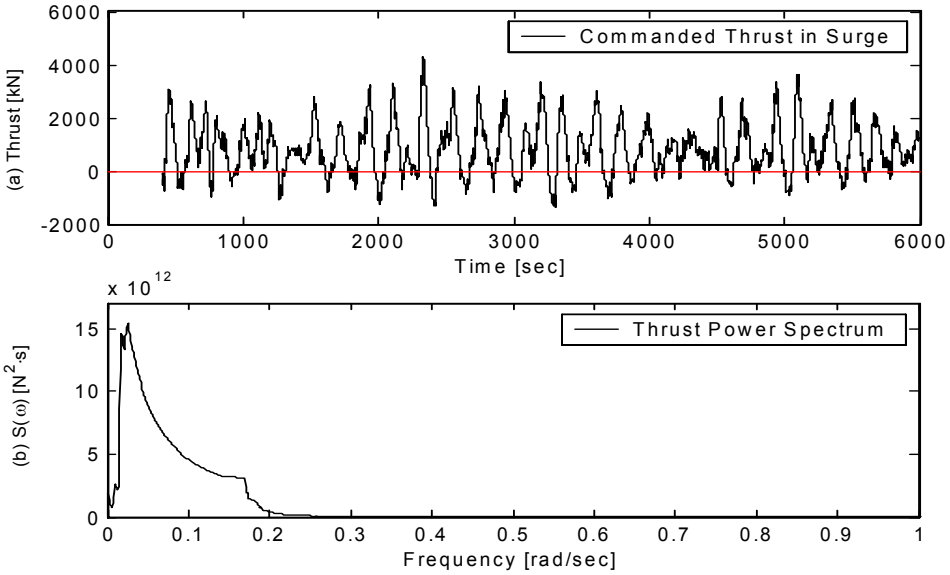

Fig. 6.12. Commanded thrust in surge direction during position-keeping.

(a) Time traces of thrust and (b) its power spectrum.

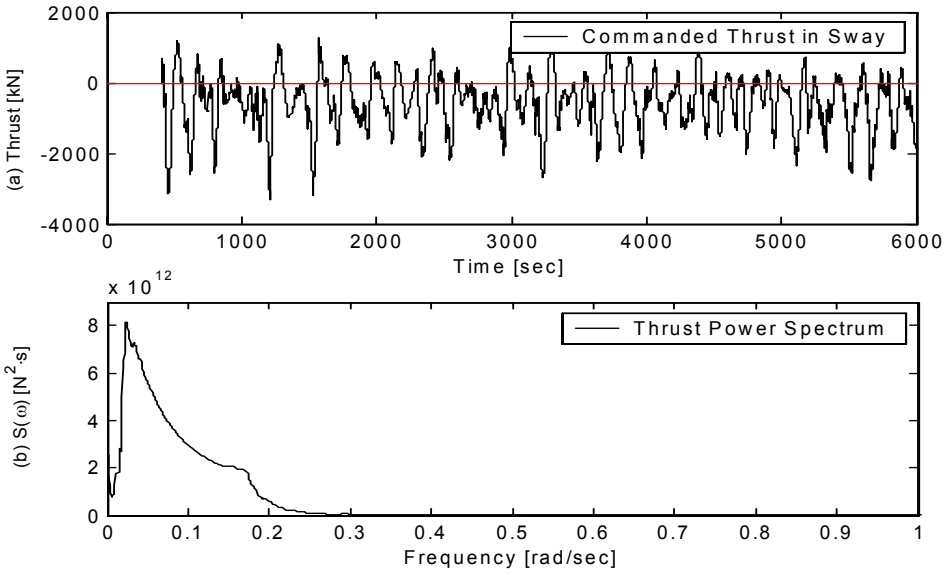

Fig. 6.13. Commanded thrust in sway direction during position-keeping.

(a) Time traces of thrust and (b) its power spectrum.

forces have relatively small *STD* values.

Table 6.6

Statistical Results of Commanded Thrusts in Surge and Sway

Thrust in Surge [kN]			Thrust in Sway [kN]		
Mean	*STD*	Extreme	Mean	*STD*	Extreme
832	975	4287	-556	778	-3302

6.5.3. Improvement of Global Motions of FPSO

To implement the "natural weathervaning" feature of a turret, the derivative and proportional gains, D_ψ and P_ψ in Eq. (4.9), are set to zero in this study case. By weathervaning the FPSO is headed to an optimized yaw angle minimizing environmental forces. For this reason, an active heading angle control of the FPSO was intentionally not considered in this simulation. However, in some practical applications, active heading angle would be able to give advantages over the weathervaning in terms of minimizing the environmental force effects since the environmental forces may vary drastically in many cases.

To evaluate what merits the assisting thrusters would provide for an FPSO, the FPSO hull global motions and the mooring/riser top tensions are investigated by means of a spectral analysis and statistical analysis for the two cases: (1) a turret-moored FPSO without thruster system and (2) a thruster-assisted turret-moored FPSO. Two horizontal, translational motions, i.e. surge and sway, are mainly emphasized since the thruster

applications, in general, aim at the horizontal motion reduction.

It is also beneficial to evaluate what changes might occur in other motions when the thruster system is applied since a floating structure has coupling effects among 6DOF motions. Those motions, as well as surge and sway, must have different behavior when thrusters are applied depending on the commanded thruster forces and their locations. For this reason, the spectra of all 6DOF motions are shown in Figs. 6.14 through 6.19, and the statistical analysis results are summarized in Table 6.7. All motions were given at the turret center on the still water level rather than at the center of gravity.

According to the spectra, the LF (<0.2rad/s) *STD* values of all motions, except for roll, are reduced when the thrusters are applied, while WF *STD* values remain almost the same as expected. Especially, as shown in Fig. 6.14, surge motion spectrum is significantly reduced with the assist of the thrust.

The trajectories of the FPSO turret center at the mean water level are shown in Fig. 6.20.

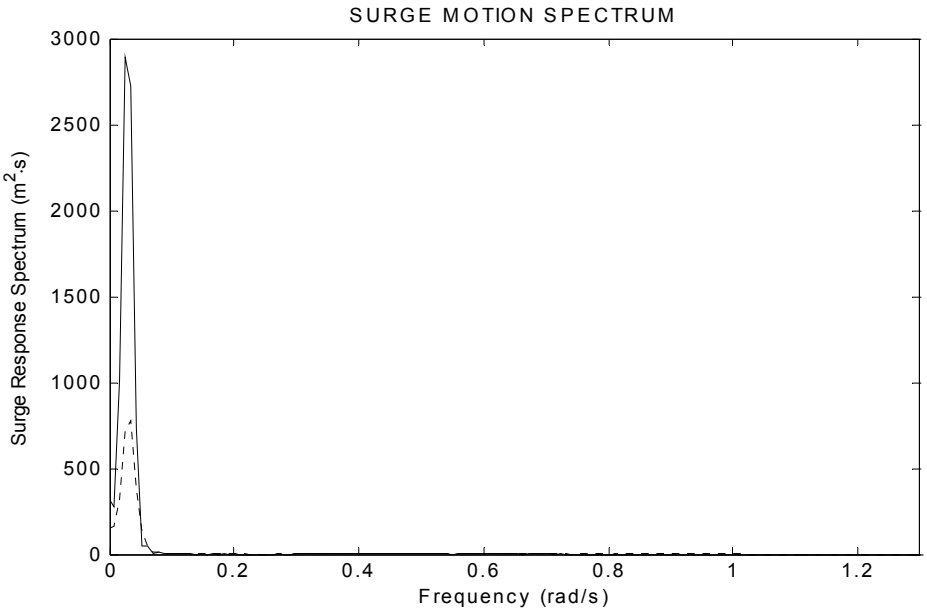

Fig. 6.14. Surge motion spectra:

(a) solid line – no thruster and (b) dotted line – with thruster.

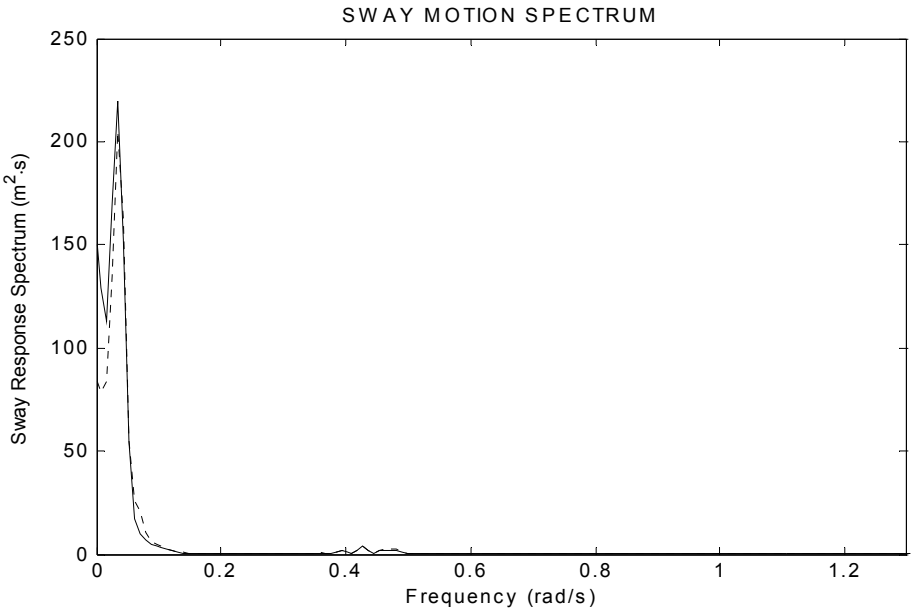

Fig. 6.15. Sway motion spectra:

(a) solid line – no thruster and (b) dotted line – with thruster.

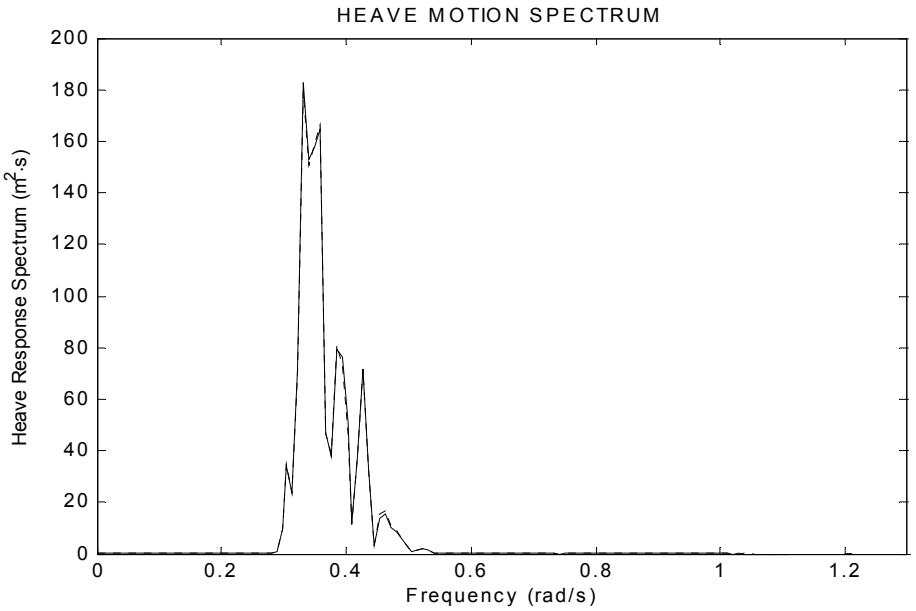

Fig. 6.16. Heave motion spectra:

(a) solid line – no thruster and (b) dotted line – with thruster.

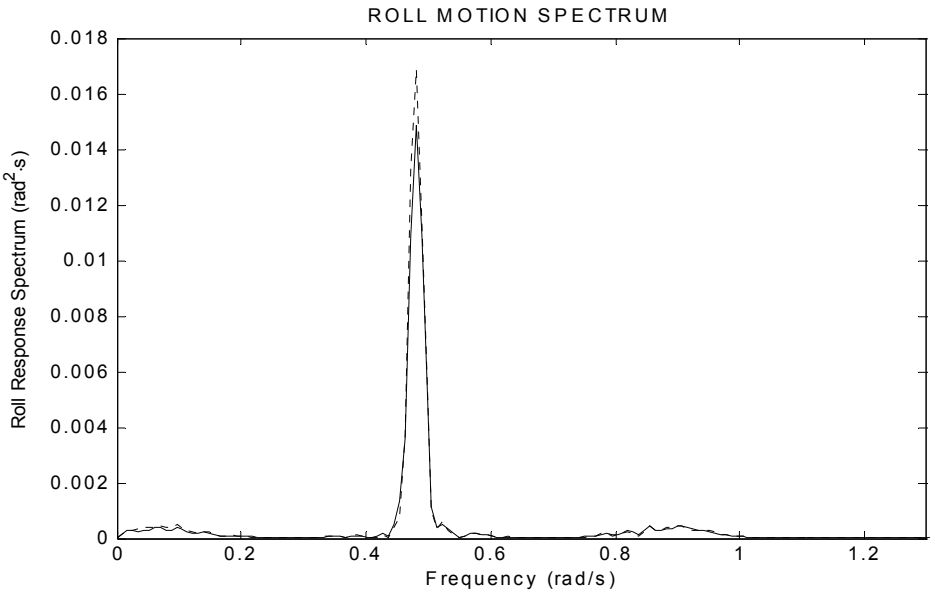

Fig. 6.17. Roll motion spectra:

(a) solid line – no thruster and (b) dotted line – with thruster.

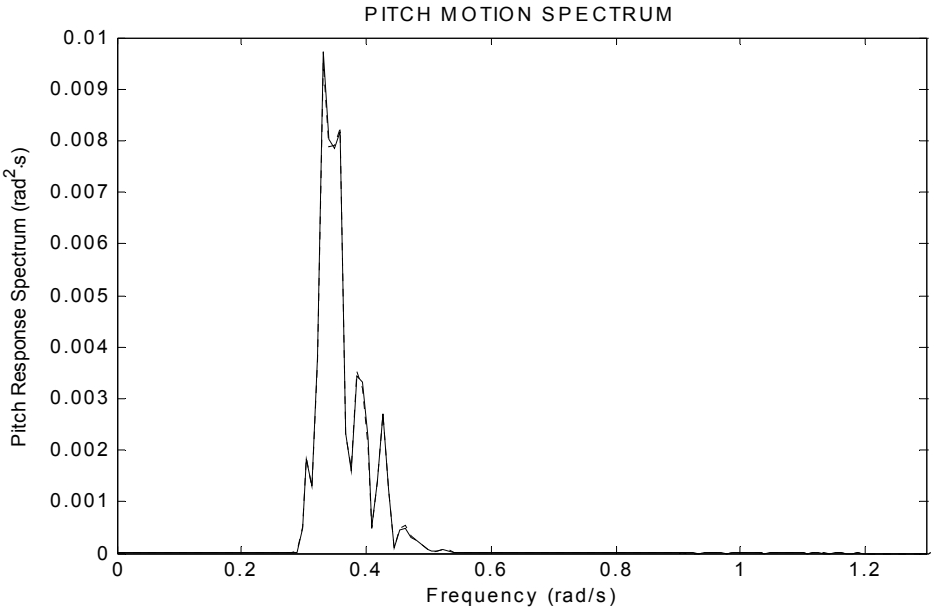

Fig. 6.18. Pitch motion spectra:

(a) solid line – no thruster and (b) dotted line – with thruster.

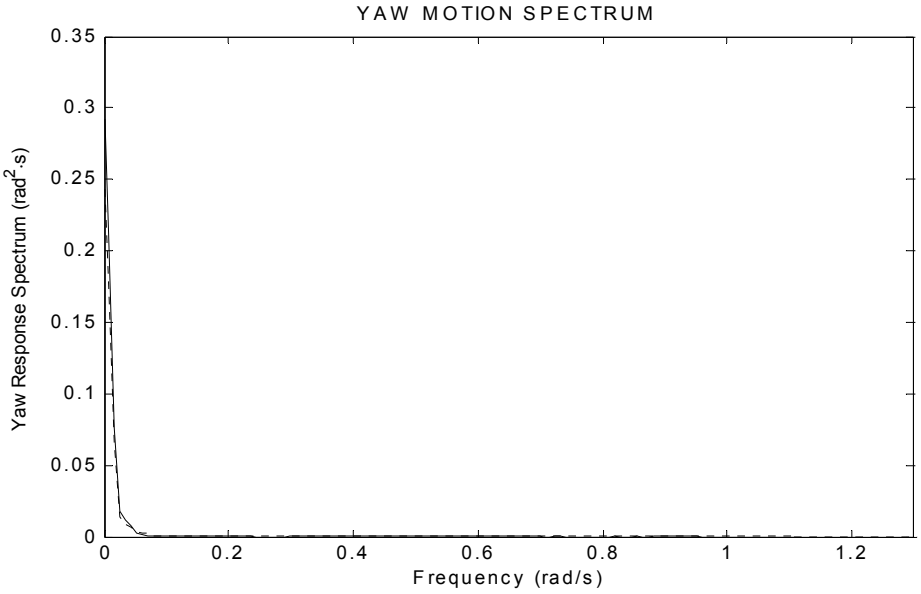

Fig. 6.19. Yaw motion spectra:

(a) solid line – no thruster and (b) dotted line – with thruster.

Table 6.7

Comparisons of Statistical Results of FPSO Hull Motions at Turret (unit: meter, degree)

	Thruster	Mean	LF *STD*	WF *STD*	Total *STD*	Max
Surge	Yes	-12.36	4.81	0.43	4.83	-26.99
	No	-14.65	8.31	0.42	8.32	-37.13
Sway	Yes	4.58	2.71	0.52	2.76	16.52
	No	4.91	2.91	0.49	2.95	14.56
Heave	Yes	0.07	0.07	3.38	3.38	10.73
	No	0.07	0.07	3.38	3.39	11.02
Roll	Yes	0.16	0.41	1.35	1.41	5.76
	No	0.16	0.39	1.30	1.36	4.33
Pitch	Yes	-0.01	0.04	1.33	1.33	-4.28
	No	-0.01	0.04	1.34	1.34	-4.42
Yaw	Yes	16.68	3.41	0.32	3.42	23.87
	No	15.70	3.70	0.29	3.71	25.42

From Table 6.7, it is found that LF *STD* and total *STD* values in surge are reduced when thrusters are applied. In general, thruster applications for the large water-plane-area platforms are not targeted for the improvement of vertical-plane motions. In addition, it is noted that the yaw motion is intentionally not controlled for the weathervaning and that the roll motion was affected from the depth of applied thrust in sway direction.

According to the results of mean yaw angle, the wind direction is the driving cause for the mean yaw angle of the FPSO, while the current and wave forces would affect the minor mean heading angle change. The low- and wave-frequency (WF) regions are defined as 0~0.2 rad/s and 0.2~1.3 rad/s, respectively. Conclusively, the mean, *STD*, and extreme values in surge are mainly reduced when thrusters are applied.

The motion amplitude in the X-direction is mainly reduced compared to the one in the

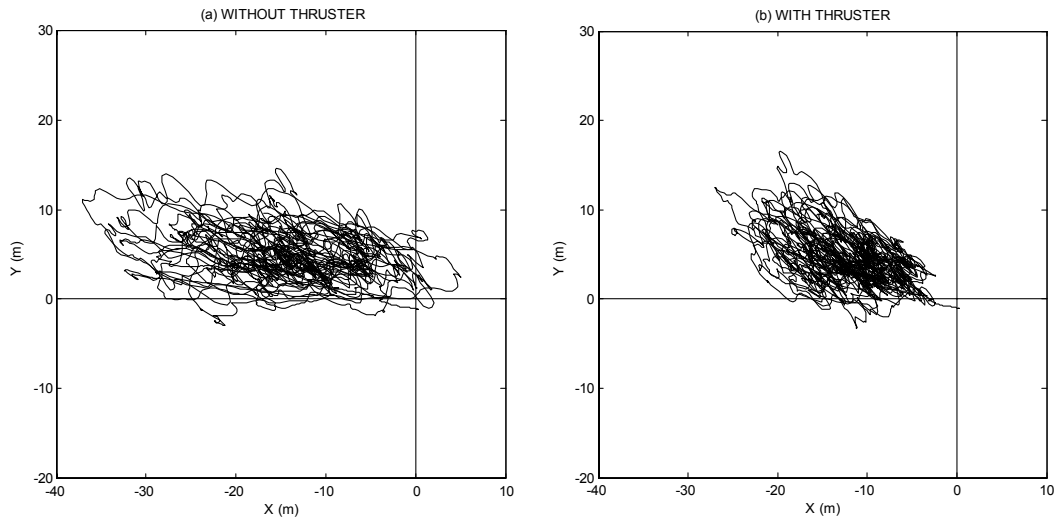

Fig. 6.20. Comparison of the turret position trajectories simulated (a) without thruster-assisted system and (b) with one. The total time duration is 6000 seconds.

Y-direction as shown in Figs. 6.20 through 6.22. The reason is that the wave exciting force is acting on 180 degrees and is the most dynamically fluctuating force compared to the low

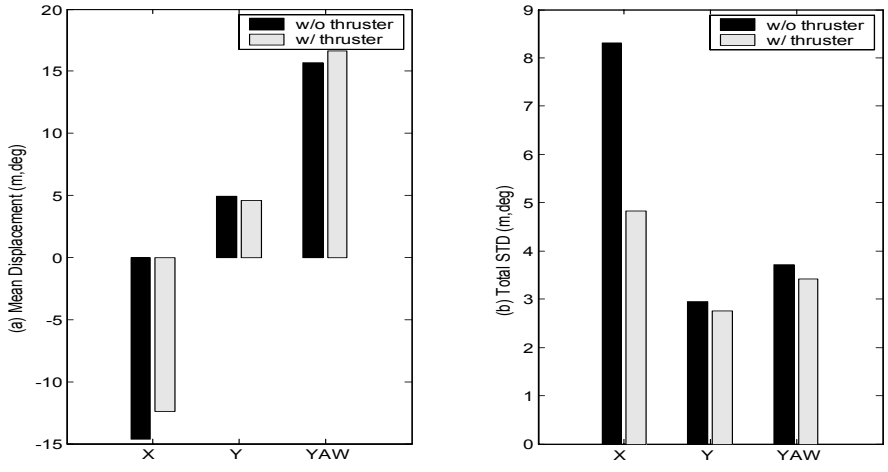

Fig. 6.21. Statistical analysis of the horizontal-plane motion of the turret center. Comparisons of (a) mean displacement and (b) total *STD* of the two cases: without thruster and with thruster.

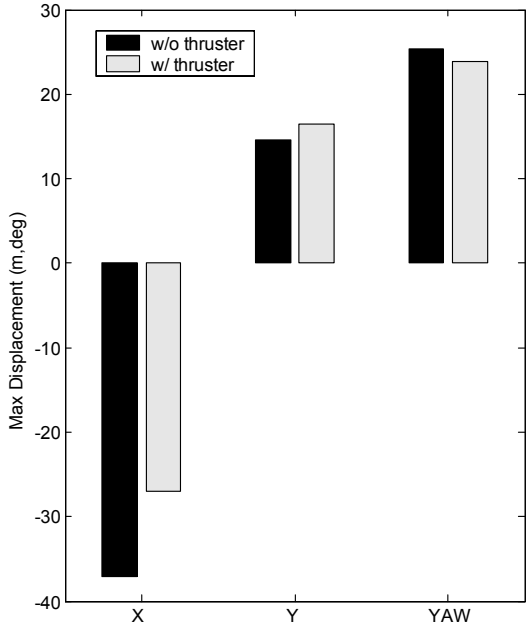

Fig. 6.22. Maximum displacement comparisons:

Black – without thruster and gray – with thrusters.

frequency environmental forces such as wind and current forces. In general, wind and current forces may affect the mean position while the wave exciting force causes the dynamic effect on a structure. However, the extreme values are constructed by the combinations of both mean and standard deviation values.

The time series of all 6DOF motions for the cases with thruster and without are shown in Figs. 6.23 and 6.24.

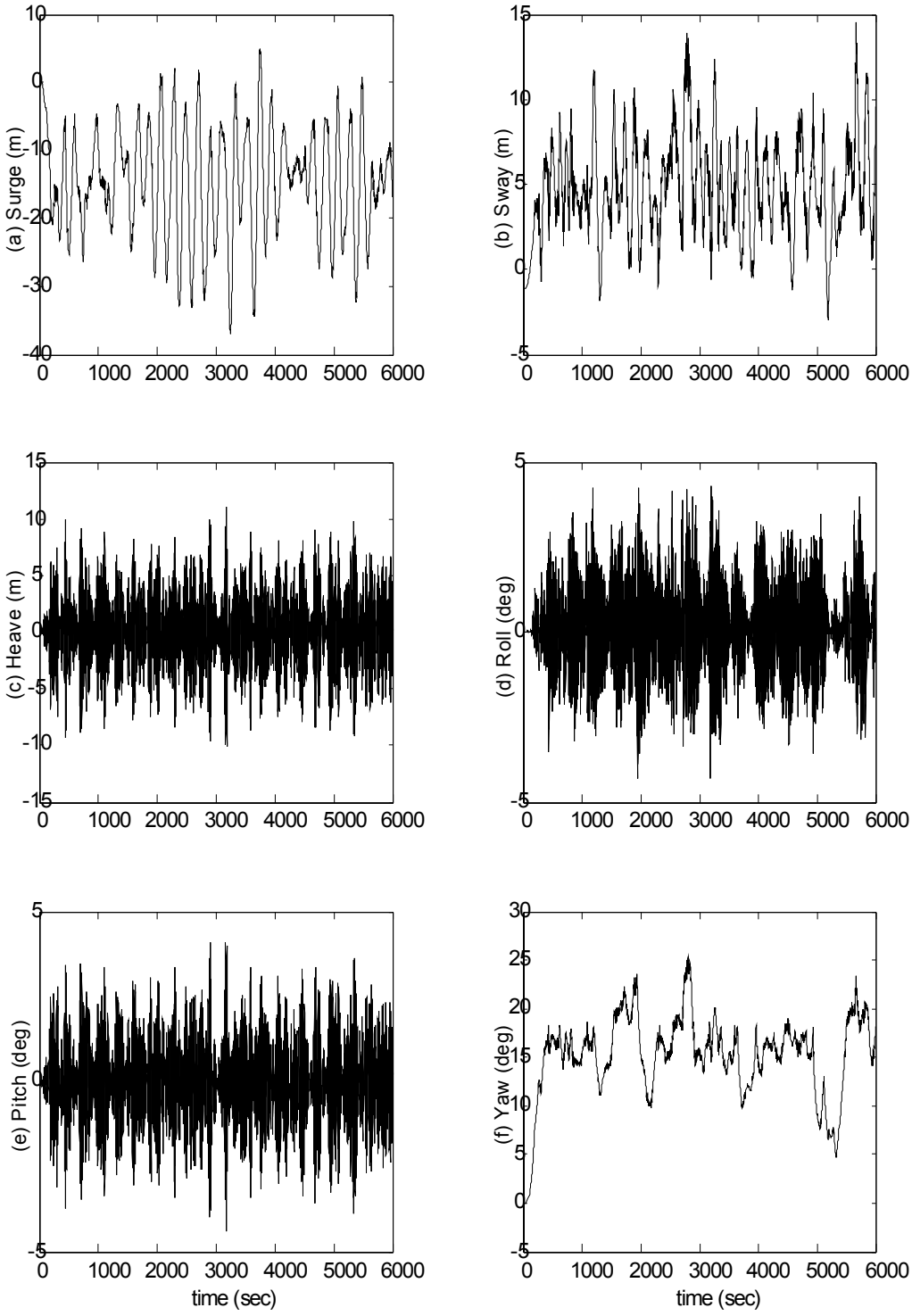

Fig. 6.23. Time series of all 6DOF motions of FPSO at the turret center when there is no thruster assist.

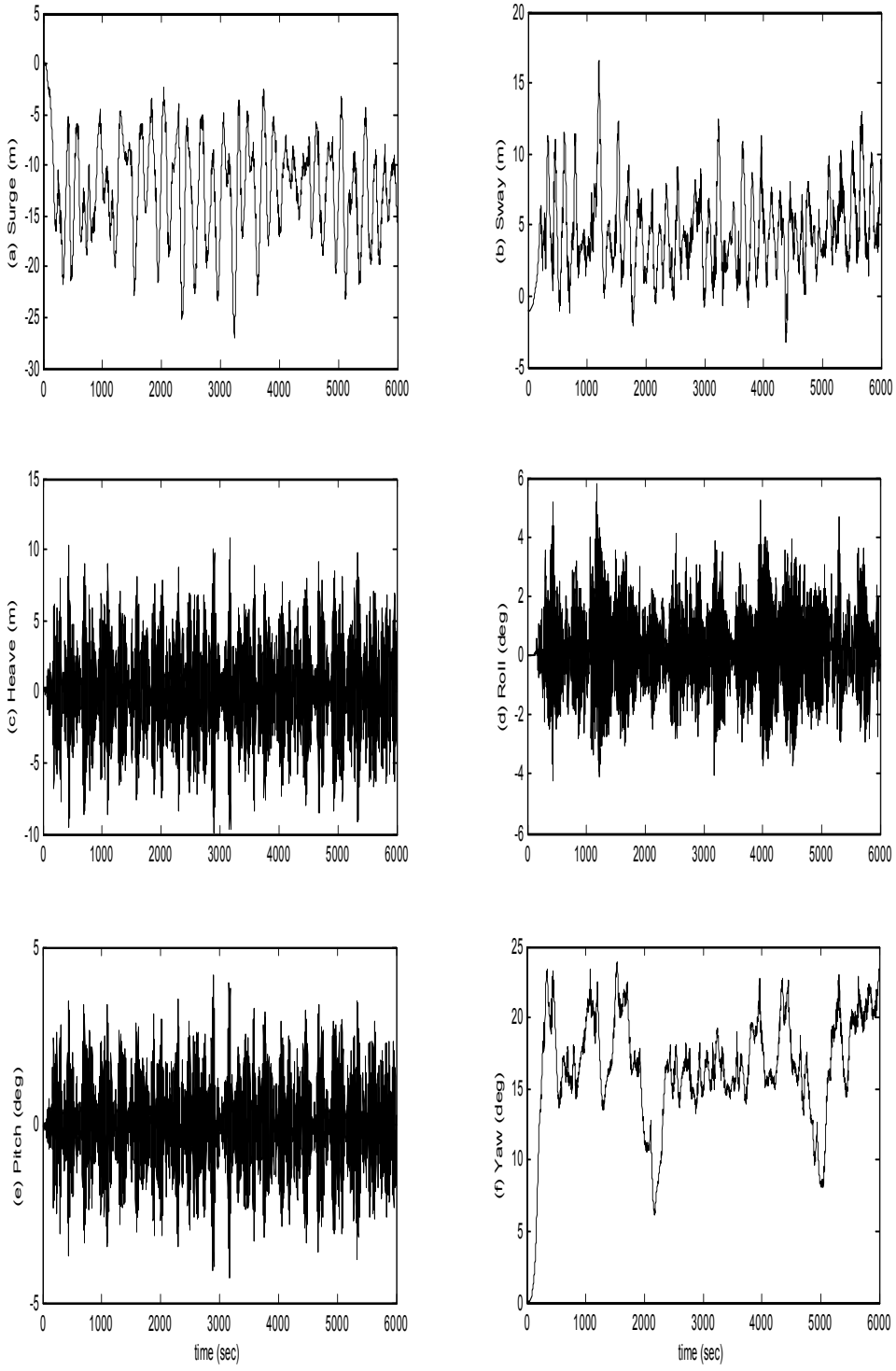

Fig. 6.24. Time series of all 6DOF motions of FPSO at the turret center when the thruster forces are applied.

6.5.4. Reduction of Mooring/Riser Top Tensions

In Table 6.8, the mean top tension of mooring line No. 2 (taut side) is decreased after applying the thrusters, while that of mooring line No. 8 (slack side) is increased. This is because of the direction of the environmental forces and the fact that the taut side becomes less taut and the slack side less slack. At any rate, the maximum tension of the mooring line No. 2 is reduced by 20% by applying the thruster assist system. This improvement is assumed to be even larger in a 10-yr storm environment, which is an operation condition. Therefore, the vessel is closer to the origin and the two mooring line top tensions become closer to those at the undisturbed condition.

Table 6.8

Comparison of mooring line/riser top tensions (unit: kN)

Leg Type and ID #	Thruster	Mean	Total *STD*	Max
Mooring Line #2	Yes	2074	298	2938
	No	2203	463	3460
Mooring Line #8	Yes	933	228	1673
	No	897	290	2047
Liquid Production Riser #13	Yes	2338	256	4716
	No	2344	266	4641
Gas Production Riser #20	Yes	1249	264	3212
	No	1255	277	4031
Water Injection Riser #22	Yes	4277	399	8108
	No	4284	400	8886
Gas Injection Riser #23	Yes	2742	226	3672
	No	2745	225	3717
Gas Export Riser #25	Yes	958	167	1762
	No	961	164	1740

According to Table 6.8, the top tension change can not be proportional since each mooring line or riser has different location, material, etc. For instance, when thrusters are applied, it can reduce the top tension of mooring line No. 2 by 15%. This reduction of the top tensions of mooring lines and risers clearly demonstrates the benefit of employing a thruster-assisted position-keeping system. On the other hand, mooring line No. 8 is on the slack side so that the mean top tension increases when thrusters are applied.

6.5.5. Kalman Filter Performance

A Kalman filter was employed in this case study, taking into consideration the fact that wave frequency and high frequency motion responses need to be filtered out of the signal fed to the controller to avoid thruster wear and tear. Time series of X-, Y-, and Yaw-motions, and their velocities of the turret center are shown in Figs. 6.25 and 6.26, respectively. As mentioned in chapter 4, the filtered displacement and velocity signals are used for the *P* and *D* control, respectively. To verify how well the implemented Kalman filter performs, X- and Y-motion energy spectra were obtained and are shown in Figs. 6.27 and 6.28. The solid line represents the spectrum obtained from the non-filtered signal, and the dotted line represents the spectrum obtained from the filtered signal. The spectra clearly show that the filter performs better in displacements than in velocities.

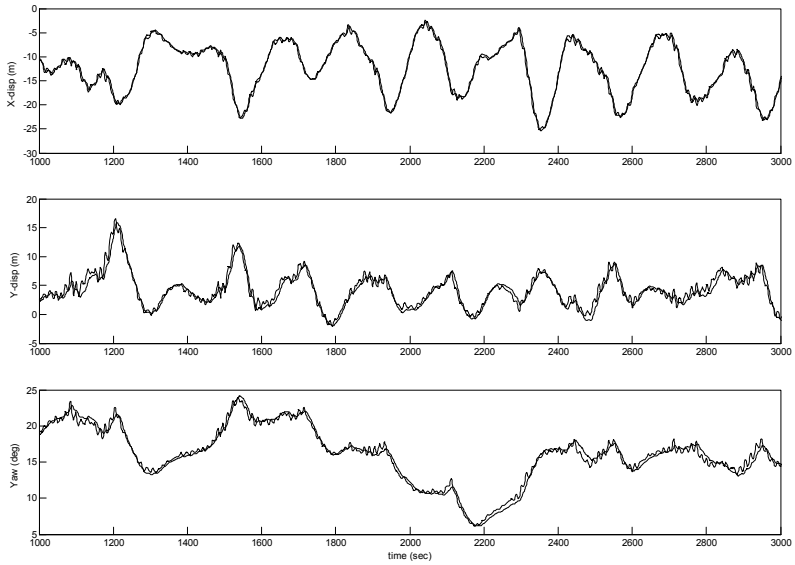

Fig. 6.25. Displacement time series of original signals (rough) and their low frequency estimates (smooth) at the turret center obtained by applying Kalman filter: (a) X-displacement, (b) Y-displacement, and (c) yaw-angle.

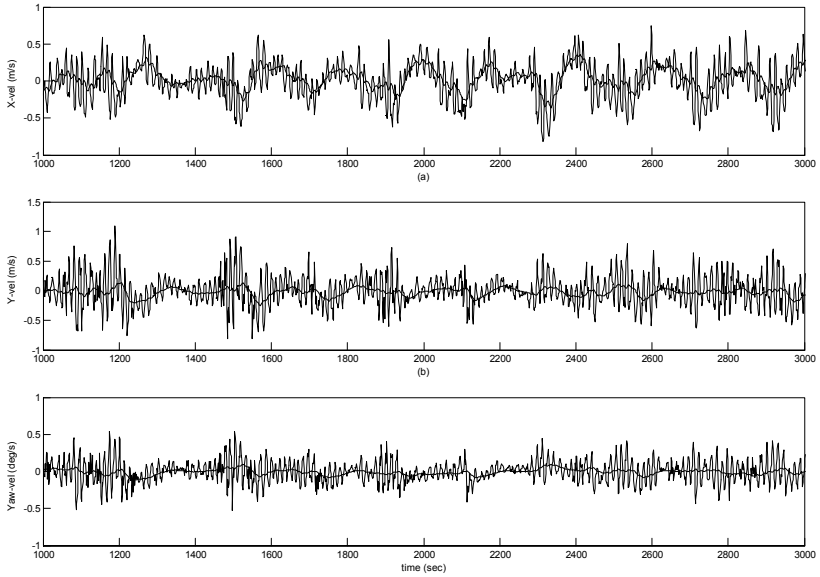

Fig. 6.26. Velocity time series of original signals (rough) and their low frequency estimates (smooth) at the turret center obtained by applying Kalman filter: (a) X-velocity, (b) Y-velocity, and (c) yaw-velocity.

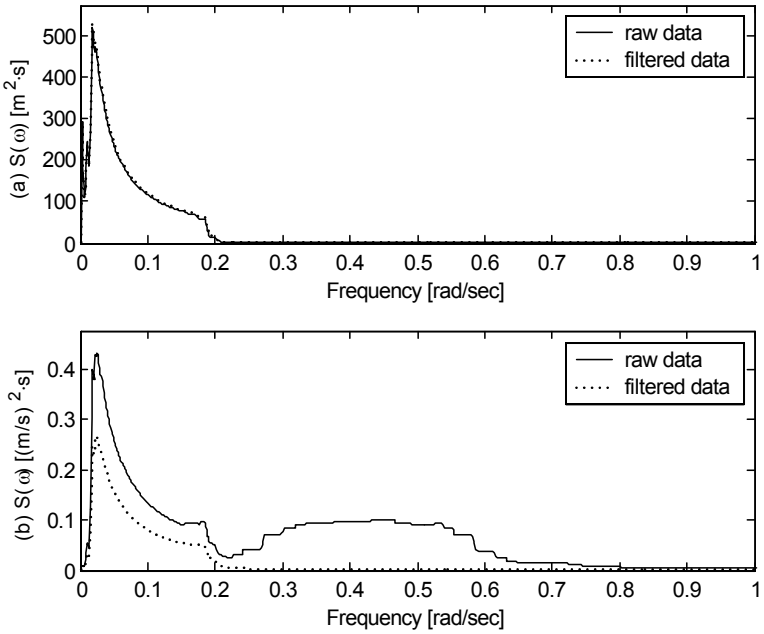

Fig. 6.27. Surge (a) motion and (b) velocity energy density spectra.

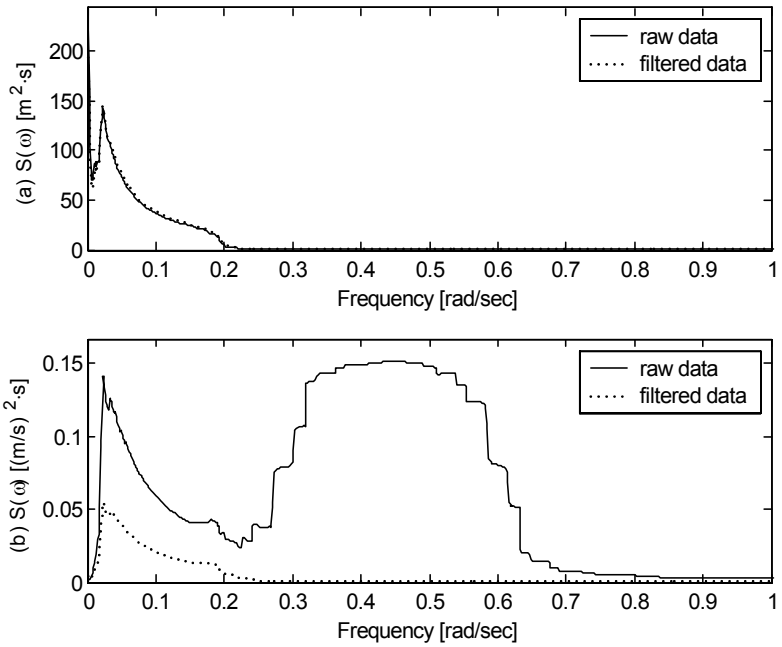

Fig. 6.28. Sway (a) motion and (b) velocity energy density spectra.

In general, for shallow water applications, DP or thruster applications would be used as an additional damping force since mooring lines have relatively high stiffness compared to the deep water cases. On the other hand, for deep water applications, the mooring line stiffness in the horizontal-plane motions is relatively small so that the thruster application should be used as an additional restoring force, i.e. springs. Therefore, in this study case, *P* control (spring effect) is emphasized more than the *D* control (damper effect). In turret-moored FPSO simulations, all three horizontal-plane motions, i.e. surge, sway, and yaw, are low frequency dominant motions, but their velocity signals have wave frequency components which need filtering for the P(I)D control.

6.5.6. Thruster Depth Effect

In previous simulation, it was assumed that the commanded thrust was applied on the still water level, which is not practical. In this case study, two thruster depths are considered: (1) the still water level (SWL) and (2) 16*m* below the still water level. Based on the results, the shallower thruster depth gives better motion performance especially in sway and roll motions. For the roll motion the thruster depth can be important. In FPSO case, since the water-plane-area is not small so that the pitch restoring moment is large enough, the rotational motion changes may not be significant. However, the roll of the FPSO can be affected significantly since the roll restoring moment is relatively small compared to the pitch.

In general, the pitch and roll motions of the platforms with relatively small water-

plane-areas such as spars and semi-submersibles can be affected by the thruster depth significantly. For two different thruster depths The global motions of the FPSO are summarized in Table 6.9.

Table 6.9

Comparisons of Statistical Results of FPSO Hull Motions for Different Thruster Depths (unit: meter, degree)

	Thruster Depth	Mean	LF *STD*	WF *STD*	Total *STD*	Max
Surge	SWL	-12.36	4.81	0.43	4.83	-26.99
	-16m	-12.15	4.72	0.43	4.74	-26.73
Sway	SWL	4.58	2.71	0.52	2.76	16.52
	-16m	4.00	2.59	0.46	2.63	12.58
Heave	SWL	0.07	0.07	3.38	3.38	10.73
	-16m	0.07	0.07	3.37	3.37	10.69
Roll	SWL	0.16	0.41	1.35	1.41	5.76
	-16m	0.15	0.38	1.24	1.30	4.99
Pitch	SWL	-0.01	0.04	1.33	1.33	-4.28
	-16m	-0.01	0.04	1.33	1.33	-4.27
Yaw	SWL	16.68	3.41	0.32	3.42	23.87
	-16m	15.44	3.41	0.30	3.42	23.17

6.5.7. Increase of Thruster Contribution

Based on the previous results of the global motion comparisons, if increased P gains are applied, the contribution of thrusters in positioning can be increased. In this regard, it is important to get reasonable P gains to counteract the environmental forces. First of all, the static offset curve shown in Fig. 6.29 should be the fundamental guideline to choose P

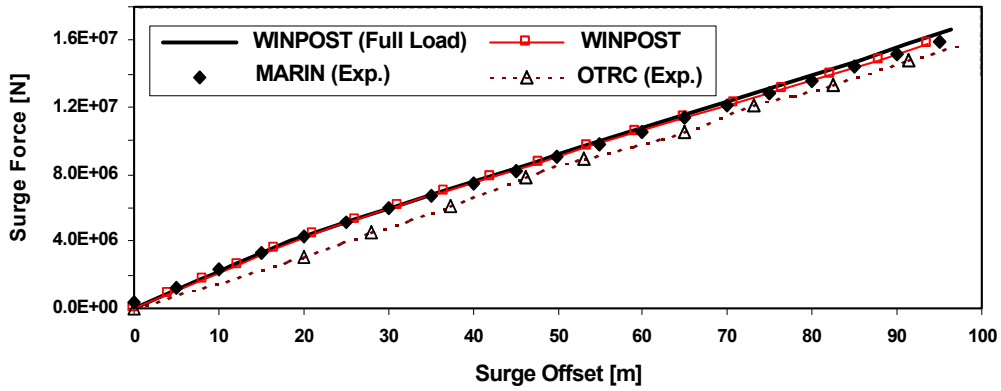

Fig. 6.29. Static offset curves for surge motion obtained by experiments and WINPOST-FPSO (Kim et al., 2003).

gains. Judging from the curve, 800kN/m is selected for the surge and sway P gains. In this procedure, the P gains need to be bounded based on the static offset curve. In other words, if the P gains are too big, thrust ends up to be too stiff compared to the mooring lines. On the other hand, if the P gains are too small, thrust turns out to be too mild for the position-keeping purpose compared to the mooring lines. Once the P gains are judged, the D gains are tuned according to the cost optimization algorithm.

The comparison of FPSO turret center trajectories is shown in Fig. 6.30. The motion amplitude of case (c) in the X-direction is more reduced compared to the case (b). Both cases have thrusters with different PD gains. As shown in Figs. 6.31 and 6.32, the surge and sway motions are more improved.

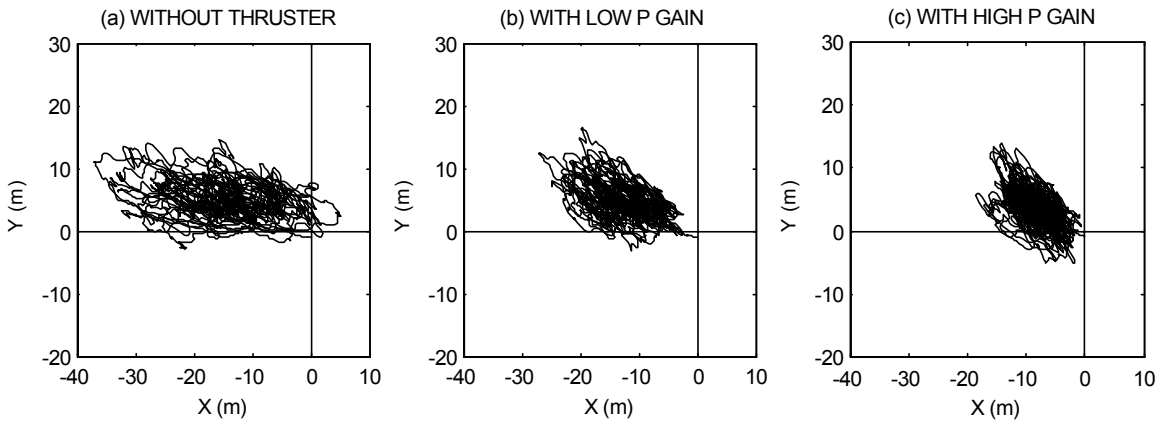

Fig. 6.30. Comparison of the turret position trajectories: (a) without thruster, (b) with low P gain, and (c) with high P gain.

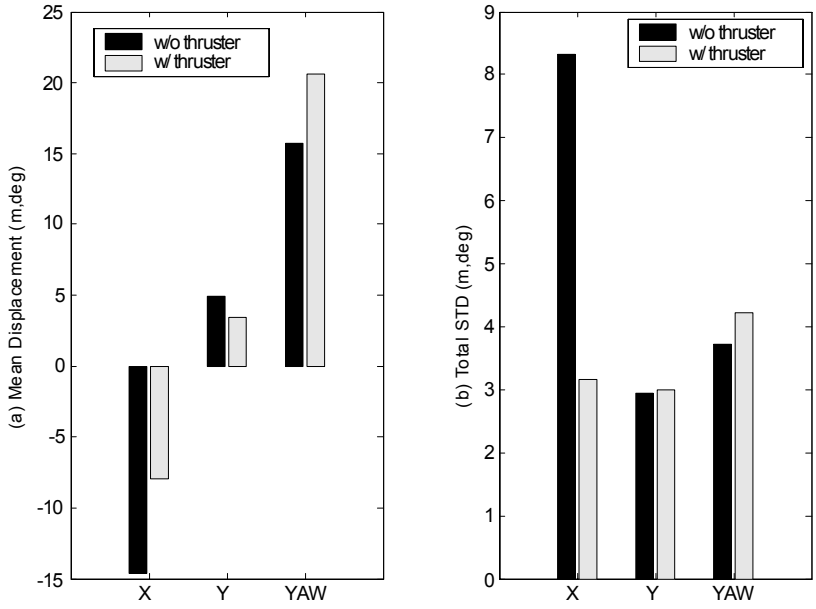

Fig. 6.31. Statistical analysis of the horizontal-plane motion of the turret center. Comparisons of (a) mean displacement and (b) total *STD* of the two cases: without thruster and with high P gains.

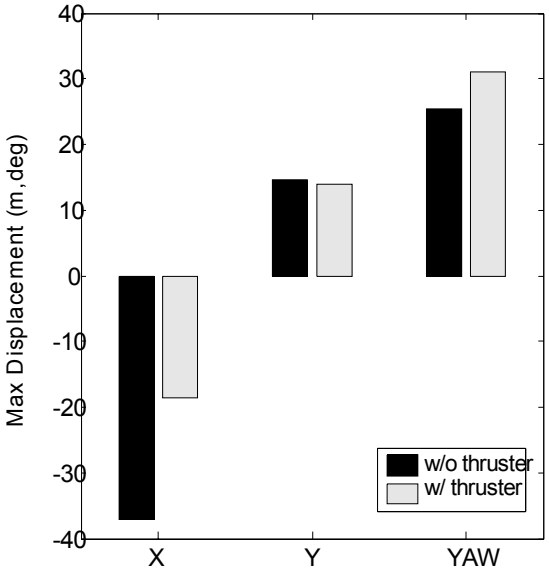

Fig. 6.32. Maximum displacement comparisons:

Black – without thruster and gray – with high P gains.

6.6. Concluding Remarks on Thruster-Assisted Turret Moored FPSO Case

In physics, the restoring force of the mooring lines should have the same order of force as the total sum of the mean environmental forces. Without thruster assist, the surge mean value is -14.65m. When thrusters are applied with high PD gains, the surge mean becomes -7.93m. The static offset curve must be foundational information to design how much contribution of thruster assist we want to apply for the thruster-assisted turret-moored FPSO.

In this study case, a fully coupled dynamic analysis of a thruster-assisted turret-moored FPSO was conducted. It is clearly demonstrated that the vessel horizontal-plane responses as well as mooring and riser tensions can be reduced by applying the thruster-

assisted positioning system. For the roll motion of an FPSO, thruster depth has to be considered properly.

To implement the weathervaning, PD gains for the yaw angle were set to zero. Statistical analysis for the yaw motion shows that the mean yaw angle was affected by the direction of wind forces, and the mean position of the turret center was mainly affected by the current force in this case study. An active yaw angle control is not considered in this study.

This case study stresses that a thruster-assisted turret-moored FPSOs can be a possible solution for the ultra-deep water production. Furthermore, the numerical results show that assisting thrusters can significantly increase the global performance of the FPSO hull motions and reduce the tension stresses of the mooring lines and risers.

CHAPTER VII

CASE STUDY II: THRUSTER-ASSISTED MOORED SPAR

7.1. Background

Based on the simulation results addressed in the previous chapter, it is expected that the riser/mooring line top tensions can be reduced, and that global motion responses can be improved when thrusters are applied. A number of spars have been installed in the GoM. (For a spar example, see Fig. 7.1.) Compared to FPSOs, spars have better characteristics in heave response since they have a smaller water plane area than FPSOs. However, spars may also have such important issues as the coupling effect between pitch and surge, big current drag force due to a deep draft, VIM (vortex-induced motion), and small capacity.

Although the concept of a thruster-assisted moored spar has not been considered as a practical application in either academia or industry, a coupled dynamic analysis of a

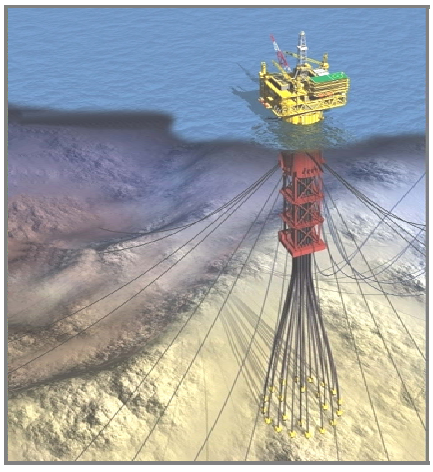

Fig. 7.1. An example of a truss spar and its mooring/riser configuration.

thruster-assisted moored spar is an interesting topic based on the assumption that a spar may have a better global motion performance and less riser/mooring top tensions.

In this chapter, the spar used in the DeepStar project (a joint industry technology development project focused on advancing the technologies needed to drill and produce hydrocarbons) was adopted and analyzed. The spar moored by 14 mooring lines with 23 buoyancy-can supported vertical risers designed for 914.4m (=3,000ft) water depth is numerically simulated to investigate the characteristics of global motion behaviors based on hull/mooring/riser dynamic coupling. A coupled dynamic analysis of the global motion of the same spar by considering the buoyancy-can effects and its relevant analysis such as free decay tests and each 6-DOF motion analysis were thoroughly conducted and verified by Koo (2003).

First, the particulars of the spar hull, mooring lines, risers are addressed. Secondly, mesh generation and hydrodynamic calculation are described. Thirdly, several time-domain analyses are conducted for the global spar motion performance and riser/mooring line top tensions in the 100-yr GoM hurricane. The global spar motion and riser/mooring line top tensions in a damaged condition are also compared with the case in an intact condition. Finally, the same analysis for the spar in a 10-yr operational condition is carried out.

7.2. Spar Platform, Mooring Line, and Riser Particulars

The simplified side view and top view of the spar are shown in Fig. 7.2, and its main parameters are given in Table 7.1. The spar is 214.88m high with the diameter of 37.19m. Its average draft is 198.12m for a loading condition.

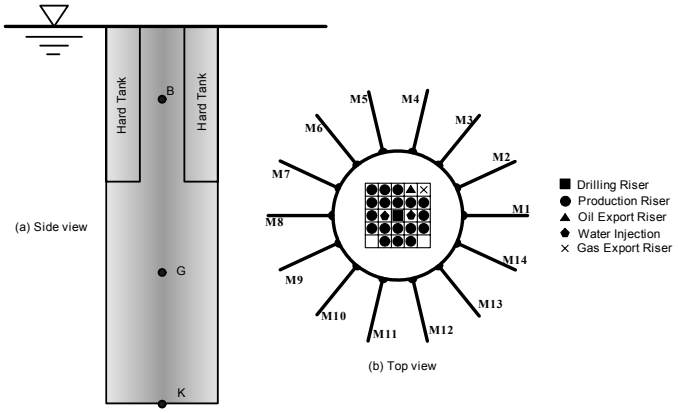

Fig. 7.2. (a) Side view and (b) top view of the spar platform used for case study and mooring/riser arrangements and numbering of mooring lines.

Table 7.1

Spar Platform Particulars

Designation	Unit	Quantity
Length	m	214.88
Diameter	m	37.19
Draft	m	198.12
Hard tank depth	m	67.06
Well bay dimension (25 slots)	m	17.7× 17.7
KB	m	164.59
KG	m	125.7
KG (based on total displacement)	m	89.27
Light ship weight	N	5.673E+08
Displacement	N	2.214E+09
Water weight (ballast tank and moon-pool)	N	1.564E+09
Vertical mooring tension	N	3.219E+07
Vertical riser tension	N	5.034E+07
Pitch radius of gyration	m	66.228
Yaw radius of gyration	m	12.829
Drag coefficient	-	1.5

The spar has 14 mooring lines and 23 buoyancy-can supported vertical risers, whose arrangement/numbering is shown in Fig. 7.2. The configurations and particulars of the mooring lines and riser are given in Table 7.2 through Table 7.4.

Table 7.2

Mooring Line Configuration

Directional Spread	Omni-direction
Total Number of Mooring Lines	14
Chain	5 – ¼″ K4 Studless Chain
Wire	5 – ⅜″ Sheathed Wire

Table 7.3

Mooring Line Particulars

Mooring Lines	Dry/Wet weight (N/m)	Axial Stiffness (kN)	Added mass (N/m)
5 – ¼″ K4 Studless Chain	370.93 / 322.71	1.328E+06	48.22
5 – ⅜″ Sheathed Wire	99.10 / 19.79	1.628E+06	19.79

Table 7.4

Riser Particulars

Riser	Total No.	Top Tension (kN) At Keel/Top of spar	Axial Stiffness (kN)	Dry/Wet Weight (N/m)
Drilling	1	3.269E+03 / 4.167E+03	1.201E+07	595.26 / 366.17
Production	18	2.106E+03 / 2.344E+03	2.994E+06	300.61 / 195.12
Water Injection	2	1.362E+03 / 1.443E+03	1.837E+06	103.28 / 64.64
Oil Export	1	1.738E+03 / 1.872E+03	4.626E+06	296.15 / 163.16
Gas Export	1	8.870E+02 / 9.530E+02	4.626E+06	208.34 / 75.35

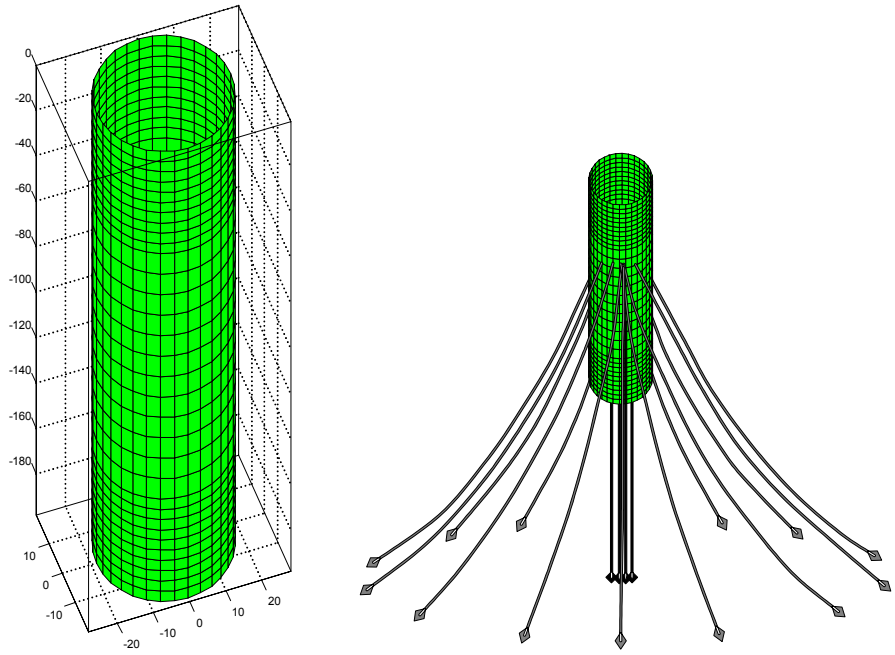

Fig. 7.3. Spar mesh generation and mooring line/riser arrangement (not to scale).

7.3. Mesh Generation and Hydrodynamic Calculation

The mesh generation of the spar platform and the arrangement of hull, mooring lines, and risers are shown in Fig. 7.3 with distorted scale. The added mass and hydrodynamic damping, first-order wave-frequency forces, and second-order mean, and difference-frequency forces are calculated in the frequency domain from the second-order diffraction/radiation program WAMIT (Lee and Korsmeyer, 1999). Since spars do not have significant high frequency motion responses unlike TLPs' springing, the sum-frequency calculation is not included in the motion analysis. As mentioned in the previous chapter, the wave exciting forces obtained from WAMIT are converted to the time domain using two-term Volterra series expansion (Ran and Kim, 1997). The spar hull and the free surface are discretized to 1,504 and 704 panels, respectively.

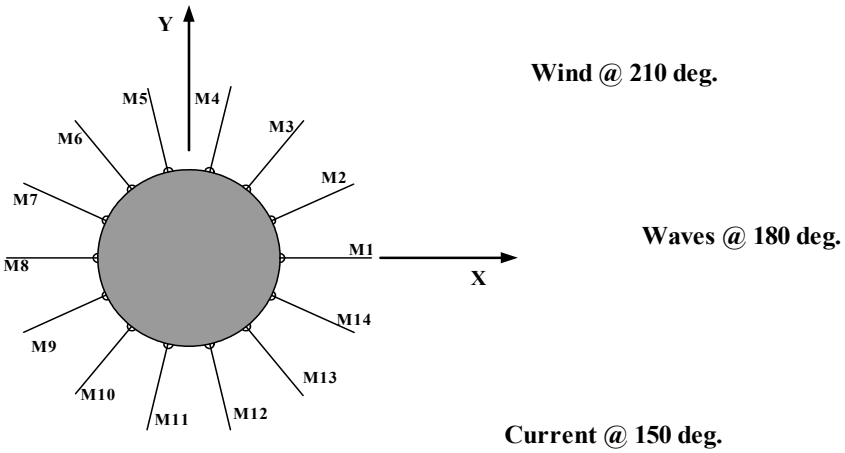

Fig. 7.4. Top view of spar hull and directions of environmental forces.

7.4. Time-Domain Simulation

7.4.1. General

The spar platform has 14 taut-leg omni-directional chain-wire mooring lines, and 23 vertical risers. Each mooring line and riser is modeled as 12 high-order elements. By increasing the number of elements of selected lines, the convergence of the discretized leg can be verified.

The directions of the environmental forces are shown in Fig. 7.4. Irregular waves are used for the numerical simulations and assumed to be uni-directional coming from the positive X-axis. As shown in Fig. 7.5, a JONSWAP spectrum of significant wave height $H_s = 12.19$m (40ft), peak period T_p=14s, and overshoot parameter γ=2.5 was selected to represent a typical 100-yr hurricane in the GoM. The storm induced current

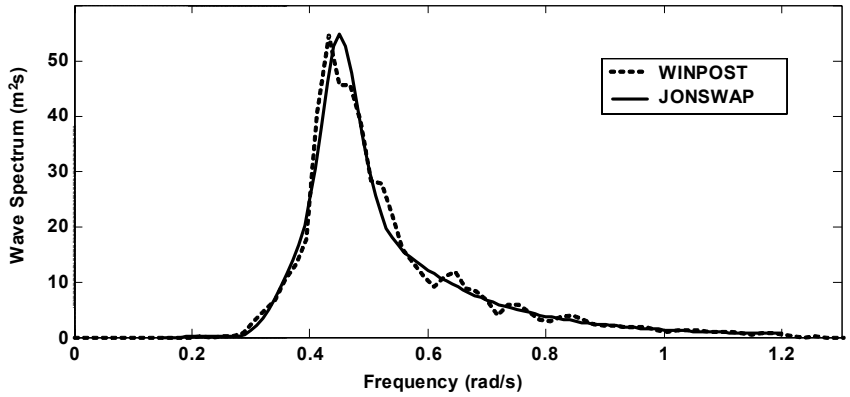

Fig. 7.5. Wave spectra from WINPOST simulation (dotted line) and JONSWAP (solid line) for 100-yr hurricane condition.

flows from 30 degrees right of wave direction. It is assumed that the current is steady, and its velocity is 1.07m/sec from mean water level to 60.96m water depths and is reduced to 0.091m/sec at 91.44m and zero at 914.4m. The wind speed used is 41.1m/sec at 10m above mean water level, and the wind direction is 30 degrees left of wave direction. For the generation of time-varying wind forces, API wind spectrum is used (See Fig. 7.6.).

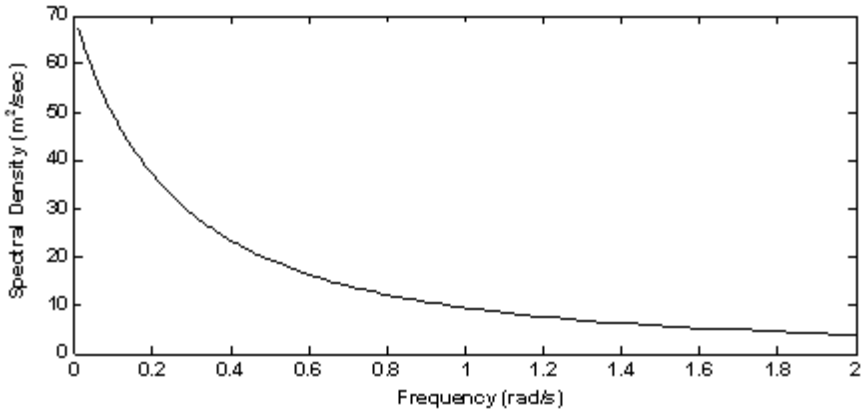

Fig. 7.6. API wind speed spectrum for 100-yr hurricane condition.

The time step used in all numerical simulations is 0.05 seconds, and the total simulation time is 3 hours. The low- and wave-frequency regions are defined as 0~0.2, and 0.2~1.2 (rad/s), respectively.

Following four different cases are investigated: (1) motion and mooring/riser top tension comparison of a thruster-assisted spar and a spar without thrusters, (2) coupled and uncoupled analyses of a thruster-assisted spar, (3) damaged condition comparison for a spar with and without thrusters, and (4) the same analysis as case (1) with 10-yr hurricane in GoM.

7.4.2. Thrust Implementation

In this study case, the installation depth of the thrusters is not concerned. Since the horizontal motion improvement is the main objective in thruster applications, the commanded thruster forces imply the representative forces in surge and sway directions. In addition, it is assumed that the thruster forces act on the mean water level. The maximum thrust limit in both x- and y-directions is predefined as 4×10^6 N.

7.4.3. Case (1): Evaluation of Advantages When Thruster Applied

First, the time traces of the four decomposed environmental forces in X- and Y-directions are shown in Figs. 7.7 and 7.8, and their power spectra are shown in Figs. 7.9 and 7.10. The wave exciting and radiation damping forces are oscillatory forces with higher order of force compared to the other two forces. According to the spectral analysis

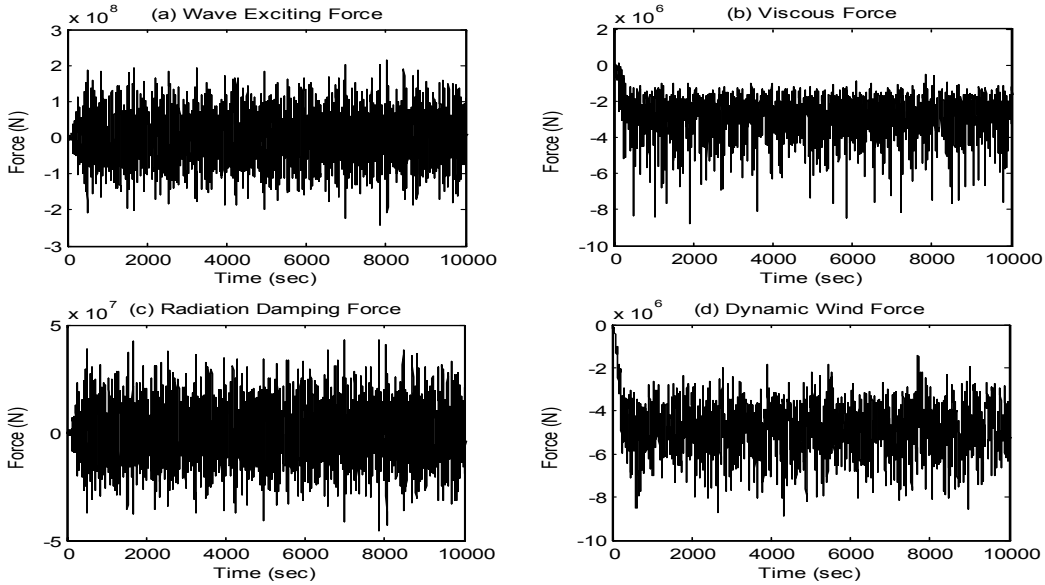

Fig. 7.7. Decomposed external forces in X-direction for 100-yr hurricane case: (a) wave exciting, (b) viscous, (c) radiation damping, and (d) dynamic wind forces.

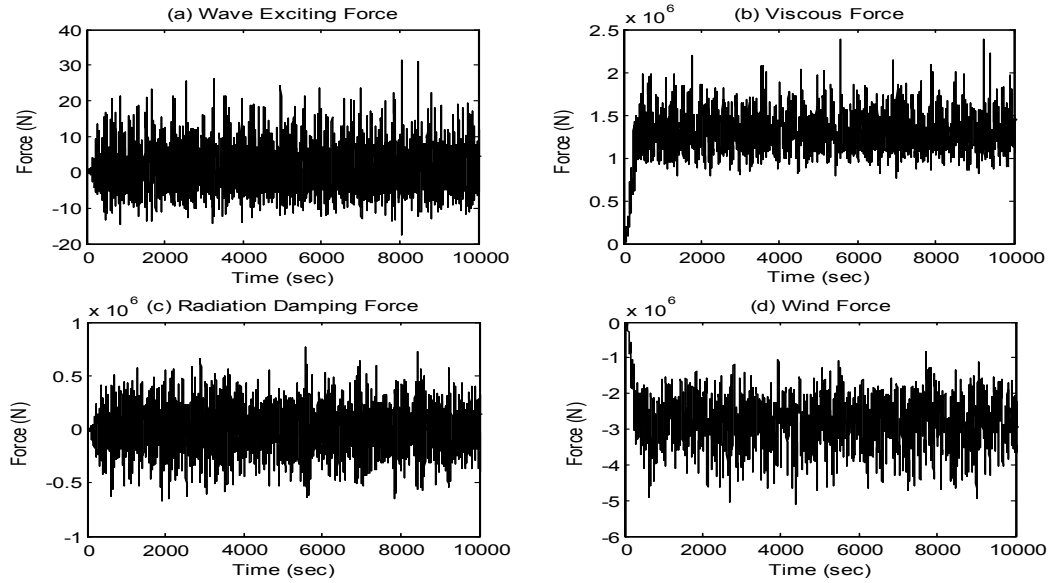

Fig.7.8. Decomposed external forces in Y-direction for 100-yr hurricane case: (a) wave exciting, (b) viscous, (c) radiation damping, and (d) dynamic wind forces.

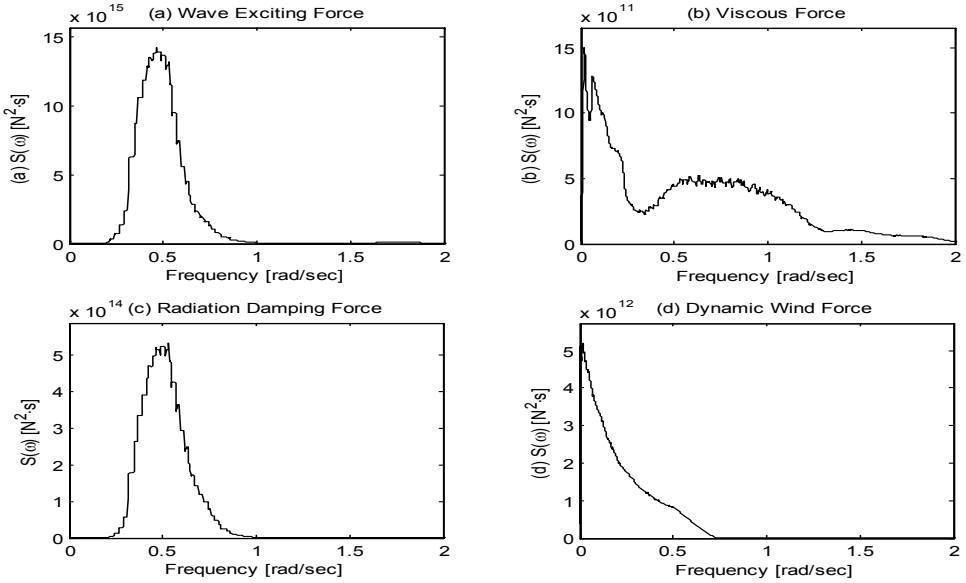

Fig. 7.9. Power spectra of the decomposed external forces in X-direction:
(a) wave exciting, (b) viscous, (c) radiation damping, and (d) dynamic wind forces.

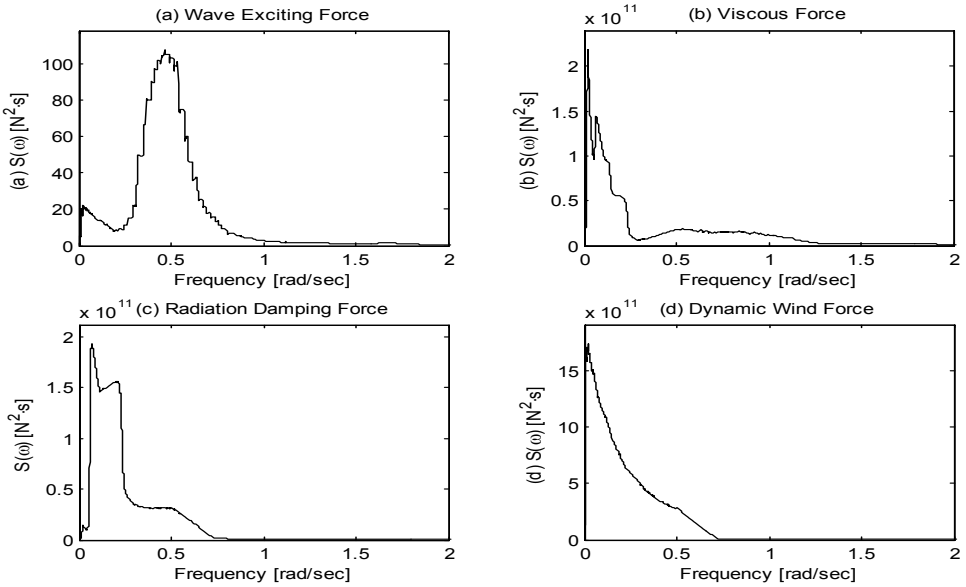

Fig. 7.10. Power spectra of the decomposed external forces in Y-direction:
(a) wave exciting, (b) viscous, (c) radiation damping, and (d) dynamic wind forces.

shown in Figs. 7.9 and 7.10 and the statistical results summarized in Table 7.5, slowly-varying forces, i.e. viscous and wind forces, have the highest order of force in terms of mean value.

Table 7.5

Statistical Results of External Forces Acting on Spar without Thruster for 100-Yr Hurricane in GoM (unit: kN)

	X			**Y**		
Force	Mean	*STD*	Extreme	Mean	*STD*	Extreme
Wave Exciting	-612	61800	-242000	0	0	0
Viscous	-2610	815	-8810	1270	188	2390
Radiation Damping	-1	12200	-45700	0	214	768
Dynamic Wind	-4850	1080	-8860	-2800	622	-5120

On the other hand, as clearly shown in Figs. 7.9 and 7.10, the wave exciting and radiation forces have larger dynamic forces compared to those slowly-varying forces, and their spectrum components are bounded in WF region, which needs to be ignored in DP or thruster-assisted moored platforms.

Secondly, as the slowly-varying active opposing force against the environmental forces, the thruster forces in X- and Y-directions are calculated based on the designed control algorithm which includes a Kalman filter, LQR, and PID controller. Based on tuning, the covariance matrices $\mathbf{Q}$ and $\mathbf{R}$ in Eq. (4.4) and the weighting factor matrices $\mathbf{Q}_o$ and $\mathbf{R}_o$ in LQR Eq. (4.11) are given by

$$\mathbf{Q} = \begin{bmatrix} (4\times10^5)^2 & 0 & 0 \\ 0 & (5\times10^6)^2 & 0 \\ 0 & 0 & (6\times10^8)^2 \end{bmatrix} \quad \text{and} \tag{7.1}$$

$$\mathbf{R} = \begin{bmatrix} (5\times10^{-1})^2 & 0 & 0 \\ 0 & (3\times10^{-2})^2 & 0 \\ 0 & 0 & (4.7\times10^{-3})^2 \end{bmatrix}. \tag{7.2}$$

The PD gains of the matrix $\mathbf{K}$ in Eq. (4.9) are given in Table 7.6.

Table 7.6

PID Gains Used for Thruster-Assisted Spar

P_x [kN/m]	D_x [kNs/m]	P_y [kN/m]	D_y [kNs/m]	P_ψ [kN/rad]	D_ψ [kNs/rad]
100	9240	100	9220	0	0

For the investigation of the commanded thruster forces, the statistical analysis and the spectral analysis were conducted. The statistical results of the thrusts are summarized in Table 7.7.

Table 7.7

Statistical Results of Commanded Thrusts in Surge and Sway

Thrust in Surge [kN]			Thrust in Sway [kN]		
Mean	*STD*	Extreme	Mean	*STD*	Extreme
1325	448	3091	446	495	2094

It is valuable to compare Tables 7.5 and 7.7 to examine how much the thruster system would contribute in the position-keeping operation of the spar. For instance, the amount of the thruster force in surge is 16% of total sum of the mean environmental force in surge;

the thruster force in sway is 29% of total sum of the mean environmental force in sway. In addition, the wave exciting and radiation forces have large *STD* values compared to the viscous and wind forces. On the other hand, the thruster forces have relatively small *STD* values same as the viscous and wind forces.

The time series of the thrust in surge and sway directions and their power spectra are shown in Figs. 7.11 and 7.12. Most of the surge thrust energy is concentrated in LF range, while some of the sway thrust energy is distributed in WF range.

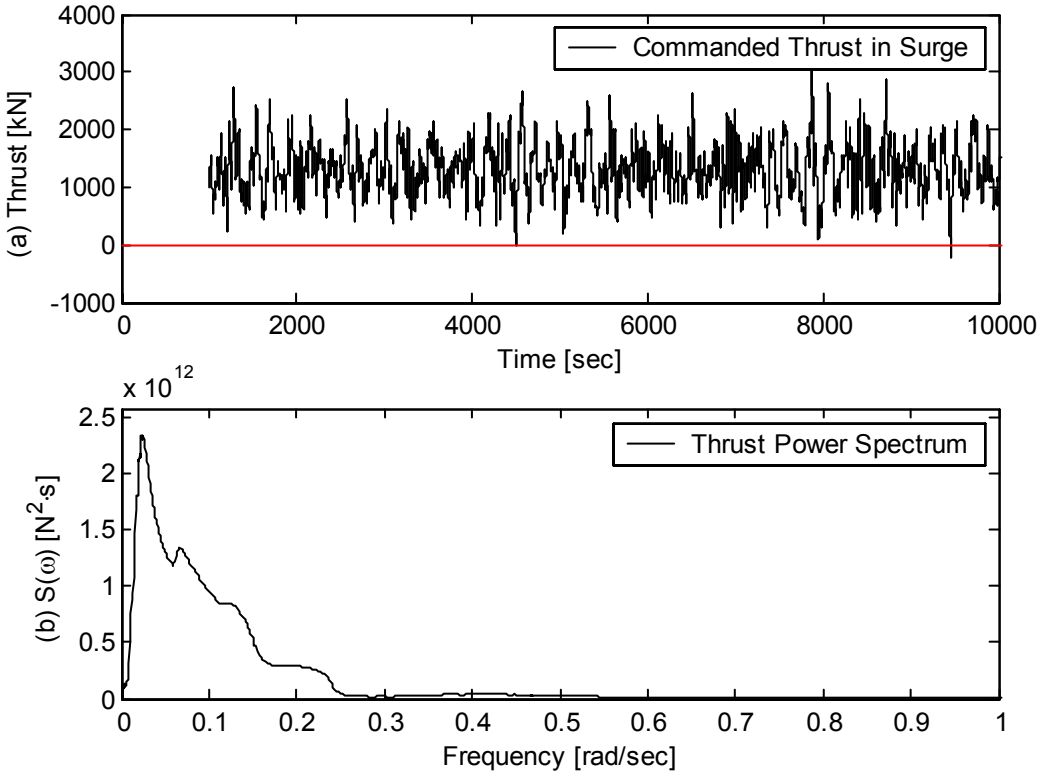

Fig. 7.11. Commanded thrust in surge direction during position-keeping.
(a) Time traces of thrust and (b) its power spectrum.

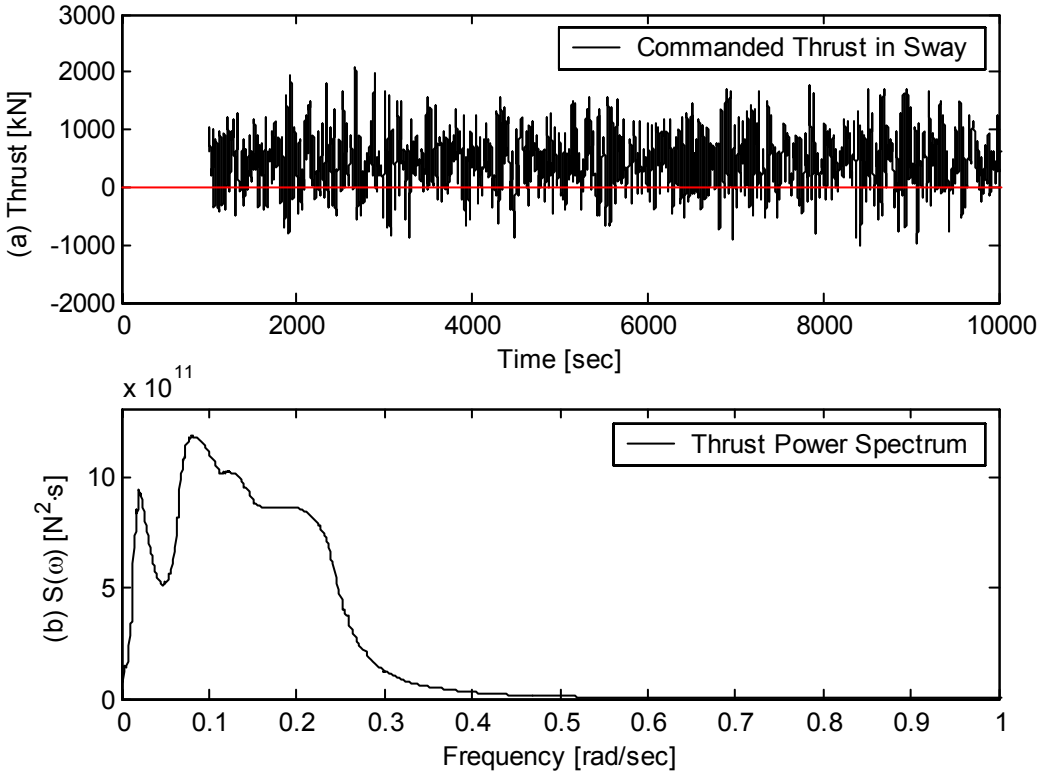

Fig. 7.12. Commanded thrust in sway direction during position-keeping.
(a) Time traces of thrust and (b) its power spectrum.

Thirdly, to evaluate what merits the assisting thrusters would provide for a spar, the spar hull global motions and the mooring/riser top tensions are investigated by means of a spectral analysis and statistical analysis for the two cases: (1) a moored spar without thruster system and (2) a thruster-assisted moored spar. Two horizontal, translational motions, i.e. surge and sway, are mainly emphasized since the thruster applications, in general, aim at the horizontal motion reduction.

However, it is also beneficial to evaluate what changes might occur in other motions when the thruster system is applied since a floating structure has coupling effects among

6DOF motions. Those motions as well as surge and sway must have different behavior when thrusters are applied depending on the commanded thruster forces and their locations. By this reason, the spectra of all 6DOF motions are shown in Figs. 7.13 through 7.18, and the statistical analysis results are summarized in Table 7.8. All motions were given at the center of the spar on the still water level rather than at the center of gravity.

According to the spectra, the *STD* values in LF (<0.2rad/s) of all motions except for yaw are reduced when the thrusters are applied, while WF *STD* values remain almost the same as expected. In surge and sway motion spectra (Figs. 7.13 and 7.14), only the surge motion has the WF components since the spar encounters the waves propagating due west so that a spar has little effect from the waves in sway direction.

Most interestingly, the thruster application benefits even heave, roll, and pitch motions so that it literally “assists” the spar to counter the environmental forces. The trajectories of the spar center at the mean water level are shown in Fig. 7.19.

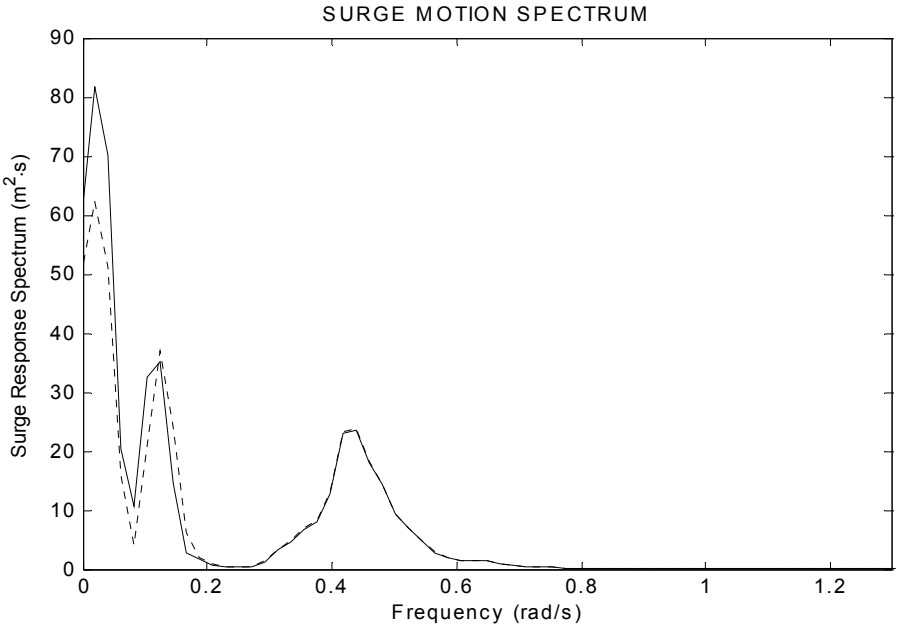

Fig. 7.13. Surge motion spectra:

(a) solid line – no thruster and (b) dotted line – with thruster.

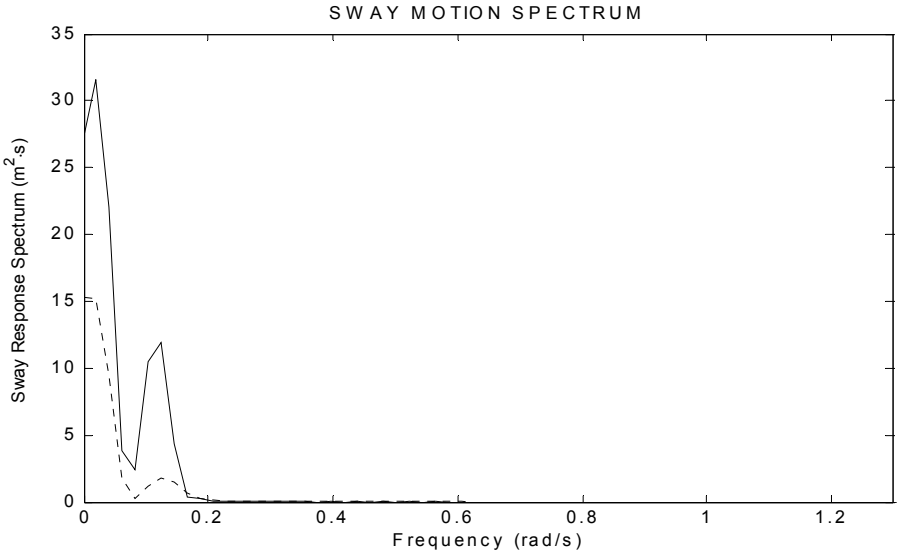

Fig. 7.14. Sway motion spectra:

(a) solid line – no thruster and (b) dotted line – with thruster.

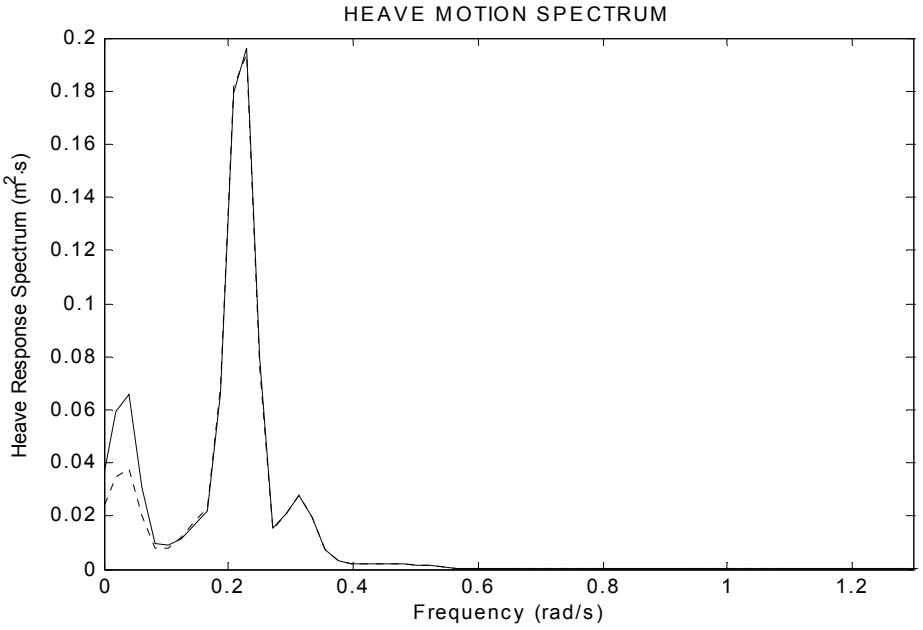

Fig. 7.15. Heave motion spectra:

(a) solid line – no thruster and (b) dotted line – with thruster.

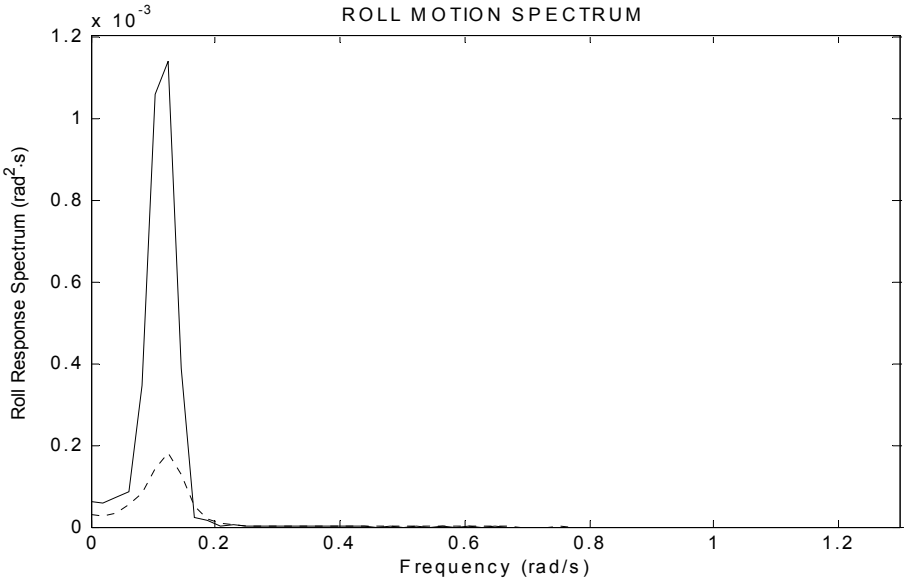

Fig. 7.16. Roll motion spectra:

(a) solid line – no thruster and (b) dotted line – with thruster.

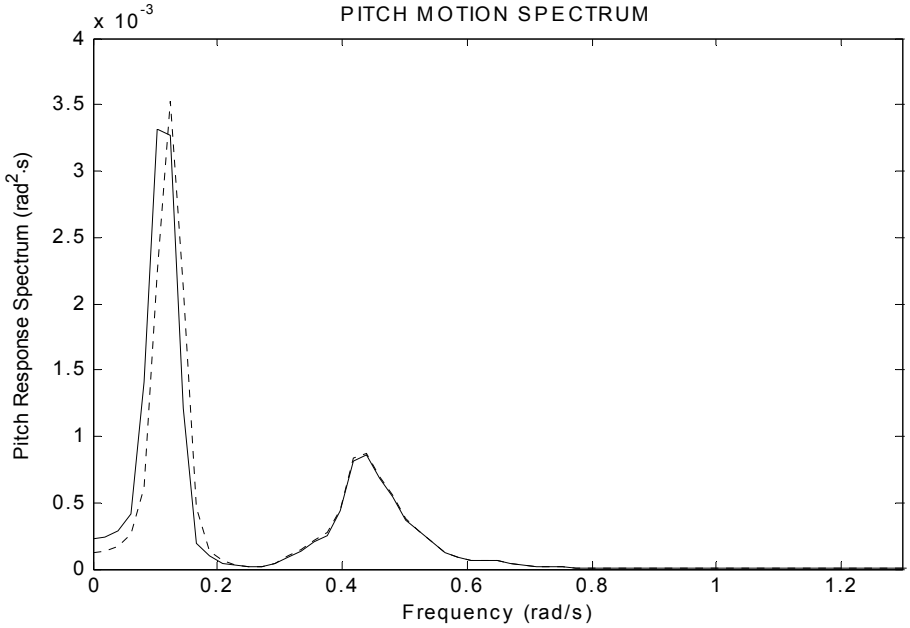

Fig. 7.17. Pitch motion spectra:
(a) solid line – no thruster and (b) dotted line – with thruster.

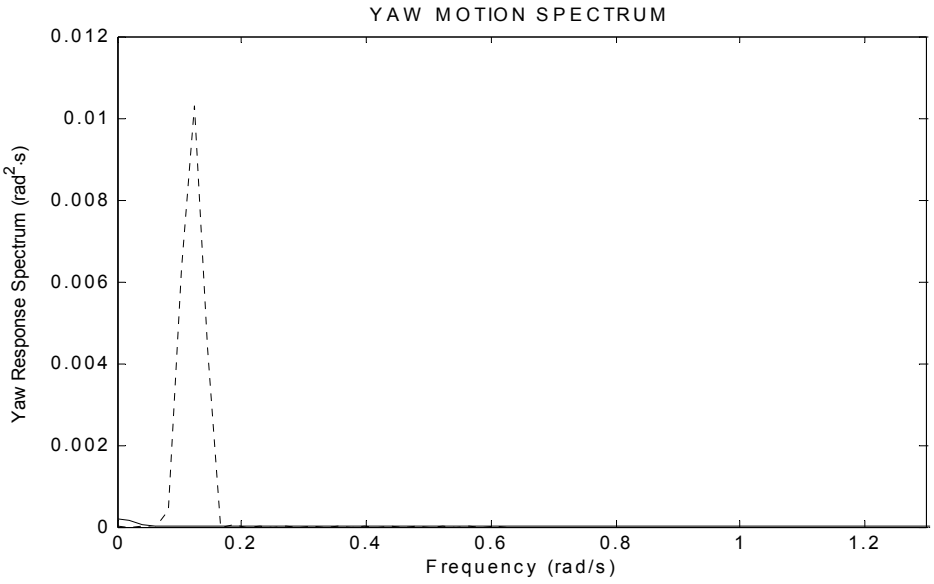

Fig. 7.18. Yaw motion spectra:
(a) solid line – no thruster and (b) dotted line – with thruster.

Table 7.8

Comparisons of Statistical Results of Spar Motions at the Local Origin (unit: meter, degree)

Motion	Thruster	Mean	LF *STD*	WF *STD*	Total *STD*	Extreme
Surge	Yes	-24.31	2.28	1.79	2.91	-36.69
	No	-26.28	2.50	1.78	3.08	-40.16
Sway	Yes	-4.70	0.91	0.06	0.92	-7.59
	No	-5.46	1.45	0.05	1.45	-10.53
Heave	Yes	-0.21	0.07	0.10	0.13	-0.72
	No	-0.24	0.08	0.10	0.14	-0.81
Roll	Yes	0.57	0.22	0.03	0.23	1.25
	No	0.73	0.47	0.03	0.47	2.12
Pitch	Yes	-1.82	0.82	0.63	1.03	-5.86
	No	-2.32	0.85	0.62	1.05	-6.91
Yaw	Yes	0.24	1.21	0.03	1.21	3.46
	No	-0.99	0.15	0.00	0.15	-1.47

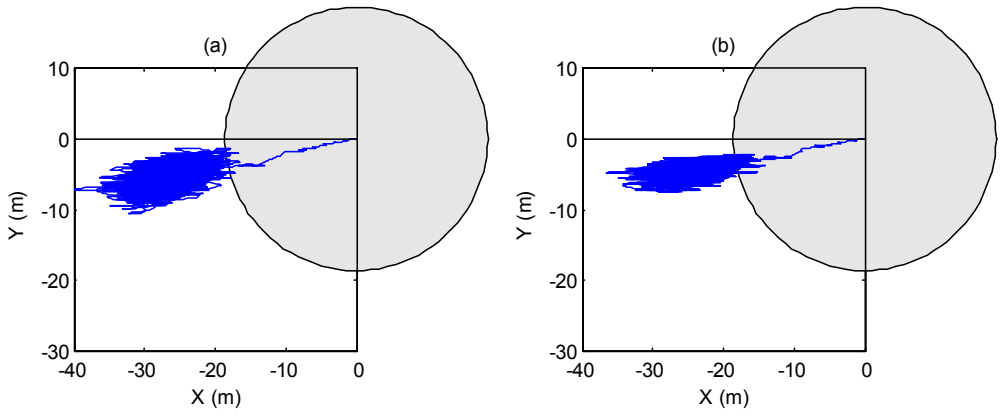

Fig. 7.19. Trajectories of spar at the mean water level. Gray circle represents the spar with correct scale. Trajectories (a) without thruster and (b) with thrusters.

The time series of all 6DOF motions for the cases with thruster and without are shown in Figs. 7.20 and 7.21.

Finally, to evaluate the top tension in mooring line/riser when thrusters are applied, statistical analysis is carried out and summarized in Table 7.9.

Table 7.9

Comparisons of Statistical Results of Mooring/Riser Top Tensions When the Spar Is Damaged (unit: kN)

	Thruster	Mean	Total *STD*	Max
Mooring Line	No	5066	590	8233
No. 1	Yes	4832	516	7592
Mooring Line	No	4987	557	7810
No. 2 (tension)	Yes	4741	468	7130
Mooring Line	No	4222	290	5631
No. 3	Yes	4087	236	5236
Mooring Line	No	3485	96	3821
No. 9 (slack)	Yes	3436	72	3698
Gas Export	No	887	0	888
Riser No. 19	Yes	887	0	888
Water Injection	No	1362	0	1362
Riser No. 26	Yes	1362	0	1362
Drilling Riser	No	3269	0	3270
No. 27	Yes	3269	0	3270
Production	No	2106	0	2106
Riser No. 29	Yes	2106	0	2106

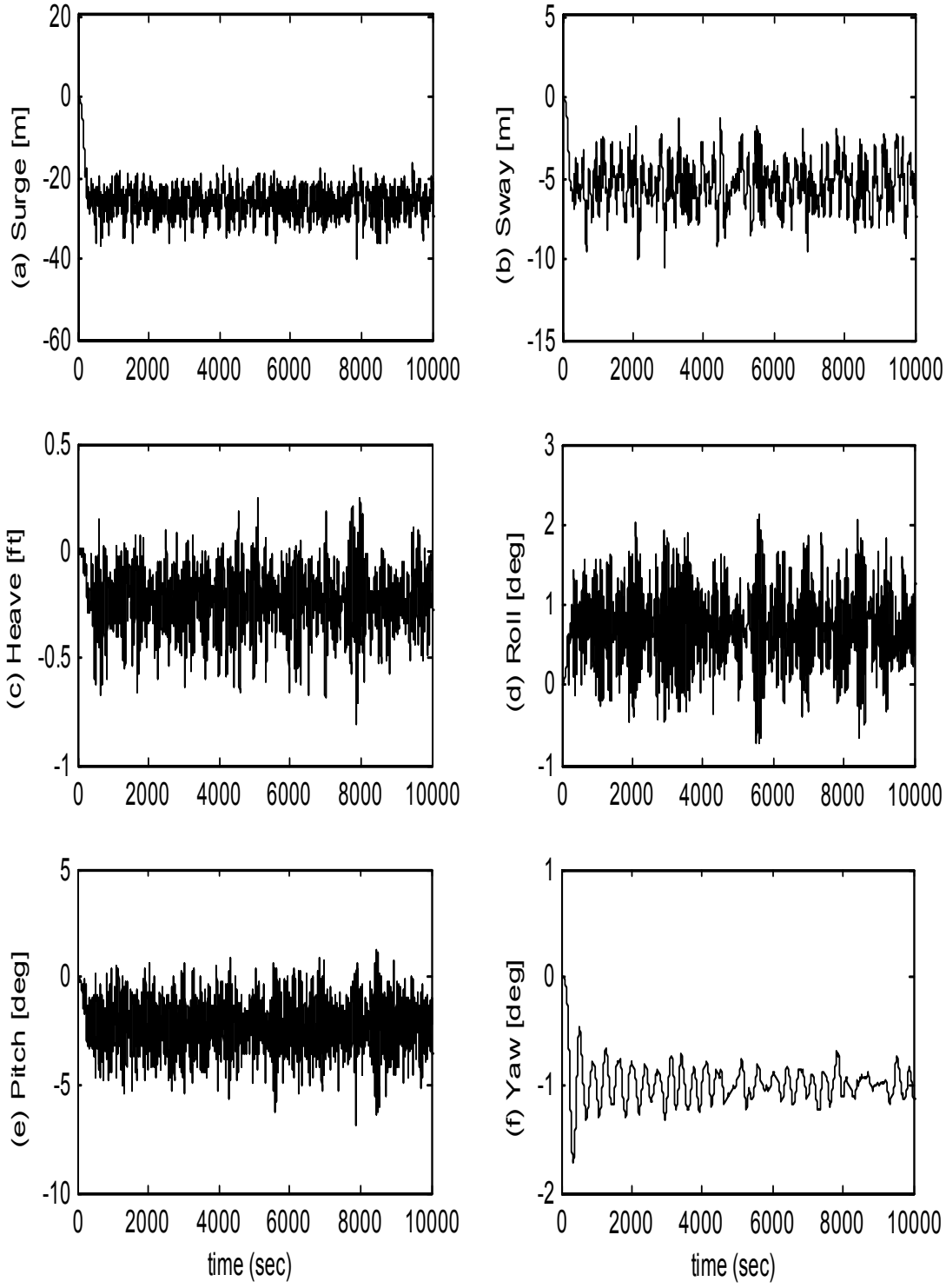

Fig. 7.20. Time series of all 6DOF motions spar center at the mean water level when there is no thruster assist.

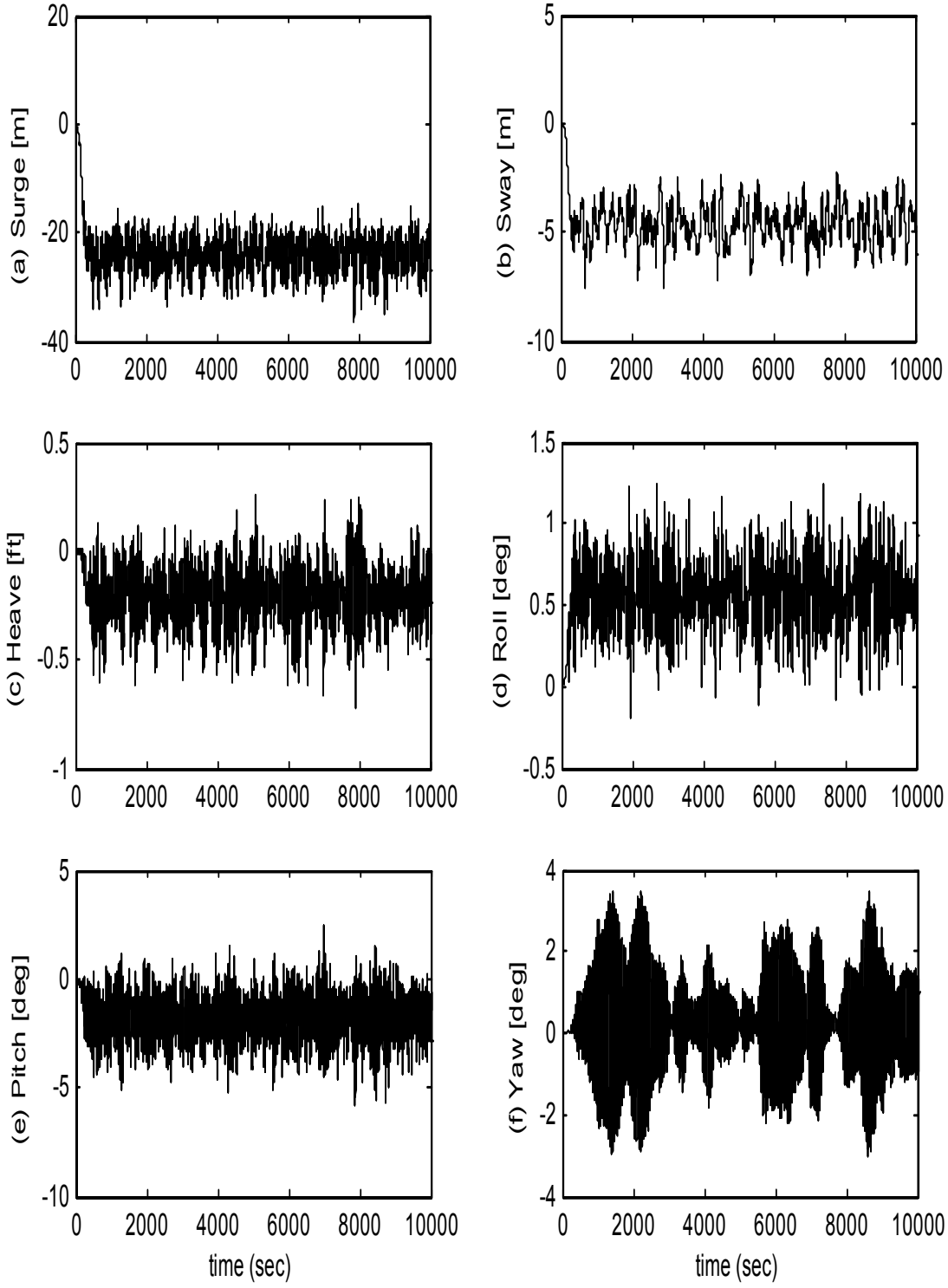

Fig. 7.21. Time series of all 6DOF motions spar center at the mean water level when the thruster forces are applied.

7.4.4. Case (2): Coupled vs. Uncoupled

As mentioned in previous Chapter V, as water depth becomes deeper, the uncoupled quasi-static analysis, which assumes that moorings/tendons and risers respond statically to the motion of the structure, may produce inaccurate results (Ma et al., 2000 and Arcandra, 2001). For DP and/or thruster-assisted POSMOOR systems, coupled analyses are more preferred since the appropriate required thruster forces can only be obtained at every time step by considering instant excursion of a platform. However, uncoupled motion analysis programs cannot capture the interactivity since their approach uses two-step procedure.

The environmental condition used in this case study is the same as the one used for case (1). In this analysis, the thruster forces were calculated and applied for the first step in the uncoupled analysis, and the motion of the platform was transferred to the second step to explore mooring/riser behaviors.

For the comparison between coupled and uncoupled analyses, the global motion of a spar is examined. The spectra of all 6DOF are shown in Figs. 7.22 through 7.27. It is clearly shown that an uncoupled motion analysis gives bigger values in all motions than a coupled analysis. Especially, it is found that the heave *RMS* response of the coupled analysis is significantly small compared to that of the uncoupled analysis.

According to the detailed statistical analysis results summarized in Table 7.10, the mean responses for both coupled and uncoupled analyses remain almost the same, but the coupled analysis provides less the LF *STD*s and extreme values than the uncoupled analysis.

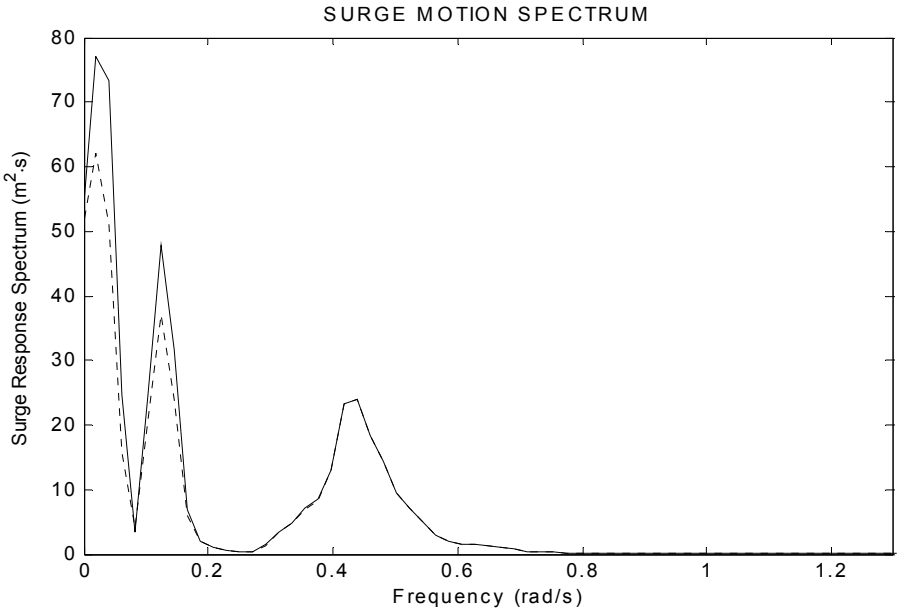

Fig. 7.22. Surge motion spectra:

(a) solid line – uncoupled, and (b) dotted line – coupled.

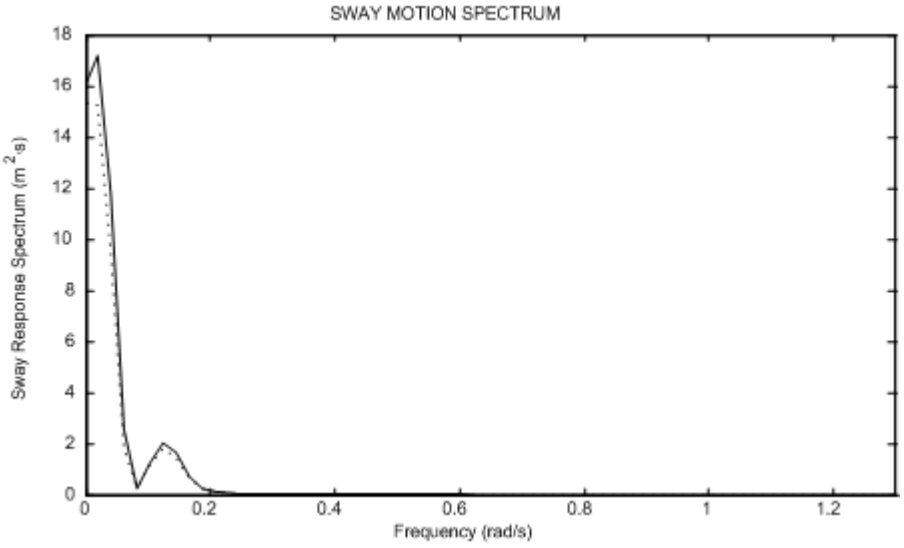

Fig. 7.23. Sway motion spectra:

(a) solid line – uncoupled and (b) dotted line – coupled.

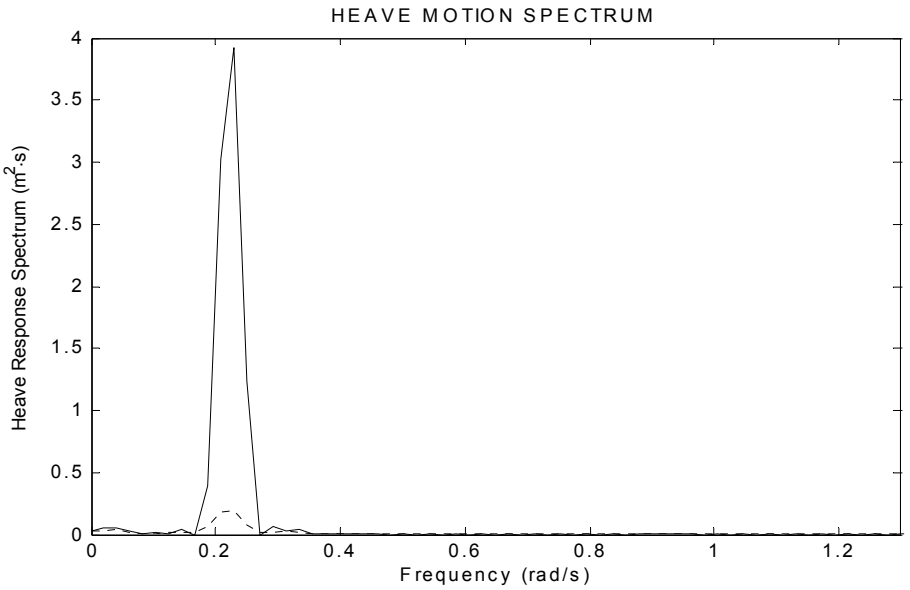

Fig. 7.24. Heave motion spectra:
(a) solid line – uncoupled and (b) dotted line – coupled.

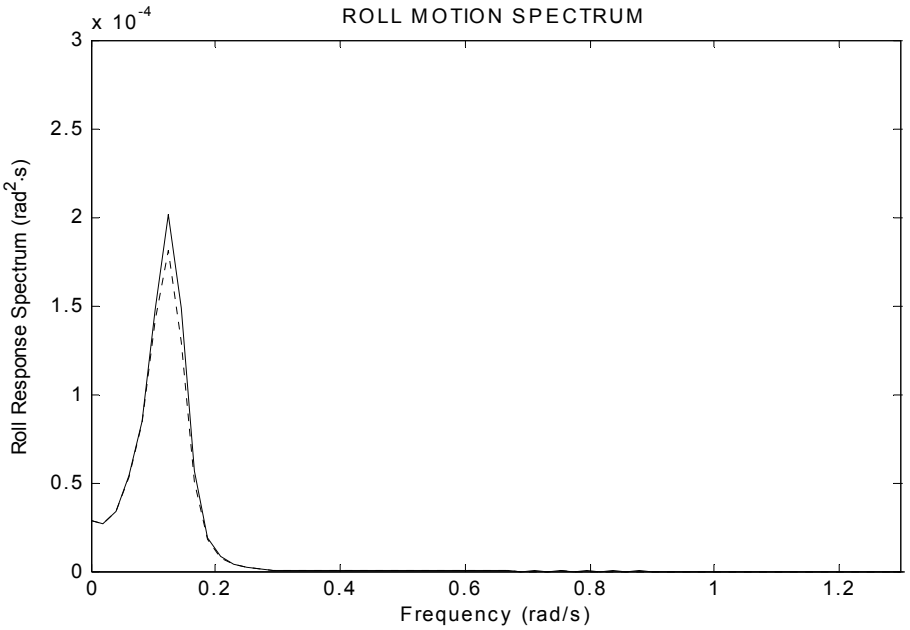

Fig. 7.25 Roll motion spectra:
(a) solid line – uncoupled and (b) dotted line – coupled.

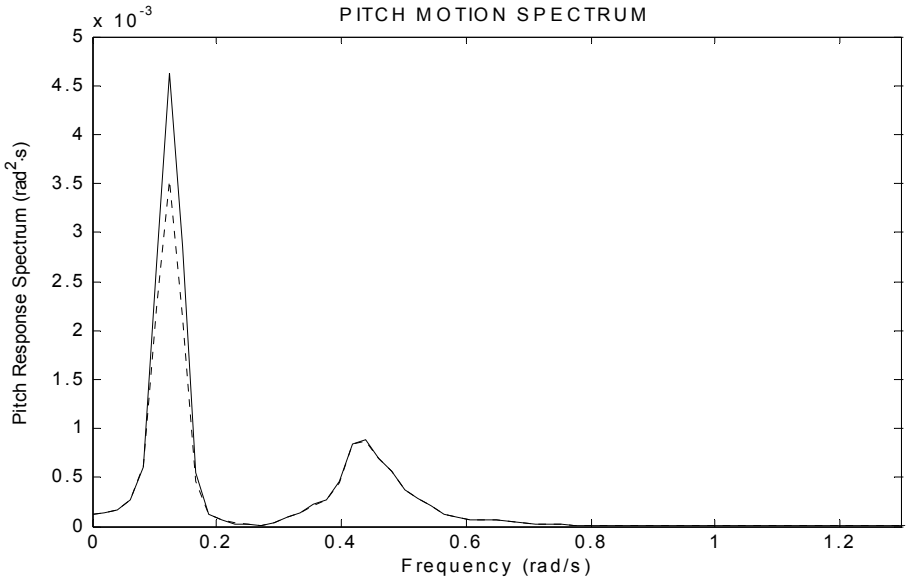

Fig. 7.26. Pitch motion spectra:
(a) solid line – uncoupled and (b) dotted line – coupled.

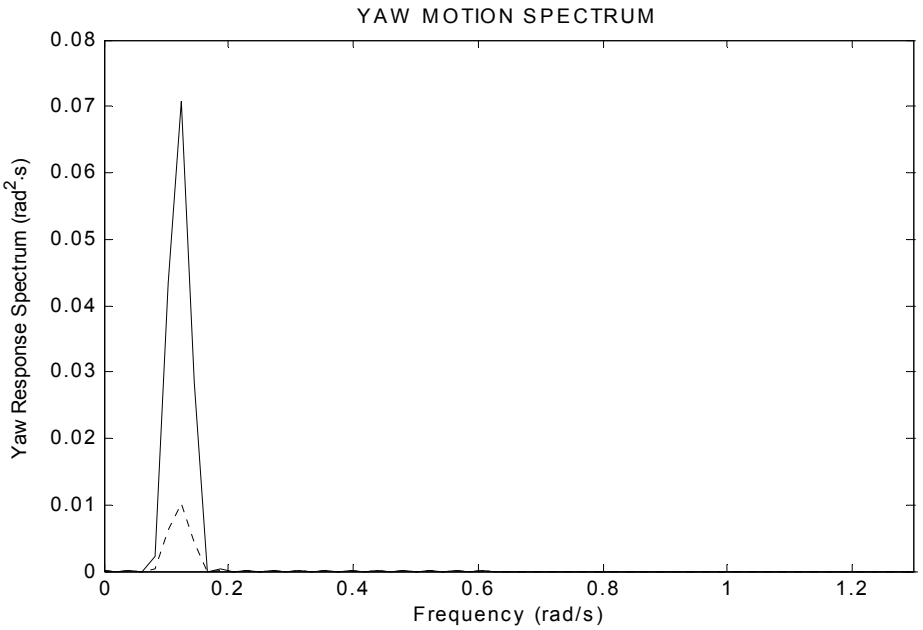

Fig. 7.27. Yaw motion spectra:
(a) solid line – uncoupled and (b) dotted line – coupled.

Table 7.10

Comparisons of Coupled and Uncoupled Analysis of Spar Motions When Thrusters Are Applied (unit: meter, degree)

Motion	Coupled	Mean	LF *STD*	WF *STD*	Total *STD*	Extreme
Surge	Yes	-24.31	2.28	1.79	2.91	-36.69
	No	-24.26	2.58	1.80	3.15	-37.40
Sway	Yes	-4.70	0.91	0.06	0.92	-7.59
	No	-4.72	0.98	0.06	0.98	-7.91
Heave	Yes	-0.21	0.07	0.10	0.13	-0.72
	No	-0.21	0.09	0.38	0.43	-1.28
Roll	Yes	0.57	0.22	0.03	0.23	1.25
	No	0.57	0.23	0.03	0.24	1.27
Pitch	Yes	-1.82	0.82	0.63	1.03	-5.86
	No	-1.83	0.91	0.63	1.11	-5.92
Yaw	Yes	0.24	1.21	0.03	1.21	3.46
	No	0.23	3.16	0.08	3.14	8.68

In summary, less motion responses were found in the results of a coupled analysis results. As shown in Table 7.11, the averages of the calculated thruster forces are almost the same, but an uncoupled analysis gives higher *STD* and extreme values, which means that the uncoupled analysis predicts more oscillatory behavior in thruster actions, so that the spar has more fluctuating responses correspondingly.

Table 7.11

Comparison of Commanded Thrust Obtained from Coupled and Uncoupled Analyses

	Thrust in Surge [kN]			Thrust in Sway [kN]		
	Mean	*STD*	Extreme	Mean	*STD*	Extreme
Coupled	1325	448	3091	446	495	2094
Uncouple	1322	521	3284	447	523	2125

7.4.5. Case (3): Evaluation of a Damaged Condition

To evaluate what would occur in spar motions and mooring/riser top tensions when one of the mooring lines breaks, three cases are systematically compared: (1) intact condition without thruster, (2) damaged condition (mooring line No. 1 broken) without thruster, and (3) the same damaged condition with thrusters. As shown in Figs. 7.28 and 7.33, the damaged condition without thruster has smaller *STD* than the intact condition since the total mooring stiffness is decreased. The mean and extreme values, of course, should be increased. However, the loss of one mooring line causes the station-keeping system (mooring in this case) to be less stiff.

The thruster-assist position-keeping system acts as a damper so that the spar motions become even less fluctuating. In deep seas, the mooring system would have less stiffness than shallow cases. Therefore, thrusters are aimed to act as an additional spring to reinforce the mooring stiffness. However, thrusters are not sufficiently capable of countering the 100-yr hurricane environment as mentioned in case (1). The 6DOF motion comparison is summarized in Table 7.12. Based on the comparison, it is noticeable that the extreme values of the case of a damaged spar with thrusters are placed in the middle of the other two cases, which are the intact case and the damaged case without thruster.

As shown in Table 7.12, most of global motions including the roll motion are improved. When a mooring line is broken, the thruster system is able to reduce the excursion of the spar hull, which must be related to a safety issue in terms of mooring/riser line tension reduction.

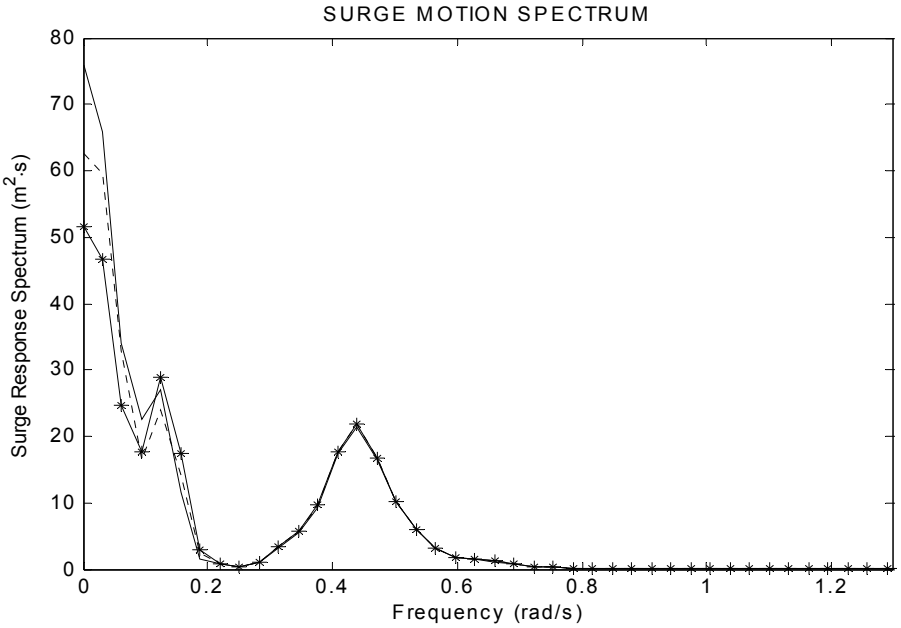

Fig. 7.28. Surge motion spectra of three different cases: (a) solid – intact, (b) dotted – damaged without thruster, and (c) * – damaged with thrusters.

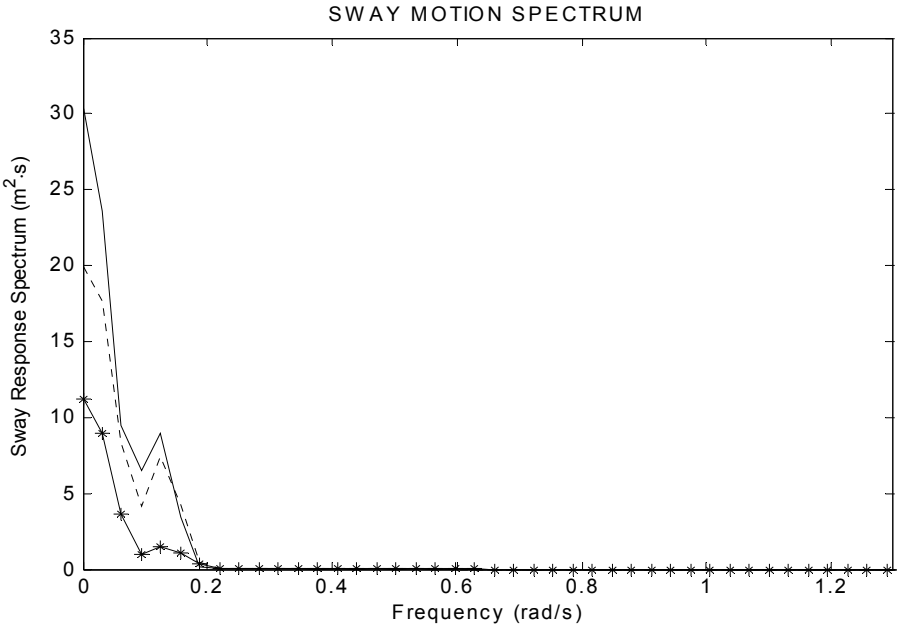

Fig. 7.29. Sway motion spectra of three different cases: (a) solid – intact, (b) dotted – damaged without thruster, and (c) * – damaged with thrusters.

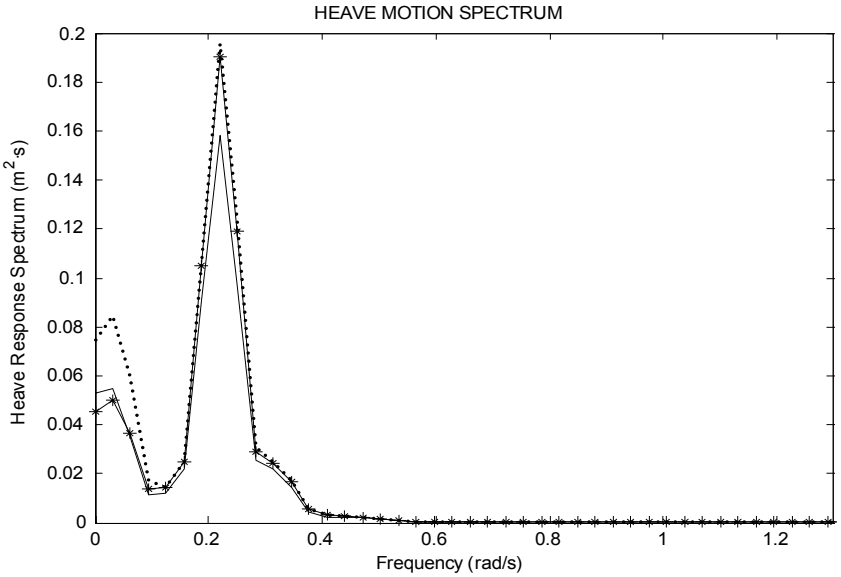

Fig. 7.30. Heave motion spectra of three different cases: (a) solid – intact, (b) dotted – damaged without thruster, and (c) * – damaged with thrusters.

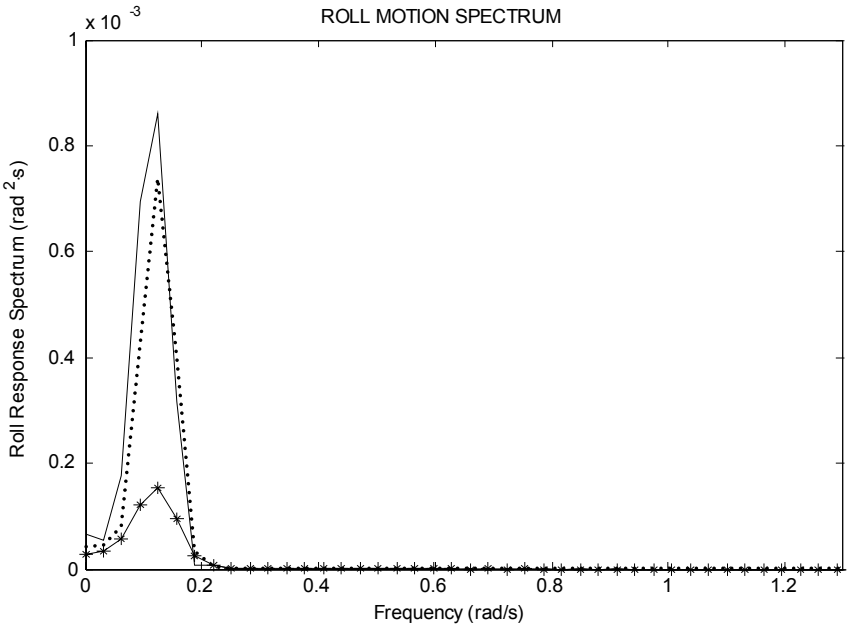

Fig. 7.31. Roll motion spectra of three different cases: (a) solid – intact, (b) dotted – damaged without thruster, and (c) * – damaged with thrusters.

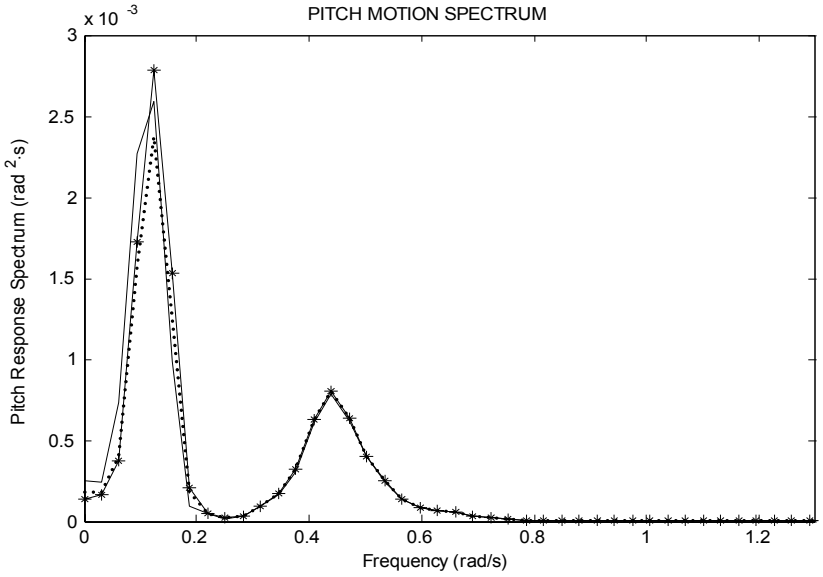

Fig. 7.32. Pitch motion spectra of three different cases: (a) solid – intact, (b) dotted – damaged without thruster, and (c) * – damaged with thrusters.

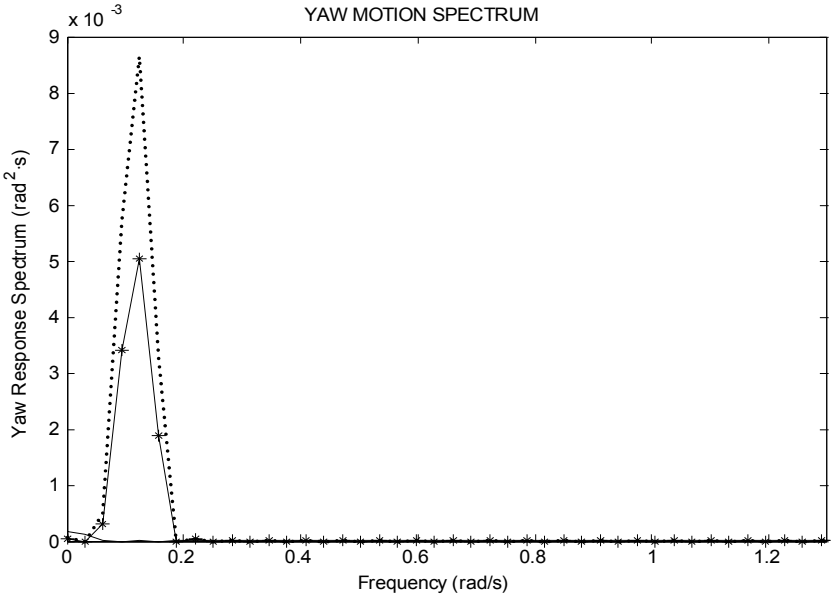

Fig. 7.33. Yaw motion spectra of three different cases: (a) solid – intact, (b) dotted – damaged without thruster, and (c) * – damaged with thrusters.

Table 7.12

Comparisons of Statistical Results of Spar Motions When Damaged (unit: meter, degree)

	Condition	Thruster	Mean	LF *STD*	WF *STD*	Total *STD*	Max
Surge	Intact	No	-26.28	2.50	1.78	3.08	-40.16
	Damaged	No	-32.93	2.38	1.79	2.99	-46.01
	Damaged	Yes	-31.28	2.26	1.80	2.90	-43.70
Sway	Intact	No	-5.46	1.45	0.05	1.45	-10.53
	Damaged	No	-4.35	1.28	0.06	1.28	-8.69
	Damaged	Yes	-4.05	8.33	0.06	0.84	-6.91
Heave	Intact	No	-0.24	0.08	0.10	0.14	-0.81
	Damaged	No	-0.13	0.09	0.11	0.15	-0.81
	Damaged	Yes	-0.07	0.08	0.11	0.14	-0.68
Roll	Intact	No	0.73	0.47	0.03	0.47	2.12
	Damaged	No	0.62	0.42	0.03	0.43	1.81
	Damaged	Yes	0.57	0.23	0.03	0.23	1.24
Pitch	Intact	No	-2.32	0.85	0.62	1.05	-6.91
	Damaged	No	-2.11	0.79	0.63	1.01	-6.18
	Damaged	Yes	-1.91	0.84	0.63	1.05	-5.90
Yaw	Intact	No	-0.99	0.15	0.00	0.15	-1.47
	Damaged	No	0.24	1.37	0.05	1.36	3.87
	Damaged	Yes	0.22	1.05	0.04	1.04	3.12

Mooring/riser top tensions are compared and summarized in Table 7.13. When thrusters are applied, the top tension of mooring line number 2 (most loaded) decreases by 11% compared to the damaged condition. All top tensions of the risers remain almost the same. Those vertical risers are not sensitive for the excursion of the spar hull. Of course, mooring line no. 9 does not have the tension decrease since the mooring is in the slack side.

Figs. 7.34 and 7.35 show the time series and spectra, respectively, of the top tension of mooring line 2 of three difference cases: (a) intact, (b) damaged without thruster, and (c)

damaged with thrusters.

Table 7.13

Comparisons of Statistical Results of Mooring/Riser Top Tensions When the Spar Is Damaged (unit: kN)

	Condition	Thruster	Mean	Total *STD*	Max
Mooring Line	Intact	No	5066	590	8233
No. 1 (broken)	Damaged	No	n/a	n/a	n/a
	Damaged	Yes	n/a	n/a	n/a
Mooring Line	Intact	No	4987	557	7810
No. 2 (tension)	Damaged	No	6727	907	10820
	Damaged	Yes	6241	745	9581
Mooring Line	Intact	No	4222	290	5631
No. 3	Damaged	No	4794	391	6767
	Damaged	Yes	4616	318	6180
Mooring Line	Intact	No	3485	96	3821
No. 9 (slack)	Damaged	No	2384	54	2610
	Damaged	Yes	2403	54	2619
Gas Export	Intact	No	887	0	888
Riser No. 19	Damaged	No	887	0	888
	Damaged	Yes	887	0	888
Water Injection	Intact	No	1362	0	1362
Riser No. 26	Damaged	No	1362	0	1363
	Damaged	Yes	1362	0	1362
Drilling Riser	Intact	No	3269	0	3270
No. 27	Damaged	No	3269	0	3270
	Damaged	Yes	3269	0	3270
Production	Intact	No	2106	0	2106
Riser No. 29	Damaged	No	2106	0	2107
	Damaged	Yes	2106	0	2107

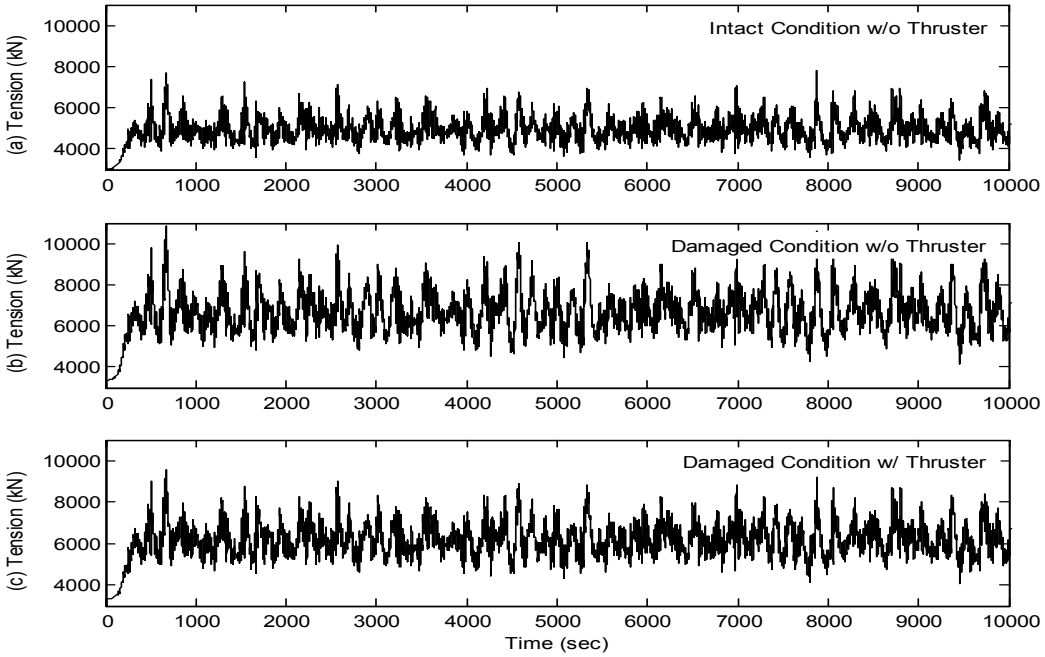

Fig. 7.34. Top tension comparison of mooring line 2 (most loaded) for three cases: (a) Intact, (b) damaged without thruster, and (c) damaged with thruster.

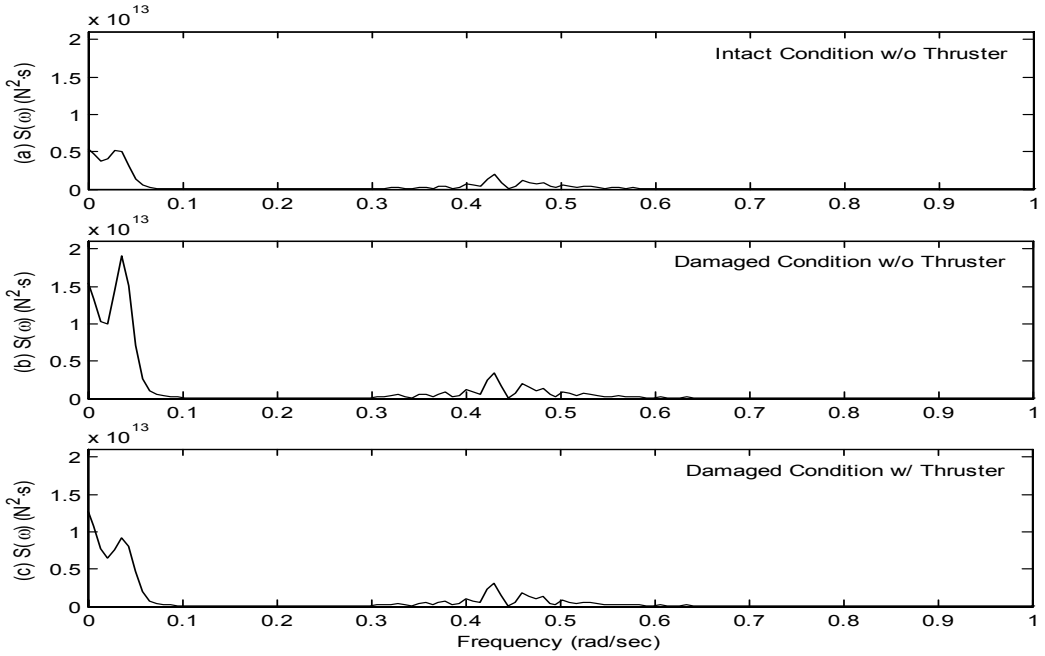

Fig. 7.35. Spectrum comparison of top tension of mooring line 2 (most loaded) for three cases: (a) Intact, (b) damaged without thruster, and (c) damaged with thruster.

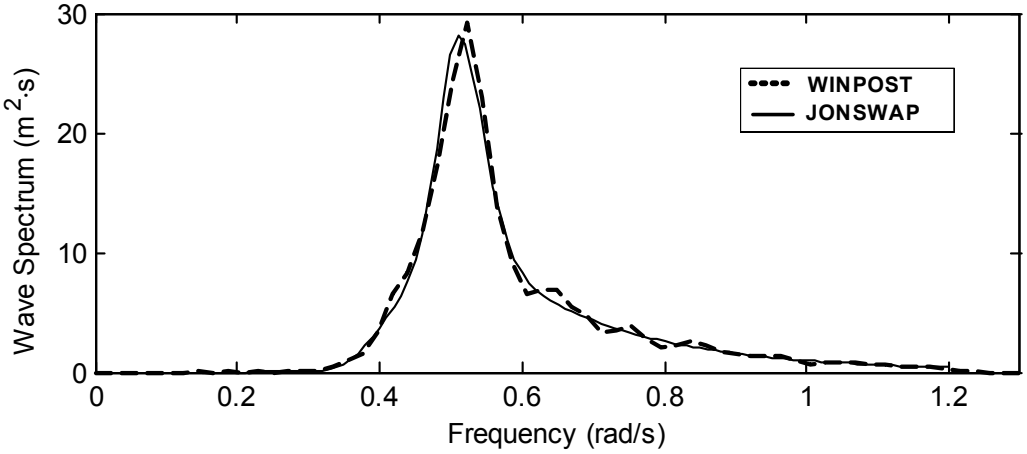

Fig. 7.36. Wave spectra from WINPOST simulation (dotted line) and JONSWAP (solid line) for 10-yr hurricane condition.

7.4.6. Case (4): Thruster Performance in 10-Year Hurricane Condition

Cortijo et al. (2003) suggested a DP FPSO for ultra deepwaters. 10-yr hurricane condition which is one of the environmental conditions used for the DP FPSO study was adopted, and it is summarized in Table 7.14. The wave spectra from WINPOST simulation and a JONSWAP are shown in Fig. 7.36 for verification of the wave generation. It is noted that the current and waves are collinear, and the surface current speed is almost the same. The significant wave height and wind speed are reduced. Fig. 7.37 shows all of those environmental forces in X-direction only, whose statistical analysis results are summarized in Table 7.15. All motion spectra are also shown in Figs. 7.38 through 7.43. The 10-yr hurricane condition is milder than 100-yr hurricane environment. Especially, wind and wave forces of 10-yr hurricane condition are relatively smaller than those of 100-yr hurricane as shown in Table 7.15.

Table 7.14

10-Yr Hurricane Condition in the GoM for Thruster-Assisted Moored Spar

Sea State	Hs [m]	Tp [s]	γ	μ_{waves} [deg]	Vw [m/s]	μ_{wind} [deg]	Vc [m/s]	μ_{cur} [deg]
10-Yr Hurr.	8.6	12.3	3.3	180	29.5	215	1.00	180

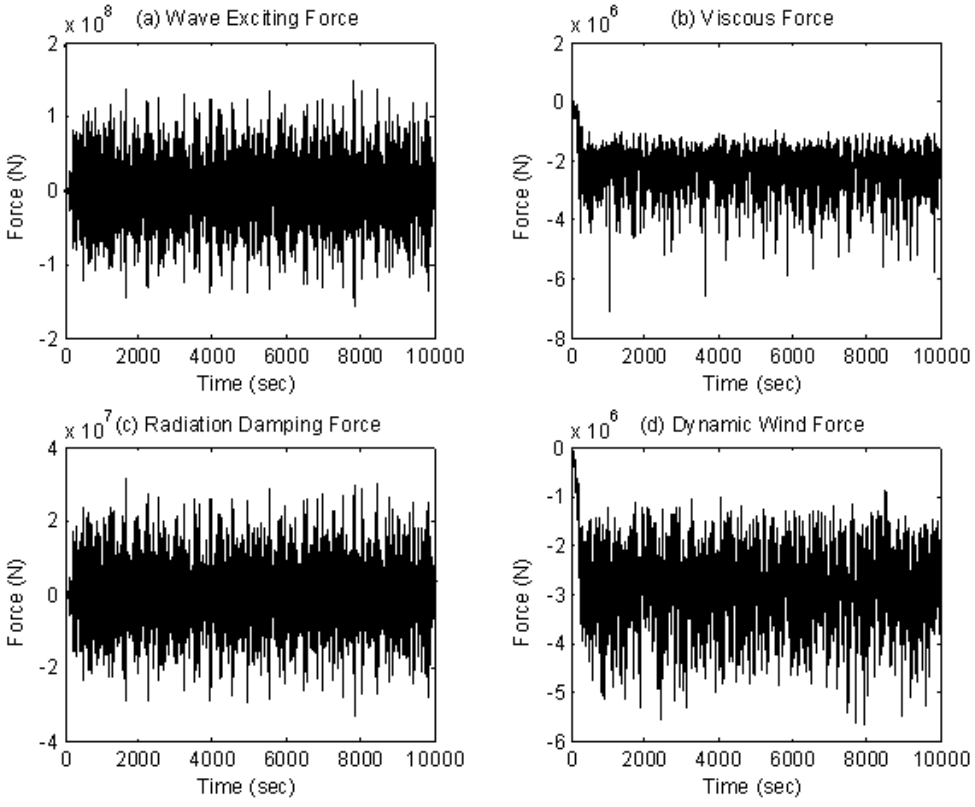

Fig. 7.37. Decomposed external forces in X-direction for 10-yr hurricane case: (a) wave exciting, (b) viscous, (c) radiation damping, and (d) dynamic wind forces.

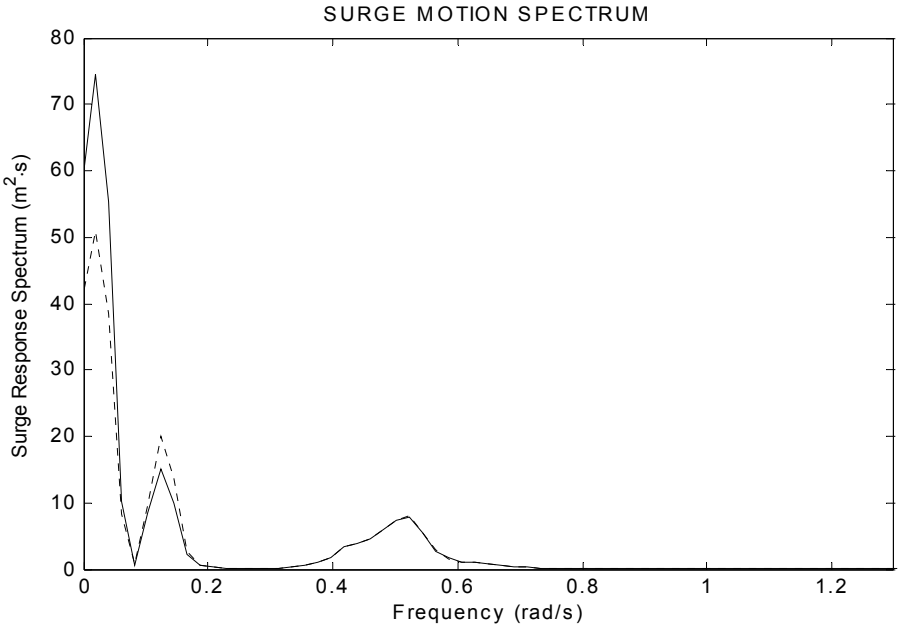

Fig. 7.38. Surge motion spectra for 10-yr hurricane case:
(a) solid – without thruster and (b) dotted – with thrusters.

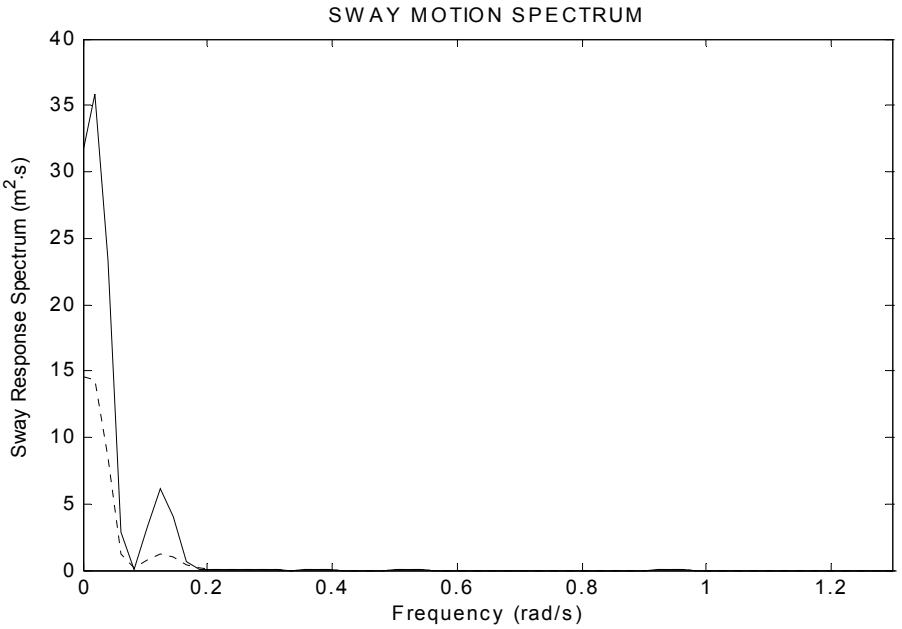

Fig. 7.39. Sway motion spectra for 10-yr hurricane case:
(a) solid – without thruster and (b) dotted – with thrusters.

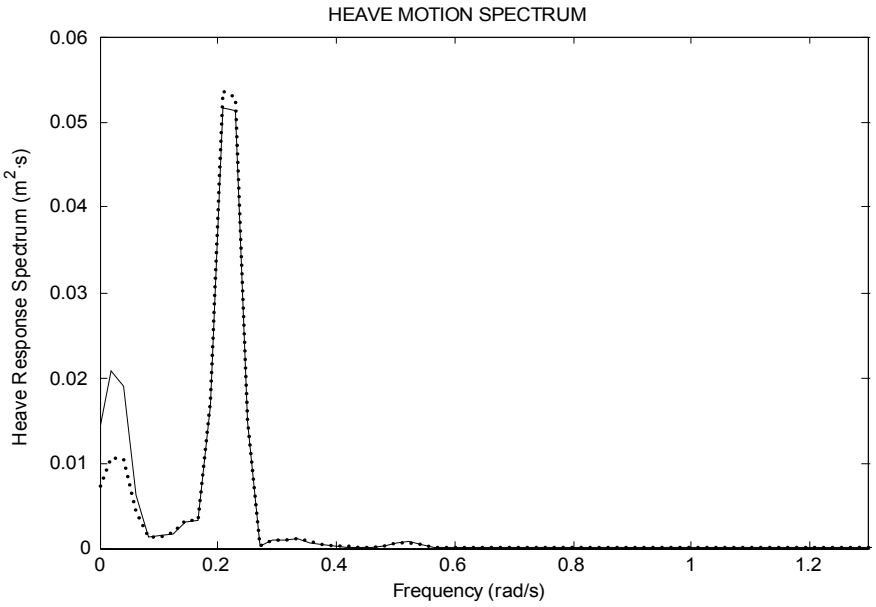

Fig. 7.40. Heave motion spectra for 10-yr hurricane case:
(a) solid – without thruster and (b) dotted – with thrusters.

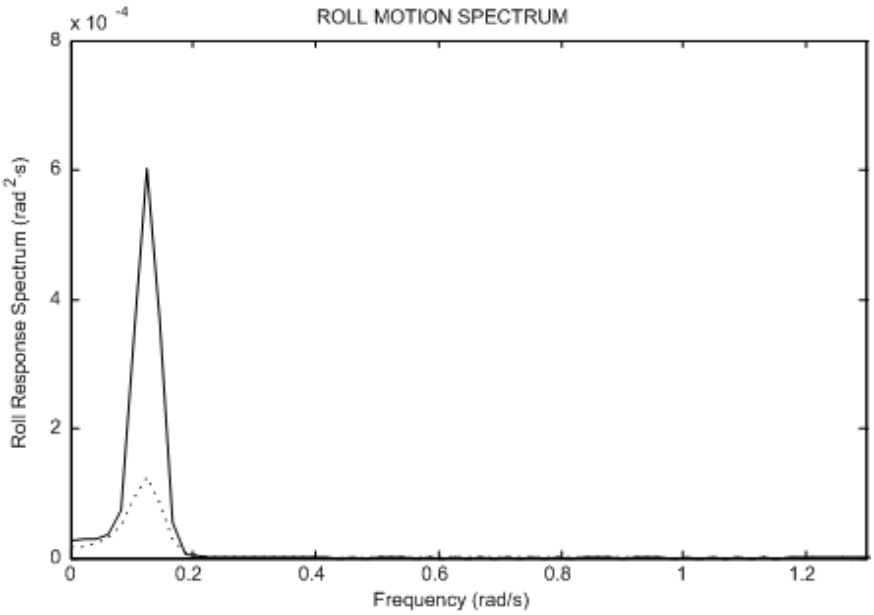

Fig. 7.41. Roll motion spectra for 10-yr hurricane case:

(a) solid – without thruster and (b) dotted – with thrusters.

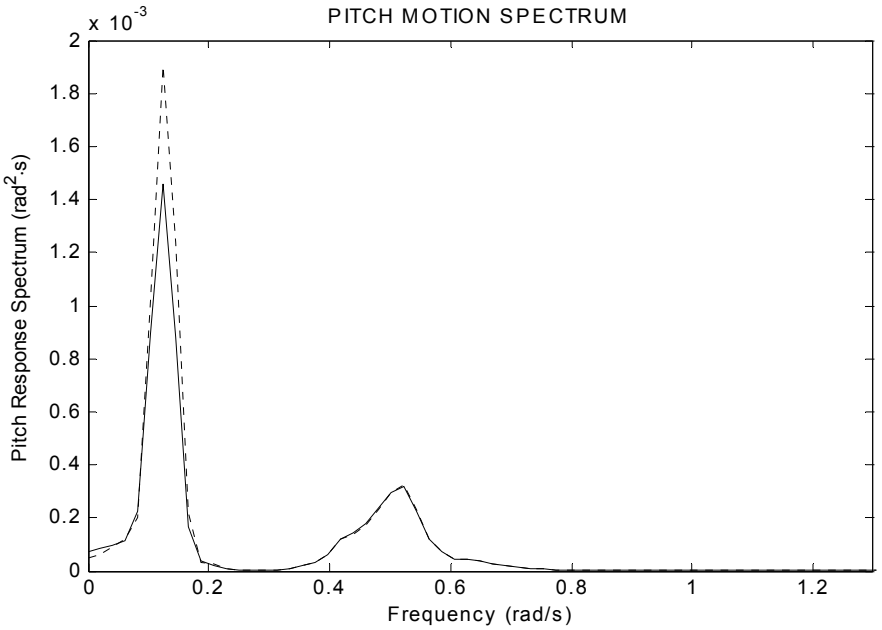

Fig. 7.42. Pitch motion spectra for 10-yr hurricane case:
(a) solid – without thruster and (b) dotted – with thrusters.

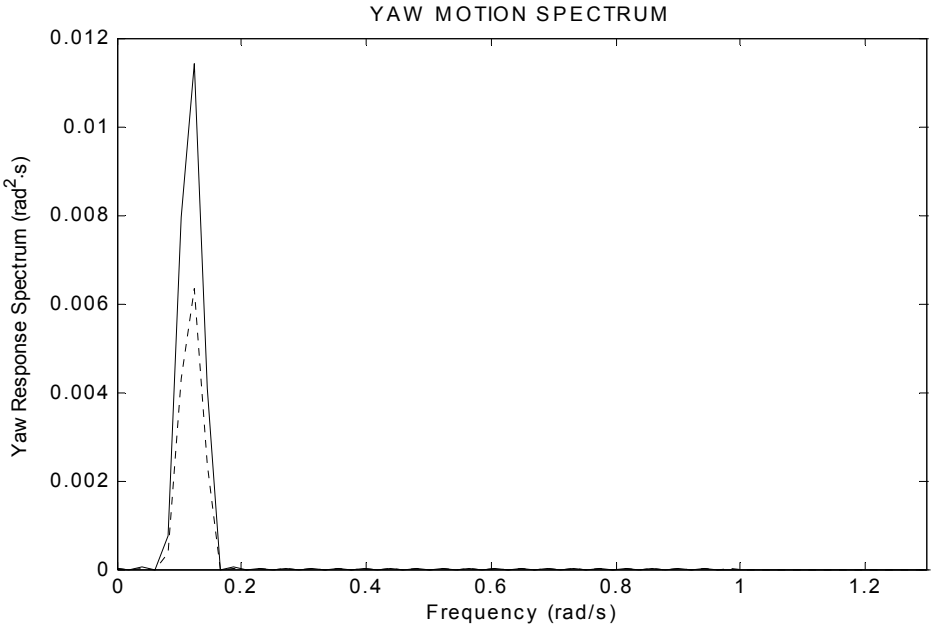

Fig. 7.43. Yaw motion spectra for 10-yr hurricane case:
(a) solid – without thruster and (b) dotted – with thrusters.

Table 7.15

Statistical Results of External Forces Acting on Spar without Thruster for 10-Yr Hurricane in GoM (unit: kN)

	X			**Y**		
Force	Mean	*STD*	Extreme	Mean	*STD*	Extreme
Wave Exciting	-398	42200	-156000	0	0	0
Viscous	-2130	544	-7120	1090	141	1930
Radiation Damping	0	9010	-33100	0	172	-666
Dynamic Wind	-2840	712	-5650	-1990	499	-3950

Even in this milder condition than a 100-yr hurricane condition, it is found that the excursion of the spar platform does not significantly change. Statistical analysis of the spar platform motion is summarized in Table 7.16. The trajectories of the spar center in 10-yr hurricane condition are shown in Fig. 7.44.

In general, a 10-yr DP operational condition is used for the motion analysis of offshore vessels with a thruster system.

Table 7.16

Comparisons of Statistical Results of Spar Motions for 10-Yr Hurricane Condition in the GoM (unit: meter, degree)

	Thruster	Mean	LF *STD*	WF *STD*	Total *STD*	Max
Surge	Yes	-17.63	1.87	1.05	2.14	-25.81
	No	-18.98	2.08	1.05	2.33	-27.79
Sway	Yes	-3.03	0.85	0.04	0.86	-5.67
	No	-3.46	1.39	0.04	1.39	-7.94
Heave	Yes	-0.10	0.03	0.05	0.06	-0.33
	No	-0.12	0.04	0.05	0.06	-0.36
Roll	Yes	0.38	0.18	0.02	0.18	0.98
	No	0.41	0.33	0.02	0.33	1.32
Pitch	Yes	-1.16	0.58	0.38	0.70	-3.82
	No	-1.28	0.52	0.38	0.65	-3.99
Yaw	Yes	0.13	0.96	0.03	0.95	2.90
	No	0.14	1.29	0.04	1.28	3.63

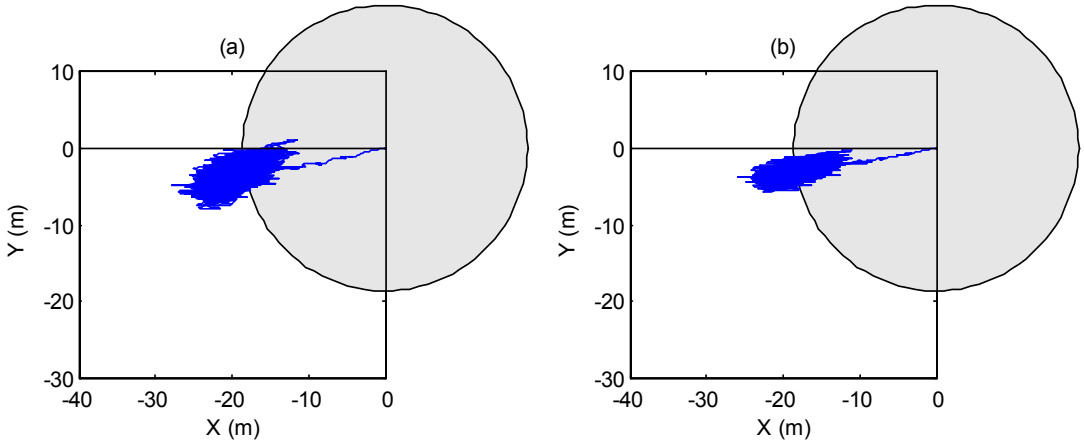

Fig. 7.44. Trajectories of spar center in 10-yr hurricane condition. Gray circle represents the spar with correct scale. Cases (a) without thruster and (b) with.

7.4.7. Case (5): Increase of Thruster Contribution

In the previous simulations, the spar motions were measured with respect to the mean water level. However, in spar motions, surge-pitch and sway-roll coupling effects are significant. For motion comparisons, the CG (Center of Gravity) would be better than the mean water level as a reference point. To investigate global motion changes, the reference point and the PD gains were changed. Comparisons of statistical results of spar motions at the mean water level with low PD gains are summarized in Table 7.17, while those comparisons at the CG of the spar with high PD gains are summarized in Table 7.18. Even mean values are different for the two no-thruster cases because of the surge-pitch and sway-roll coupling effects.

Table 7.17

Comparisons of Statistical Results of Spar Motions at the Mean Water Level for 100-Yr Hurricane Condition in the GoM with Low PD Gains (unit: meter, degree)

Motion	Thruster	Mean	LF *STD*	WF *STD*	Total *STD*	Extreme
Surge	Yes	-24.31	2.28	1.79	2.91	-36.69
	No	-26.28	2.50	1.78	3.08	-40.16
Sway	Yes	-4.70	0.91	0.06	0.92	-7.59
	No	-5.46	1.45	0.05	1.45	-10.53

Table 7.18

Comparisons of Statistical Results of Spar Motions at the Center of Gravity for 100-Yr Hurricane Condition in the GoM with High PD Gains (unit: meter, degree)

Motion	Thruster	Mean	LF *STD*	WF *STD*	Total *STD*	Extreme
Surge	Yes	-16.93	1.48	0.61	1.60	-21.76
	No	-21.88	1.91	0.61	2.01	-28.05
Sway	Yes	-2.57	0.56	0.01	0.56	-4.26
	No	-4.08	1.17	0.01	1.17	-7.67

7.5. Concluding Remarks

The fully coupled hull/mooring/riser time-domain dynamic analysis program gives smaller motion responses than an uncoupled analysis. The change in environmental conditions may not affect the relative contribution of the thruster-assisted system unless both the mooring line stiffness and P gains remain the same. As shown in Table 7.18, the thrusters with higher PD gains perform better than lower PD gains. However, the PD gains should be designed based on the surge and sway static offset curves.

Typical sea states, wind speeds, and surface current speeds for the GoM and the North Sea according to DNV (2001) are given in Table 7.19. Environmental loads applied in mooring calculations are normally based on wind and wave conditions with a 100-yr return period, applied together with a current 10-year return period (Meyer and Huglen, 2003).

However, for a moored spar case, the current force becomes larger compared to the FPSO case due to the relative deep draft compared to other offshore structures. Therefore, large viscous force driven by current (or even loop current) needs to be properly considered when thruster applications for a spar are considered.

Thrusters are useful for two cases: (a) when fatigue loads are important, and (b) when better safety is concerned for damaged conditions. The spar would have better performance in global motions with smaller STDs, which provide less cyclic stresses to the spar mooring/riser system. In addition, the thrusters reduce the top tension of the most loaded mooring line by 11% in one of the cases mentioned above.

Table 7.19

Typical Environmental Condition for the GoM and the North Sea

Environment	GoM (Hurricane)	Norwegian Sea (Haltenbanken)	Northern North Sea (Troll Field)	North Sea (Ekofisk Area)
Max. H_s 100-year	11.9 m	16.5 m	15.0 m	14.0 m
Wave Period T_P	14.2 s	17.0-19.0 s	15.5-17.5 s	15.0-17.0 s
Wind Speed 1hr 10m 100-year	44.1 m/s	37.0 m/s	40.5 m/s	34.0 m/s
Surface Current Speed 10-year	1.98 m/s	0.90 m/s	1.50 m/s	0.55 m/s

CHAPTER VIII

SUMMARY, CONCLUSIONS, AND FUTURE WORK

8.1. Summary

Thruster control algorithm was developed, and Kalman filter performance was reviewed based on spectral analysis. Each PD gain was tuned based on optimization of cost function. Two case studies were conducted, and the simulation results confirmed two proposed hypotheses: (1) reduction of radii of watch circle of an FPSO and a spar and (2) reduction of top tensions of riser/mooring line. To test the two hypotheses, the following cases are investigated: (1) w/o thruster vs. w/, (2) coupled vs. uncoupled, and (3) intact, damaged w/o thruster, damaged w/.

The coupled full 6DOF motion analysis was conducted rather than just horizontal-plane responses (surge, sway, and yaw). To investigate global motion responses, spectral and statistical analysis were conducted.

A coupled dynamic analysis of thruster-assisted moored platforms was discussed. As oil/gas fields become depleted, ocean engineers are turning their attention to fields in ultra deep seas. Through the systematic case studies for the deepwater development in the GoM, two concepts were proposed and evaluated: (1) a thruster-assisted turret-moored FPSO and (2) a thruster-assisted spar.

Two key conclusions that we may draw from this study are: (1) Thruster-assisted moored systems may be a viable, feasible solution for the challenging issue of platform

operation in ultra deep seas, (2) The coupled analysis gives smaller motion responses than the uncoupled analysis since the hull-leg coupling effect is considered in the coupled analysis.

Following are the detailed conclusions drawn from each study case in Chapters VI and VII. Finally, suggested future work is discussed at the end of this chapter.

8.2. Thruster-Assisted Turret-Moored FPSO

As ocean oil fields become depleted, new feasible solutions for ultra deep sea exploration and drilling have been suggested. Deeper water conditions create challenges such as the increase of mooring line stress, effective means of position-keeping, reliable mooring/riser analysis methodology accompanied with the increase of the mooring/riser length, etc.

A thruster-assisted turret-moored FPSO, one of the promising solutions, was used for the study of the coupled dynamic analysis of thruster-assisted moored offshore platforms. To develop the analysis tool called WINPOST-FPSO-DP, Kalman filtering and control algorithms were considered. For numerical simulations, the 100-yr hurricane condition with non-parallel wind, wave, and current was applied. Even if the design condition is used for the simulation, the extreme values of the responses and mooring line/riser top tensions of the thruster-assisted FPSO in time domain analysis are considerably less than those in the case without thrusters.

From the evaluation of the numerical simulation results the following conclusions may be drawn:

- Position and velocity estimates were obtained with the use of the Kalman filtering.
- Judging from the power spectra of the applied thruster forces, the thrusters counter only the slowly-varying environmental forces.
- The thrusters may not be targeted to resist 100-yr hurricane case or even 10-yr hurricane condition. However, they are beneficial in the reduction of the extreme motion responses since the low frequency STD values can be decreased by the thruster assist.
- The thruster application generates such unnecessary rotational motions as roll and pitch. In this regard, the thruster depth effect needs to be properly considered.
- The mooring line stiffness of a deepwater offshore platform may be milder than that of a platform in shallow water. Therefore, thrusters can mainly be used as an additional spring to reinforce the mooring stiffness as well as a damper to reduce the STD. Thus, the mean values of platform motions can be reduced due to the hardened stiffness with the thruster assist, and the extreme values can also be reduced by the damping effect generated from the thrusters. With the same reasoning, for shallow water applications of thruster-assist system, the damping aspect of a thruster could be primarily emphasized for the purpose of position keeping of a floating structure.
- If the PD gains are appropriately tuned based on how much environmental forces need to be considered and what static offset curves we have, the P gains can be properly adjusted to improve the global motions of an FPSO.

8.2. Thruster Application for a Spar

Because of not fullly understood phenomena, such as wave-current interaction, viscous effect, and vortex induced motion, an offshore structure would encounter more serious structural stress than the expected values when the structure is designed. A spar is an example of this issue. It has been reported that a spar would move beyond the expected response limitation given based on the design and calculations. Even though several solutions could be suggested for the problem, enhancement of the global performance of a spar by means of assisting thrusters is considered in this study case. Study cases include: 1) intact condition in 100-yr hurricane condition with non-parallel wind and current, 2) coupled vs. coupled analyses, 3) failure condition with a broken mooring line, 4) 10-year hurricane condition with non-parallel wind, and 5) increase of thruster contribution. Based on the above case studies, the following conclusions are made:

- Position-keeping control law of a spar for the horizontal plane needs to be extended to roll and pitch damping since the spar has a small water-plane-area, resulting in relatively small restoring moments compared to other offshore platforms such as an FPSO. Thus, spar has unnecessary large roll and pitch oscillations by the thruster actions.
- An uncoupled analysis would give larger motion responses since it cannot capture the additional damping effect generated by the riser/mooring line.
- For design conditions, most external forces acting on the spar would have the similar order of forces.

- For a damaged condition (in case of mooring line No. 1 broken), the surge motion increases as expected, on the other hand the sway motion decreases. The broken mooring line is parallel to the X-axis, so geometrically it is not designed to resist the sway motion. In addition, extra mooring line stress caused by the line break would be concentrated in X-direction. Also, when surge mean position becomes larger, the positioning function in Y-direction becomes tighter due to the increase of the offset in Y-direction.
- Mooring line break could mean that the stiffness of the mooring lines becomes weaker.
- Due to the deep draft and super structure of a spar platform the slowly-varying mean drift current and wind force have the similar order of force. The mean drift wave exciting force is also dominant. In an FPSO case, only wave and wind forces are dominant since she has a small draft compared to a spar so that the viscous force effect becomes smaller. Therefore, for the design condition the weathervaning is targeted to reduce the wind force.

8.3. Future Work

Thruster modeling and power specification, and auto-tuning of PID gains, roll and pitch control may need to be considered in future studies. More sophisticated analysis of the interactions between the thrusters and hull motions may give different response results. Reduction of vortex induced motion with thruster assist can also be an important topic for the improvement of spar global motions.

REFERENCES

Aalbers, A. B., Janse, S. A. W., and Boom, W. C., 1995. DP assisted and passive mooring for FPSO's. Offshore Technology Conference, OTC 7722, Houston, USA, pp. 281-288.

API RP-2A WSD, 1994. Recommended practice for planning, designing and constructing fixed offshore platforms-working stress design. American Petroleum Institute, pp. 23.

Arcandra, T., 2001. Hull/mooring/riser coupled dynamic analysis of a deepwater floating platform with polyester lines. Ph.D. Dissertation, Texas A&M University, College Station, TX.

Arcandra, T., Nurtjahyo, P., and Kim, M. H., 2001. Hull/mooring/riser coupled analysis of a turret-moored FPSO 6000ft: Comparison between polyester and buoys-steel mooring lines. The 11th Offshore Symposium, The Texas Section of SNAME, Houston, Texas.

Balchen, J., Jenssen, N., Mathisen, E., and Saelid, S., 1980. A dynamic positioning system based on Kalman filtering and optimal control. Modeling, Identification and Control, pp. 135-163.

Barltrop, N. D. P., 1998. Floating Structures: A Guide for Design and Analysis. The Center for Marine and Petroleum Technology, vol. 2, chapter 10.

Cortijo, J. L., Duggal, A. S., Dijk, R., and Matos, S., 2003. DP FPSO – A fully dynamically positioned FPSO for ultra deep waters. Proceedings of ISOPE 2003, Honolulu, Hawaii, USA, May 25-30, pp. 194-202.

Det Norske Veritas (DNV), 2001. Comparative risk analysis for deepwater production systems prepared for Minerals Management Service (MMS).

Douglas-Westwood & Infield Systems, The World Floating Production Report 2003-2007.

Faltinsen, O. M., 1990. Sea loads on ships and offshore structures. Cambridge University Press, Cambridge, UK, pp. 23-31.

Ferziger, J. H., 1981. Numerical Methods for Engineering Application. John Wiley & Sons, Inc., pp. 84-92.

Fossen, T. I., 1994. Guidance and Control of Ocean Vehicles, John Wiley & Sons Ltd.

Fung, P. T., and Grimble, M. J., 1983. Dynamic ship positioning using a self-tuning Kalman filter. IEEE Transaction on Automatic Control, vol. AC-28, No. 3, pp. 339-350.

Garret, D. L., 1982. Dynamic analysis of slender rods. Journal Energy Resources Technology, vol. 104, pp. 302-307.

Kamphuis, J. W., 2000. Introduction to coastal engineering and management. Advanced Series on Ocean Engineering, vol. 16, World Scientific, pp. 79-80.

Kim, M. H., 1997. WINTCOL/WINPOST User's Manual. Ocean Engineering Program, Civil Engineering Department, Texas A&M University, College Station, TX.

Kim, Y. B., and Kim, M. H., 2002. Hull/mooring/riser coupled dynamic analysis of a tanker-based turret-moored FPSO in deep water. Proceedings of International Offshore and Polar Engineering Conference, Kyushu, Japan.

Kim, M. H., and Yue, D. K. P., 1990. The complete second-order diffraction solution for an axisymmetric body: Part 2. Bichromatic incident waves and body motions. Journal of Fluid Mechanics, vol. 211, pp. 557-593.

Kim, M. H., Kim, Y. B., Mercier, R., and Ward, S., 2003. Hull/mooring/riser coupled dynamic analysis of a turret-moored FPSO compared with OTRC experiment. Proceedings of International Symposium on Deepwater Mooring Systems: Concepts, Design, Analysis and Materials, Houston, Texas, pp. 239-254.

Kim, M. H., Ran, Z., and Zheng, W., 1999. Hull/mooring coupled dynamic analysis of a truss spar in time domain. Proceedings of International Offshore and Polar Engineering Conference, Brest, France.

Kim, M. H., Roesset, J. M., and Zhang, J., 1997. Nonlinear dynamic analysis methods for spar platforms. Proceedings of the Society of Naval Architects and Marine Engineers Conference (Gulf Section), Houston.

Kim, M. H., Tahar, A., and Kim, Y. B., 2001a. Variability of spar motion analysis against various design methodologies/parameters. Proceedings of the 20th Offshore Mechanics and Arctic Engineering, (OMAE), vol. 1, pp. 153-152.

Kim, M. H., Tahar, A., and Kim, Y. B., 2001b. Variability of TLP motion analysis against various design methodologies/parameters. Proceedings of the 11th International Offshore and Polar Engineering Conference, Stavanger, vol. 1, pp. 467-473.

Koo, B. J., 2003. Evaluation of the effect of contact between risers and guide frames on offshore spar platform. Ph.D. Dissertation, Civil Engineering Department, Texas A&M University, College Station, TX.

Korsmeyer, F. T., Lee, C. H., Newman, J. N., and Sclavounos, P. D., 1988. The analysis of wave effects on TLP. Proceedings of OMAE'88, Houston.

Lee, C. H., 1995. WAMIT Theory Manual. Department of Ocean Engineering, Massachusetts Institute of Technology, Cambridge, MA.

Lee, D. H., and Choi, H. S., 2000. A dynamic analysis of FPSO-shuttle tanker system. Proceedings of 10th International Offshore and Polar Engineering Conference, Seattle, USA.

Lee, C. H., and Korsmeyer, F. T., 1999. WAMIT User Manual. Department of Ocean Engineering, Massachusetts Institute of Technology, Cambridge, MA.

Lee, D. Y., Ha, M. K., and Kim, H. J., 1999. Development of dynamic positioning simulation program. Journal of Kansai Society of Naval Architects, Japan, No. 231, pp. 65-73.

Lee, D. H., Joo, S. M., and Choi, H. S., 1998. Control performance of a turret-moored vessel assisted by dynamic positioning system. Proceedings of International Federation of Automatic Control Conference on Control Applications in Marine Systems, Fukuoka, Japan, pp. 99-103.

Lee, C. H., Newman, J. N., Kim, M. H., and Yue, D.K.P, 1991. The computation of second-order wave loads. Proc. of OMAE'91, Stavanger, Norway.

Luo, Y., and Baudic, S., 2003. Predicting FPSO responses using model tests and numerical analysis. Proceedings of International Offshore and Polar Engineering Conference, Honolulu, Hawaii, USA, May 25-30, pp. 167-174.

Ma, W., Lee, M. Y., Zou, J., and Huang, E. W., 2000. Deepwater nonlinear coupled analysis tool, Proceeding of the 32nd Offshore Technology Conference, Houston, Texas, OTC 12085, pp. 655-665.

Meyer, E. A., and Huglen, Ø., 2003. What dynamic positioning means to floating storage and shuttle tankers in the Gulf of Mexico. Dynamic Positioning Conference, Houston, Texas, USA.

Nordgren, R. P., 1974. On computation of the motions of elastic rods. Journal of Applied Mechanics, vol. 41, pp. 777-780

Oil Companies International Marine Forum (OCIMF), 1994. Prediction of wind and current loads on VLCCs, 2nd ed., Witherby & Co. Ltd., London, England.

Ran, Z., 2000. Coupled dynamic analysis of floating structures in waves and currents. Ph.D. Dissertation, Civil Engineering Department, Texas A&M University, College Station, TX.

Ran, Z., and Kim, M. H., 1997. Nonlinear coupled responses of a tethered spar platform in waves. International Journal of Offshore and Polar Engineering, vol. 7, No. 2, pp. 111-118.

Ran, Z., Kim, M. H., and Zheng, W., 1999. Coupled dynamic analysis of a moored spar in random waves and current (Time-domain Vs. Frequency-domain Analysis). Journal of Offshore Mechanics and Arctic Engineering, vol. 121, pp.194-199.

Ran, Z., Kim, M. H., Niedzwecki, J. M., and Johnson, R. P., 1995. Response of s spar platform in random waves and currents (Experiment Vs. Theory). International Journal of Offshore and Polar Engineering, vol. 6, No. 1, p 27-34.

Sorensen, A. J., 2003. Marine cybernetics: Modeling and control. Lecture notes. Department of Marine Technology, Norwegian University of Science and Technology.

Sorenson, A. J., and Strand, J. P., 1998. Positioning of semi-submersibles with roll and pitch damping. Proceedings of International Federation of Automatic Control Conference on Control Applications in Marine Systems, Fukuoka, Japan, pp. 61-67.

Sorensen, A. J., Strand, J. P., and Fossen, T. I., 1999. Thruster assisted position mooring system for turret-anchored FPSOs. Proceedings of the IEEE International Conference on Control Applications, Hawaii, USA, pp. 1110-1117.

Strand, J. P., Sorensen, A. J., and Fossen, T. I., 1998. Design of automatic thruster assisted position mooring systems for ships. Modeling, Identification and Control, vol. 19, no. 2, pp. 61-75.

Wichers, J.E.W., and Devlin, P. V., 2001. Effect of coupling of mooring lines and risers on the design values for a turret moored FPSO in deep water of Gulf of Mexico. Proceedings of 11th International Offshore and Polar Engineering Conference, vol. 3, pp. 480-487.

Wichers, J.E.W., and Dijk, R., 1999. Benefits of using assisted DP for deepwater mooring systems. Offshore Technology Conference, OTC 10781, Houston, USA.

Wichers, J.E.W., and Ji, C., 2000. On the coupling term in the low-frequency viscous reation forces moored tankers in deep water. Proceedings of Offshore Technology Conference, OTC 12086 [CD-ROM], Houston, Texas.

VITA

Sangsoo Ryu

Nam-gu, Juan 1 Dong, 199-12, 7 Tong, 1 Bahn

Incheon, Korea, 402-201

E-mail address: sryu@aggienetwork.com

Sangsoo Ryu was born in Seoul, Korea on March 20, 1970. He graduated from Inha University with a bachelor of science in Naval Architecture and Ocean Engineering in August, 1992. He entered the graduate school of Inha University in March, 1993 and received a master of science in Naval Architecture in February, 1995. After graduation, he joined the Republic of Korea Navy and taught at the Korean Naval Academy until June 1998. He also taught at Kyung-nam University before he entered the graduate program at Texas A&M University in January, 1999. Sangsoo Ryu received a Ph.D. in Ocean Engineering in December, 2003. He is married to Jihyun and has two daughters Hannah and Grace.